

COPI

Project Report
SC-80

AD-A215 934

Laser Intersatellite Transmission Experiment Spatial Acquisition, Tracking, and Pointing System

J.E. Kaufmann
E.A. Swanson

12 September 1989

Lincoln Laboratory
MASSACHUSETTS INSTITUTE OF TECHNOLOGY
LEXINGTON, MASSACHUSETTS



Prepared for the Department of the Air Force
under Contract F19628-85-C-0002.

Approved for public release; distribution is unlimited.

DTIC
ELECTE
DEC 18 1989
S B D

89 12 18 047

This report is based on studies performed at Lincoln Laboratory, a center for research operated by Massachusetts Institute of Technology, with the support of the Department of the Air Force under Contract F19628-85-C-0002.

This report may be reproduced to satisfy needs of U.S. Government agencies.

The ESD Public Affairs Office has reviewed this report, and it is releasable to the National Technical Information Service, where it will be available to the general public, including foreign nationals.

This technical report has been reviewed and is approved for publication.

FOR THE COMMANDER

Hugh L. Southall

Hugh L. Southall, Lt. Col., USAF
Chief, ESD Lincoln Laboratory Project Office

2

MASSACHUSETTS INSTITUTE OF TECHNOLOGY
LINCOLN LABORATORY

**LASER INTERSATELLITE TRANSMISSION EXPERIMENT
SPATIAL ACQUISITION, TRACKING, AND POINTING SYSTEM**

*J.E. KAUFMANN
E.A. SWANSON
Group 67*

PROJECT REPORT SC-80

12 SEPTEMBER 1989

Approved for public release: distribution is unlimited.

DTIC
ELECTE
DEC 18 1989
S B D

LEXINGTON

MASSACHUSETTS

ABSTRACT

This report describes the spatial acquisition, tracking, and pointing system of the MIT Lincoln Laboratory Laser Intersatellite Transmission Experiment (LITE) flight package which was to be integrated on the NASA Advanced Communications Technology Satellite (ACTS). The overall design approach and underlying rationale are also discussed. Considerable attention is given to the characterization of the spacecraft's dynamic environment and its impact on acquisition and tracking subsystem design and performance.

Accession For	
NTIS GRA&I	<input checked="" type="checkbox"/>
DTIC TAB	<input type="checkbox"/>
Unannounced	<input type="checkbox"/>
Justification	
By	
Distribution/	
Availability Codes	
Dist	Avail and/or Special
A-1	

TABLE OF CONTENTS

Abstract	iii
List of Illustrations	vii
List of Tables	ix
List of Acronyms	xi
1. INTRODUCTION	1
1.1 Background	1
1.2 Experiment and System Overview	2
1.3 Organization of Report	6
2. SYSTEM REQUIREMENTS	9
2.1 Pointing Requirements	9
2.2 Tracking Requirements	11
2.3 Acquisition Requirements	11
3. FLIGHT PACKAGE DESIGN CONSIDERATIONS	13
3.1 Mechanical Design	13
3.2 Thermal Design	15
3.3 Spacecraft Attitude Control and Disturbance Environment	16
3.4 Point-Ahead Requirement	23
3.5 Atmospheric Effects	24
4. SYSTEM DESCRIPTION	27
4.1 Optical System Overview	27
4.2 System Initialization	31
4.3 Alignment	32
4.4 Spatial Acquisition	39
4.4.1 Overview	39
4.4.2 Angular Uncertainty Budget	41
4.4.3 Acquisition Strategy	42
4.4.4 Implementation	50
4.4.5 Performance	52
4.5 Hand-Off from Acquisition to Tracking	62
4.6 Tracking and Pointing	64
4.6.1 Overview	64
4.6.2 Servo Description	65
4.6.3 Tracking Error Sensor	71
4.6.4 Pointing Budget	77

5. CONCLUSION AND DISCUSSION	79
ACKNOWLEDGMENTS	83
REFERENCES	85
APPENDIX	89

LIST OF ILLUSTRATIONS

Figure No		Page
1	LITE Operational Overview	3
2	Spatial Acquisition Sequence	4
3	Impact of Tracking and Pointing Errors on BER Performance	10
4	Spacecraft-to-OMS Interface	13
5	<i>Finite Element Models of Optomechanical Subsystem</i>	14
6	Spacecraft-to-OMS Acceleration Transfer Functions	15
7	Simulated Spacecraft Pitch Disturbance Due to ESA	18
8	Simulated Spacecraft Pitch Disturbance Due to SAD	19
9	Simulated Spacecraft Pitch Disturbance in Transition between ESA and Gyro Attitude Control	20
10	Simulated Spacecraft Pitch Disturbance Due to Gyro	20
11	Measured MWA Acceleration Spectrum	21
12	Calculated Spacecraft-to-OMS LOS Transfer Function	22
13	<i>Simplified OMS Schematic</i>	27
14	OMS Optical Prescription	28
15	Top and Bottom Views of OMS	29
16	Source Stabilization Loop Block Diagram	32
17	Source Stabilization Loop Optical Diagram	33
18	Boresight System Block Diagram	35
19	Boresight Optical Diagram	36
20	Telescope LOS-to-Spacecraft System Alignment Block Diagram	37
21	Telescope LOS-to-Spacecraft Optical Diagram	38
22	Acquisition LOS-to-Spacecraft System Alignment Block Diagram	39
23	Acquisition LOS-to-Spacecraft System Optical Diagram	40
24	Acquisition System Block Diagram	43
25	Acquisition System Optical Diagram	44

26	CPM Azimuth Jitter Performance	45
27	Acquisition Signal and Matched Filter Response	46
28	Acquisition Signal Spectrum	47
29	Main and Dither Scans for Acquisition Threshold Detection	48
30	Multiple Region Acquisition Scan	49
31	Acquisition System Signal Processing	50
32	Acquisition Time/Jitter Trade-Off	60
33	Acquisition Margin/Jitter Trade-Off	60
34	Tracking Disturbance Spectrum	62
35	Tracking System Normalizing Angle Error Detector	63
36	Simplified Tracking and Pointing System	65
37	Tracking System Block Diagram	66
38	HBO Loop Block Diagram	67
39	CPM Azimuth Loop Block Diagram	68
40	Tracking System Closed-Loop Rejection Performance	71
41	Tracking System NEA Performance	73
42	Tracking System Operating Ranges	74
43	Pointing and Tracking System Block Diagram	76
44	Pointing and Tracking Optical Diagram	77
A-1	Pick Maximum Dither Scan Performance (Nighttime Earth Background)	91
A-2	Pick Maximum Dither Scan Performance (Daytime Earth Background)	92

LIST OF TABLES

Table No		Page
1	Key ACTS/LITE System Characteristics	2
2	Spatial Acquisition System Options	5
3	LITE Spatial Acquisition/Tracking System	5
4	Highlights of ACTS/LITE Acquisition System Specifications	6
5	Highlights of ACTS/LITE Tracking System Specifications	7
6	Acquisition Angular Uncertainty Budget	16
7	Spacecraft Disturbances	17
8	LOS Disturbances Due to MWA	23
9	Periscope-to-Spacecraft Alignment Accuracy	34
10	Telescope-to-Spacecraft Alignment Accuracy	37
11	Line-of-Sight Jitter During Acquisition	44
12	Matched Filter Characteristics	51
13	LEO-ACTS Acquisition Link Budget	53
14	Acquisition and Tracking System Noise Parameters	55
15	Acquisition System Performance Summary	61
16	HBO Loop Parameters	69
17	Azimuth CPM Loop Parameters	69
18	Tracking System Uncompensated Closed-Loop Jitter	70
19	Tracking System Link Budget	75
20	Pointing System Budget	78

LIST OF ACRONYMS

ACTS	Advanced Communications Technology Satellite
AGC	Automatic Gain Control
ANT	Antenna Assembly
APD	Avalanche Photo Detector
ATD	Acquisition and Tracking Detector
BER	Bit Error Rate
BW	Beamwidth
CCD	Charge Coupled Device
CG	Center of Gravity
CID	Charge Injection Device
CPM	Coarse Pointing Mirror
DAC, D/A	Digital to Analog Converter
DDLTT	Direct Detection Laser Transceiver
DM	Diagnostics Module
ESA	Earth Sensor Assembly
FOV	Field of View
FSK	Frequency Shift Keying
FWHM	Full-Width-Half-Maximum
GEO	Geostationary Earth Orbit
HBO	High-Bandwidth Optic
ICD	Interface Control Document
I/F	Interface
LEO	Low Earth Orbit
LITE	Laser Intersatellite Transmission Experiment
LCS	Line of Sight
MWA	Momentum Wheel Assembly
NAED	Normalizing Angle Error Detector
NASTRAN	NASA Structural Analysis Program
NEA	Noise Equivalent Angle
NEB	Noise Equivalent Bandwidth
OMS	Optomechanical Subsystem
PAM	Point Ahead Mechanism
PIN	P-Type Intrinsic N-Type
PDR	Preliminary Design Review
PM	Primary Mirror

RDC	Resolver to Digital Converter
rss	Root-Sum Square
SAD	Solar Array Drive
SADA	Source Alignment Detector Assembly
SAP	Spatial Acquisition Processor
S/C	Spacecraft
SM	Secondary Mirror
SSM	Source Select Mirror
TIA	Transimpedance Amplifier
WFE	Wavefront Error

LASER INTERSATELLITE TRANSMISSION EXPERIMENT SPATIAL ACQUISITION, TRACKING, AND POINTING SYSTEM

1. INTRODUCTION

1.1 BACKGROUND

The potential advantages of laser communications over RF systems in intersatellite links, particularly for higher data rates, have become widely recognized [1-2]. These include smaller apertures which are more easily integrated with the spacecraft, relative freedom from interference (intentional or otherwise), and the availability of extremely large bandwidths. Recent advances in optical device technology, particularly in semiconductor lasers, have spurred considerable research and development efforts in laser transmitter and receiver subsystems. However, for intersatellite links, accurate pointing of an optical communications beam as narrow as a few microradians to a distant terminal also presents a significant challenge to the system designer. The problem is complicated by issues such as uncertain platform attitude and on-board angular disturbances which can be many beamwidths in magnitude. This report discusses the spatial acquisition and tracking problem in the context of an optical communications demonstration to have been conducted by MIT Lincoln Laboratory on the *NASA Advanced Communications Technology Satellite (ACTS)*. As such it represents the detailed description of a point design. Although the flight portion of this demonstration was cancelled due to lack of sufficient funding, an engineering model of the opto-mechanical module is being built to validate the design techniques and thus reduce risk for future lasercom flight programs.

Since 1985, Lincoln Laboratory has been involved in the design and development of an experimental optical communications subsystem on ACTS, which was to be launched into a geostationary orbit sometime around 1990. RCA is the ACTS spacecraft contractor. The ACTS program was to demonstrate a variety of both microwave and optical space communications technologies. At RF it provides a number of high data rate channels via a 30-GHz uplink and 20-GHz downlink, using two multibeam antennas. The optical communications experiment was to test both heterodyne and direct-detection systems as candidates for future intersatellite links. NASA's Goddard Space Flight Center was to provide the direct-detection hardware while the heterodyne system was the responsibility of Lincoln Laboratory. The Lincoln portion of the experiment has been designated as the *Laser Intersatellite Transmission Experiment (LITE)*. The direct-detection system, called the direct-detection laser transceiver (DDLTL), was to be implemented as an add-on subsystem to be delivered to Lincoln Laboratory for integration in the total optical communications package and with ACTS. The LITE design includes acquisition, tracking, and pointing subsystems which are the subject of this report. The design of a major part of this opto-mechanical subsystem (OMS), has been performed jointly by Lincoln Laboratory and by Perkin-Elmer Corporation under contract to Lincoln.¹

¹ In January 1988, after successful OMS preliminary and critical design reviews and a successful LITE preliminary design review, the LITE program was rescoped from a flight program to an engineering model due to funding cutbacks.

Because laser satellite communications technology is still in an emerging state, there is limited information in the literature about the acquisition and tracking problem based on experience with an actual satellite platform [3-14]. The intent of this report is to identify the problem areas requiring attention and careful design by the acquisition/tracking subsystem designer and to present a design solution in the context of ACTS/LITE. Models for the attitude accuracy and disturbances environment of a candidate satellite platform and applications of key component technologies are highlighted. Although the discussion is specific to LITE, the basic approaches should be applicable to other future laser communications satellite systems.

1.2 EXPERIMENT AND SYSTEM OVERVIEW

The LITE portion of the experiment was to demonstrate a one-way transmission of data at rates up to 220 Mbps from ACTS to a receiving terminal. Data was to be sent from the ground over the 30-GHz uplink to ACTS where it was to be demodulated and then retransmitted optically to the receiver. An on-board pseudorandom sequence generator was provided for bit-error rate (BER) testing. Initial experiments were to be conducted using a special purpose ground station as a substitute for another satellite. This station was to be located at an astronomically favorable high-altitude site in the southwestern United States, such as Mt. Wilson in southern California, to mitigate the effects of atmospheric turbulence on optical beam propagation through the atmosphere. This arrangement would have provided a relatively simple and inexpensive way to verify performance in advance of the launch of another satellite terminal in the future. Follow-up demonstrations of a complete satellite-to-satellite link could have involved a second LITE-compatible package on board a low-earth orbit (LEO) satellite. This report will focus on the later scenario. Although we will briefly comment on atmospheric effects, they are not included in the various system budgets.

The key system characteristics of LITE are listed in Table 1, while Figure 1 provides a simplified experiment overview. Spatial acquisition and tracking between the two ends of the link are performed cooperatively. The receiving terminal will find and track a beam from ACTS and in turn will point a return beacon to ACTS (Figure 2). This beacon will not carry data modulation and is provided solely for acquisition and tracking.

Link	GEO to Ground, GEO, or LEO
Aperture Size	20-cm diam.
Transmit Beamwidth	4.3 μ rad FWHM, Diffraction-Limited
Transmit Laser Power	30 mW, Beacon and Data Transmitters
Wavelength Plan	LITE Transmitter: 8634 - 8656 Å Acq/Track Beacon: 8591 Å
Polarization	Opposite Circular for Transmit/Receive
Data Rates	27.5, 55, 110, 220 Mbps
Modulation	2-ary or 4-ary FSK

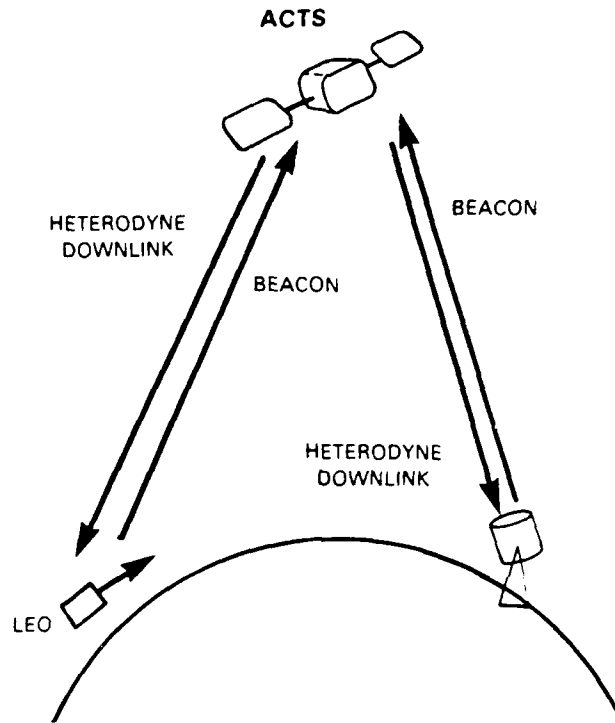
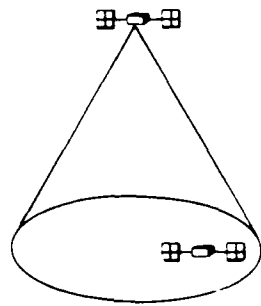


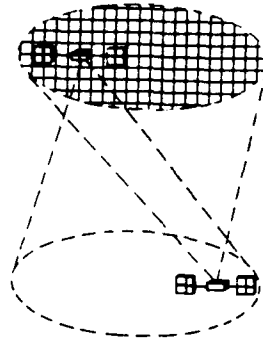
Figure 1 LITE operational overview

The design of the acquisition system involves a choice of illumination and reception strategies. Generally speaking, these can be categorized as either serial or parallel [15]. (A third possibility, namely zooming, can be considered as a serial/parallel hybrid.) Table 2 summarizes the characteristics of serial and parallel acquisition schemes. The ACTS flight package design evolved into one which employs a wide-beam parallel illumination strategy for the transmit beam and a serial-scan receiver using an APD front end. The other terminal employs a charge coupled device (CCD) parallel-search acquisition receiver and uses a moderately widened (several times diffraction limit) transmit beam.

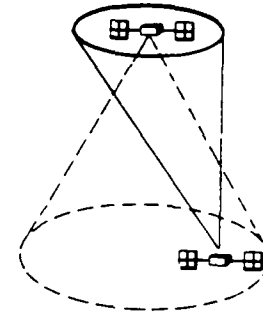
The spatial tracking system can adapt conventional RF angle-tracking techniques — monopulse or beam-dithering (conical scan or sequential lobing) — to the optical domain. The principles of these techniques are well documented in the radar literature. Tracking system design also involves selection of a sensor technology (heterodyne versus direct detection) and associated hardware (photodetectors, front-end design). The flight package uses a monopulse direct-detection tracker which shares the APD front-end with the acquisition system. The other receiving terminal, which carries a heterodyne data receiver, will perform tracking in the heterodyne mode [4].



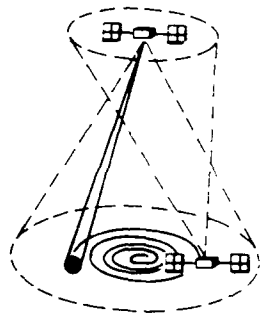
1) TRANSMITTER ILLUMINATES RECEIVER WITH BROADENED BEAM (~ 1 mrad)



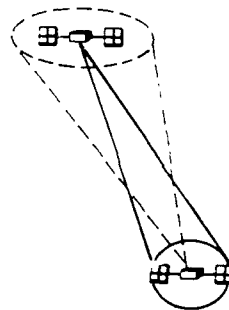
2) RECEIVER ACQUIRES TRANSMITTER WITH CCD



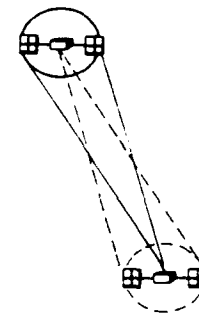
3) RECEIVER ILLUMINATES TRANSMITTER WITH BROADENED BEAM ($\sim 18 \mu\text{rad}$) WHILE COARSE TRACKING



4) TRANSMITTER SCANS FOR TARGET USING TRACKING DETECTOR FOV ($\sim 20 \mu\text{rad}$)



5) TRANSMITTER ACQUIRES, INITIATES TRACKING AND COLLAPSES DOWNLINK ($\sim 4.3 \mu\text{rad}$)



6) RECEIVER BEGINS TRACKING AND COLLAPSES UPLINK ($\sim 4.3 \mu\text{rad}$)

Figure 2. Spatial acquisition sequence.

106808.9

TABLE 2. Spatial Acquisition System Options		
	Transmit	Receive
Serial	Scan Narrow Beam via Steering Mirror	Scan Detector (e.g., APD) FOV via Steering Mirror, Serial Processing
Parallel	Broadened Beam	Wide FOV Detector Array (e.g., CCD), Parallel Processing

A summary of the key characteristics of the spatial acquisition/tracking systems is given in Table 3. Highlights of the specifications for the ACTS/LITE acquisition and tracking systems are given in Tables 4 and 5, with a discussion on most of these later in this report. Only the flight package system on board ACTS is considered, with the intention of focusing on the issues of performing acquisition and tracking in space on an actual satellite platform. Closely related issues, such as the thermal and mechanical designs, are also discussed briefly.

TABLE 3. LITE Spatial Acquisition/Tracking Systems				
	Detector	Heterodyne / Direct Detection	Acq/Track Receiver	Transmit Beamwidth (FWHM)
		Acquisition		
Flight Package	Quad APD	Direct Detection	Serial Scan	1 mrad
Receiving Terminal	CCD	Direct Detection	Parallel Search	18 μ rad
		Tracking		
Flight Package	Quad APD	Direct Detection	Monopulse	4.3 μ rad
Receiving Terminal	Quad P-I-N	Heterodyne Detection	Monopulse	4.3 μ rad

TABLE 4.
Highlights of ACTS/LITE Acquisition System Specifications

Specification		Comment
Detector	Quadrant APD	Quadrants Summed, 20 μ rad FOV
Received Beacon	8591 Å, 54 kHz Square-Wave Intensity Modulation	Avoids DC offsets and Low Frequency Interference at Receiver
Optical Filter	< 30 Å	Background Rejection
Scan Parameters	Spiral Pattern Diameter 1.25 μ rad Velocity 160, 40, 10, 2.5 mrad/s Overlap 5, 10, 15 μ rad	
CPM Tracking Slew Rate	0 - 300 μ rad/s	LEO
Search Time	Variable 0.5 - 26 s	Per 1.25 mrad diameter Region
Detection	Threshold or Pick Maximum	Detection Filter Matched to Scan Rate
Open-Loop LOS Jitter (OMS and S C)	< 6 μ rad rms	Spacecraft SAD and ESA off. Gyro on
Signal Margin	9.7 - 18.5 dB	Varies with Scan Rate, Detection Mode, and Background (> 0.98 Prob. Acq.)

1.3 ORGANIZATION OF REPORT

Section 2 defines the top-level requirements imposed on the acquisition and tracking subsystems. Constraints on system design, including package size, weight, and power, satellite launch and orbital environments, and the special case of atmospheric effects on the ACTS-to-ground link are discussed in Section 3. The details of system design and operation are given in Section 4 in the form of a walk-through of the key system functions, beginning with system initialization and culminating in cooperative pointing and tracking. A conclusion is found in Section 5.

TABLE 5.
Highlights of ACTS/LITE Tracking System Specifications

Specification		Comment
Detector	Quadrant APD	Monopulse Detection. 20 μ rad FOV
Received Beacon	8591 Å. 54 kHz Square-Wave Intensity Modulation	Avoids DC offsets and Low Frequency Interference at Receiver
Optical Filter	< 30 Å	Background Rejection
Loop-Crossover Frequency	500 or 1000 Hz, Selectable	Disturbance Rejection vs NEA
CPM Slew Rate	0 - 300 μ rad/s	LEO
Tracking Error	< 0.215 μ rad rms Jitter < 0.086 μ rad Bias	< 1 dB Comm. Loss
Signal Margin	18.8 dB 18.5 dB 0.5 dB	Night Earth Background Day Earth Background Solar Background
Disturbance Amplitude Margin	17 dB 3.0 dB	Low Frequency Sources Momentum Wheel

2. SYSTEM REQUIREMENTS

2.1 POINTING REQUIREMENTS

The two types of pointing requirements can be separated as those during communication and during acquisition. This section deals with the requirements during communication, and Section 2.3 discusses requirements during acquisition.

The purpose of the pointing system is to deliver power to and receive power from a distant receiver. In the case of a communication system the quality of pointing can be quantified in terms of the effect on link BER. Several papers have been published on the effect of pointing errors on communication performance either in terms of average BER or probability of burst errors [14,16-20]. A major topic of these publications is optimizing antenna gain for a given pointing error. The optimized antenna diameter is obtained by a compromise between the increase in power that results from increased antenna gain and the eventual decrease in power that results from increasing pointing errors due to decreasing antenna beamwidth. Many of the assumptions used in their analyses are invalid for our system. For instance, it is typically assumed that the tracking errors are Gaussian and independent of signal power. Our pointing budget reveals that the dominant source of jitter is composed of approximately equal parts of Gaussian and non-Gaussian jitter, that the Gaussian component is a function of signal power, and that a large component of the pointing error is due to bias.

Our philosophy has been to avoid regions in which pointing errors are a significant limitation on the BER. Once the antenna aperture is big enough to close the link for the margin, data rate, and modulation format desired, and assuming the spatial pointing system can support that link, increasing the antenna aperture would only be detrimental to overall system performance. This approach will minimize susceptibility to modeling errors, ensure that the pointing systems at the transmitter and receiver are uncoupled and remain in their linear range, and minimize the need for reacquisition due to loss-of-lock. Minimizing loss-of-lock is important not only because spatial, frequency, and timing systems must reacquire, but re-acquisition can require a time-consuming interface with the spacecraft control system.²

The effect of pointing (and tracking) errors on communication performance will be characterized in terms of the increase in transmitter power required to maintain a constant average BER [20]. It is assumed that both the transmitter and receiver aperture diameter are fixed, and that the modulation format is noncoherent 4-ary FSK modulation with rate 1/2 convolutional coding. However, the results are representative of other systems, too. The dependence of the BER conditioned on received signal power has been presented [21]. It is a complicated function that depends on many parameters, one of which is received signal power. For a heterodyne communication system the received IF signal power is a function of the pointing

² Acquisition on board ACTS requires a command to stop the spacecraft solar array drive in order to reduce line-of-sight motion.

error from the transmitter and the tracking error at the receiver. The power loss, $L(\epsilon)$, due to radial pointing or tracking error, ϵ , is easy to derive and is well approximated by

$$L(\epsilon) = \left[\frac{2 J_1(\pi\epsilon)}{\pi\epsilon} \right]^2 \quad (1)$$

where ϵ has been normalized by the transmitter or receiver FWHM beamwidth (λ/d). The increase in transmitter signal power required to maintain a specified average BER can be found by averaging the conditional BER over the respective pointing and tracking error probability densities.

Figure 3 shows a special case of our analysis. Here we have assumed an average BER of 10^{-6} and that each of the four integration axes (azimuth and elevation at the transmitter and receiver) have probability densities that are independent identically distributed Gaussian random variables. On the ordinate is the rms single-axis error and the plots are parameterized by radial bias (i.e., total transmitter bias = total receiver bias = 0.2 BW).

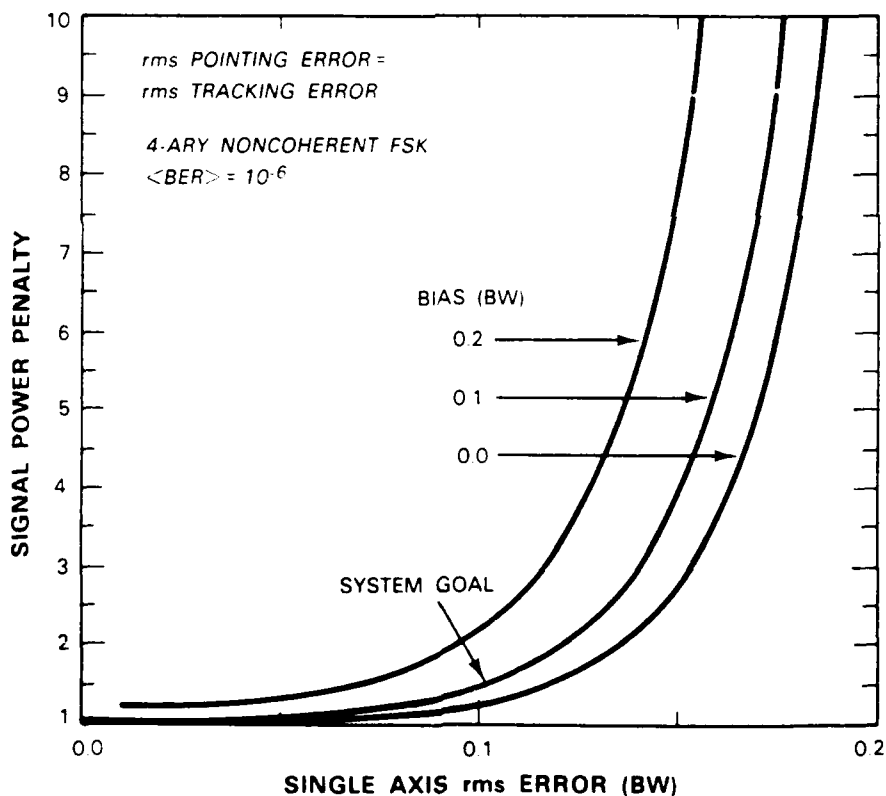


Figure 3. Impact of tracking and pointing errors on BER performance.

For each curve in Figure 3 there is a value of rms error beyond which the power penalty quickly becomes prohibitive and that value decreases with increasing bias. Our goal for the transmitter pointing system is to keep both the bias and jitter to less than 0.1 beamwidths (BW). Under the assumptions, this would allow a power penalty of less than 1 dB. Note that a more elaborate analysis has been performed using the actual models for pointing errors (Section 4) and yields a similar result for the power penalty.

2.2 TRACKING REQUIREMENTS

As indicated earlier, it is desirable to keep the pointing errors less than 0.1 BW. For our 20-cm aperture and wavelength of 0.86 μm , this corresponds to 0.43 μrad . Since the spacecraft has disturbances many orders of magnitude larger than this value (see Section 4.6.1), a beacon must be sent from the receiving terminal to the transmitter to be used as a reference for the ACTS pointing system. Although inertial reference units and star trackers can be used to correct for some of the spacecraft disturbances (principally at low frequencies), dynamic thermal and vibrational environments still dictate the need for an optical beacon reference.

The accuracy with which the spatial tracking system can track the beacon is a lower bound for pointing system accuracy. In addition to tracking errors, there are many other contributors to pointing error (see Section 4.6.4). Each item must be allocated a fraction of the overall pointing budget. For instance, to the tracking system we allot to each axis a budget of 0.05 BW to rms tracking error and 0.02 BW to tracking bias.

2.3 ACQUISITION REQUIREMENTS

In order to reduce the large spatial uncertainties at the transmitter and receiver to the point where cooperative pointing and tracking of diffraction-limited beams can begin, a spatial acquisition system is needed. There are a number of obvious goals for this system: (1) that after transferring various ephemeris data and acquisition parameters, the acquisition sequence be autonomous; (2) that after moving the coarse pointing optics to the region of interest, the time required for acquisition be less than ~ 1 min; (3) that the probability of a failed acquisition be small ($\sim 10^{-2}$); and (4) that the acquisition system be simple so as not to dominate overall system risk, complexity, weight, and power. A few papers have dealt with optical spatial acquisition [15,22,23]. Although a cooperative serial illumination/parallel search best satisfies the first three requirements, it was decided a parallel illumination/serial search at the transmitter and parallel illumination/parallel search at the receiver would best satisfy all four requirements. Parallel illumination helps minimize the coordination needed between transmitter and receiver, and although a parallel search requires less signal power and search time, a serial search at the transmitter allows the acquisition system to share much of the hardware that is required for the tracking system.

The acquisition algorithm is depicted in Figure 2. First, the transmitter (on ACTS) illuminates the receiver with a spoiled beam. Next, the receiver performs a parallel search with a CCD and acquires the spoiled beam. Since there is not enough power to accurately track the beam, a broadened beam is pointed open-loop to illuminate the transmitter. The amount of broadening is chosen to be larger than the nominal pointing uncertainty. Next, the transmitter scans its uncertainty zone with the tracking detector array, acquires, and begins tracking the beacon. The transmitter then collapses its broadened beam down to a

diffraction-limited beam and adds the appropriate point-ahead angle. The increase in received power allows the receiver to begin tracking. Finally, the receiver can collapse its beam down to the diffraction limit and also adds the appropriate point-ahead angle.

This acquisition sequence dictates two pointing requirements. The first is that the errors introduced by the mechanical pointing devices themselves should not significantly add to the total receiver uncertainty. As will be seen in the Section 3, the attitude uncertainty of the ACTS platform is ~ 1 mrad. Therefore the open-loop pointing system accuracy requirement was chosen as $100 \mu\text{rad}$. Second, since a serial acquisition using the tracking detector FOV is used, the LOS jitter during the acquisition scan must be less than the FOV to ensure no gaps in coverage of the uncertainty zone. Section 4.4 shows the budgeted value of $6\text{-}\mu\text{rad}$ rms for LOS jitter is consistent with the tracking detector FOV of $20 \mu\text{rad}$.

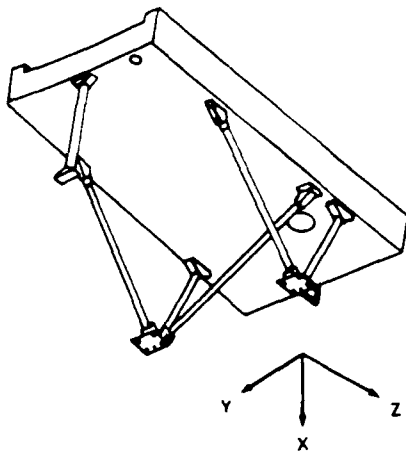
3. FLIGHT PACKAGE DESIGN CONSIDERATIONS

As is the case with any spaceflight package there are a number of constraints that can affect the system design and performance. These include the constraints associated with the launch and operational environments, which in turn, affect the mechanical and thermal design. Pointing and tracking performance are affected by the spacecraft attitude uncertainty and disturbance environment. In addition, the point-ahead requirement is significant for space-based platforms. Finally, the LITE experiment design was influenced by the requirement of establishing a link through the atmosphere. This section addresses these issues.

3.1 MECHANICAL DESIGN

The major mechanical design drivers are launch loads, a fundamental resonance mode requirement from the spacecraft contractor, and the on-orbit LOS jitter environment. The first obvious mechanical requirement is to ensure package survival through launch. The spacecraft contractor requires that the fundamental modes of the optical module be kept above 50 Hz to keep it from interacting with the low frequency rocket accelerations and to minimize coupling into the spacecraft attitude control system. In addition, while on-orbit the mechanical structure should either isolate, where possible, or minimize amplification of spacecraft mechanical disturbances (i.e., solar array drive, momentum wheels).

To meet the fundamental mode requirement and simultaneously satisfy the operational vibrational isolation requirements, a three-point kinematic mount is used in the spacecraft-to-optical module interface (Figure 4). The kinematic mounting helps minimize bench distortions due to thermal misalignments between the spacecraft and the OMS. The geometry and materials used in the mounting struts allows the interface to



PERCENTAGE OF TOTAL MASS PARTICIPATION
PER MODE IN THE SIX FUNDAMENTAL MODES

MODEL RESONANCE (Hz)	DIRECTION					
	X	Y	Z	θ_x	θ_y	θ_z
49.7		71.6		93.5		21.4
55.4			73.2		13.4	
62.1	1.7	18.9		2.3	1.9	9.4
136.9		6.3		3.0	2.4	56.0
144.9			23.3		16.7	8.0
151.5	92.9				60.7	2.6

Figure 4. Spacecraft-to-OMS interface.

106808-33

be tuned to optimize for vibration isolation and launch loads. Also contained in this figure is the total mass participation per mode in the six fundamental modes. Vertically, this table indicates extent of total mass contained in the first six modes. Horizontally, it indicates to what extent the modes are coupled. This data, as well as data on launch loading and vibrational isolation, were determined by a detailed NASTRAN model. The nodal representations of four of these finite element models are shown in Figure 5. These models were used extensively and often coupled with thermal, optical, and servo models to accurately determine system performance. As an example of the utility of this model, Figure 6 shows the acceleration transfer functions along the Z-axis to various points within the optical module. Note the fundamental resonance at 50 Hz. Below this resonance both launch and on-orbit disturbances are transmitted directly into the optical module; at this resonance they are amplified; above this resonance they are attenuated.

3.2 THERMAL DESIGN

Maintenance of wavefront quality and accurate pointing are tightly coupled to the thermal stability of the optical module. Temperature changes and variation in temperature gradients, if not controlled, can induce misalignments and mechanical deformation of key optical components (i.e., mirrors and lenses). The varying solar loading of both the electronics and the optical modules and the varying amount of electronic waste heat lead to a thermal environment with large dynamics and the need for precise thermal control. Operation over thermal extremes of full sun to no sun in the aperture and/or full sun to no sun on the radiators was required. To achieve these and other thermal goals, a thermal control system that utilizes both active and passive techniques is used. To maintain precise local control, the optical bench is divided into 24 active thermal control zones, each utilizing a hybrid temperature controller. The set points for the various control zones range from 15 to 27 C with a stability of approximately $\pm 1^\circ\text{C}$. The passive system utilizes a solar rejection window, thermal radiators, 22-layer kapton film-insulated blankets on exterior surfaces, and low conductivity tubular support trusses for the spacecraft-to-OMS interface. To minimize thermally induced drifts in the tracking system (mainly due to temperature sensitivity of the APD detectors), the temperature regulation within the detector housing is tighter, being $20 \pm 0.2^\circ\text{C}$. The pointing budget contained in Section 4.6.4 accounts for some of these effects. The electronics module, which requires less strict thermal control, is allowed to vary between -35 and $+60$ C.

3.3 SPACECRAFT ATTITUDE CONTROL AND DISTURBANCE ENVIRONMENT

One of the main drivers of the acquisition system design is the size of the angular uncertainty region. This uncertainty limits the accuracy with which initial acquisition of the received beam, as well as pointing of the transmit beam, can be performed. The three dominant components to angular uncertainty are (1) limitations within the spacecraft attitude control system and thermal warping of the spacecraft structure; (2) the open-loop pointing accuracy of the OMS relative to the spacecraft body; and (3) inaccuracies in orbital ephemeris data. The ACTS spacecraft body orientation determines the basic pointing accuracy of the LITE package. The platform pointing accuracy in pitch, roll, and yaw is shown in Table 6. This table includes worst-case values derived from the LITE/ACTS ICD [24], as well as best-case values derived from internal RCA design specifications (as of ACTS PDR) [25-28]. We expect the actual tolerance to be closer to the best-case values; however, the system is designed to accommodate both. Also included in this table are estimated values for uncertainty due to ephemeris and OMS open-loop pointing (Section 2.3). Section 4.4.2 discusses the angular uncertainty budget in more detail.

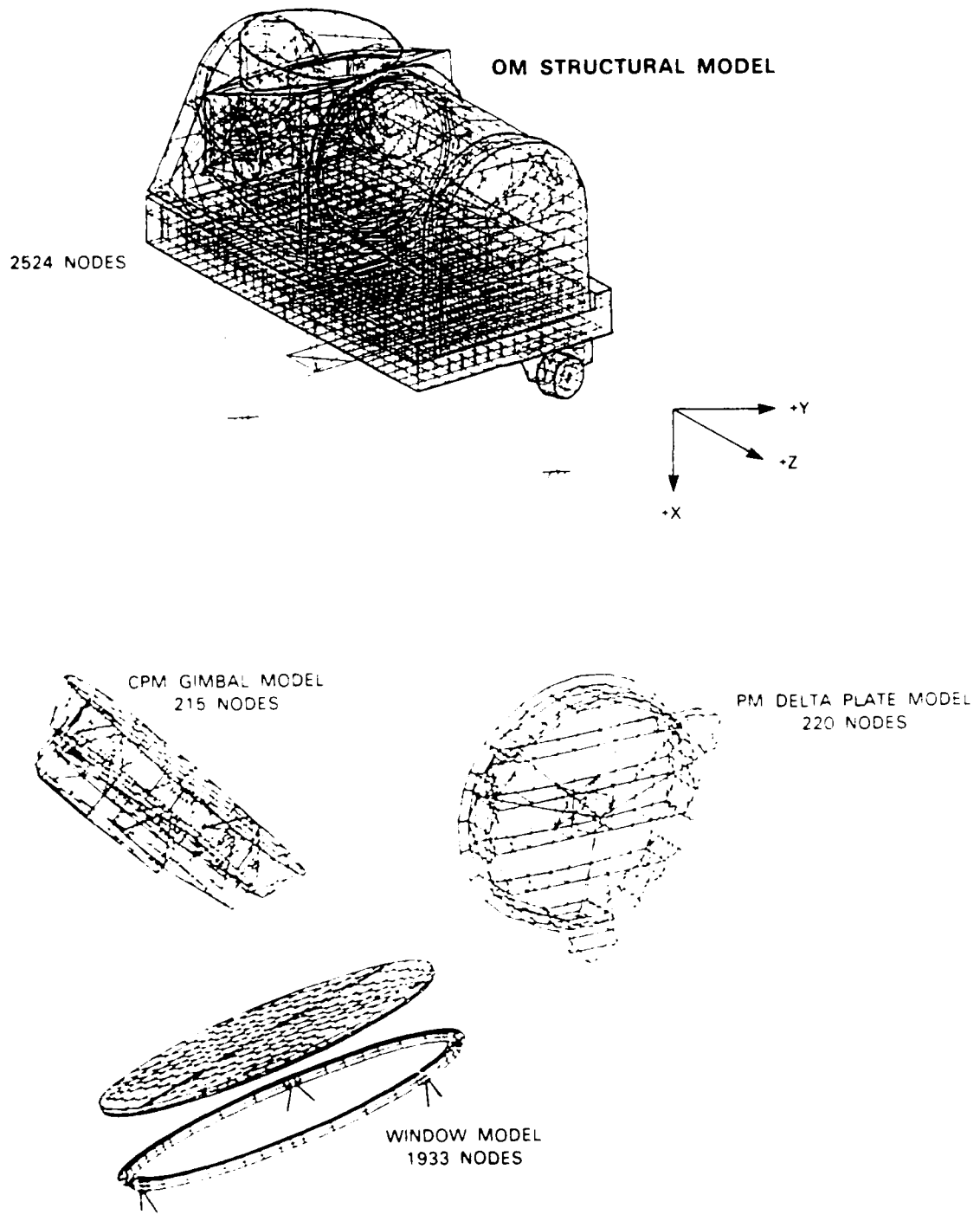
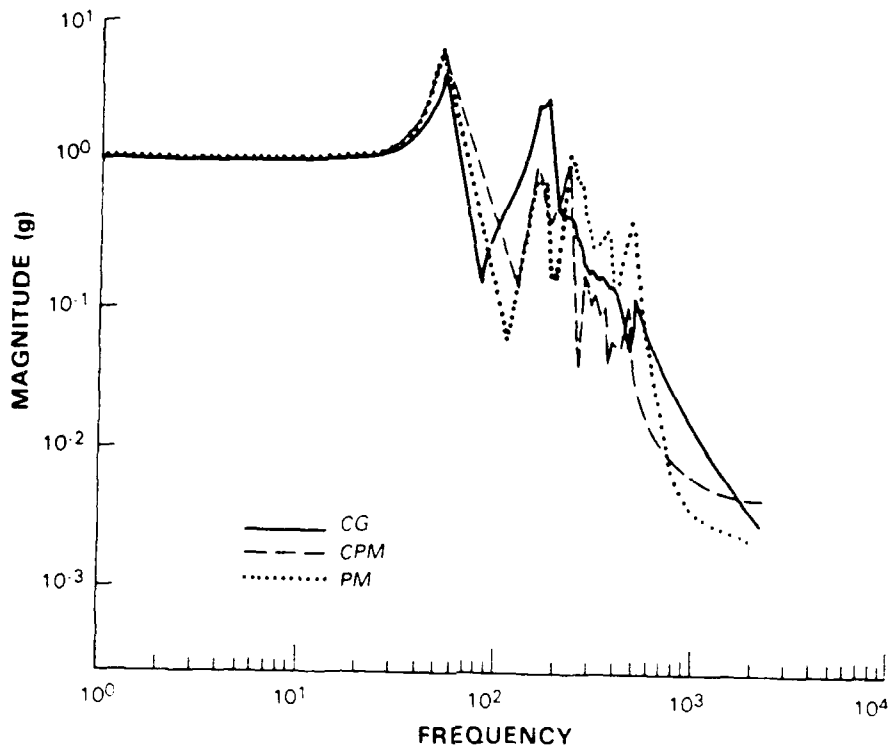


Figure 5 Finite element models of OMS

106608 32



121485 2

Figure 6. Spacecraft-to-OMS acceleration transfer functions

TABLE 6. Acquisition Angular Uncertainty Budget		
Ephemeris	0.1 mrad	
OMS Open-Loop Pointing	0.1 mrad	
ACTS Attitude Control	Best Case	Worst Case
Pitch	±0.5 mrad	±1.75 mrad
Roll	±0.3 mrad	±1.75 mrad
Yaw	±2.0 mrad	+4.4 mrad

Vibrational disturbances are another major design driver for the acquisition, tracking, and pointing system. The data available on the spacecraft disturbances was limited. In order to account for uncertainties in the models, an amplitude margin of 7 (17 dB) was assigned to all the disturbances except the momentum wheel assembly (MWA) and gyro (margins used in the MWA models are discussed later). In addition, all the disturbances are assumed to be present in each angular axis even though the models often predict the disturbance to be present mainly in one axis. Table 7 contains a list of the major platform disturbances. During spatial tracking, noise in the spacecraft earth sensor assembly (ESA) combined with quantization effects in the attitude control system and momentum wheel speed granularity give rise to a low frequency angular disturbance in pitch. Figure 7 is a simulated time history of the disturbance [25-28], the bandwidth of which is limited by the maximum update rate of the MWA of 1 Hz. This disturbance is modeled as a second order Butterworth spectrum with a bandwidth of 1 Hz and an rms amplitude of 100 μ rad (7X margin not included).

TABLE 7.
Spacecraft Disturbances

Earth Sensor Assembly (ESA)						
100 μ rad rms, 2nd-order Butterworth spectrum, 1 Hz -3dB frequency						
Solar Array Drive (SAD)						
70 μ rad peak, Triangle Wave, 0.75 Hz						
Antenna Assembly (ANT)						
30 μ rad peak, sine wave, 1 Hz						
10 μ rad peak, sine wave, 2 Hz						
Gyro						
Drift < 200 μ rad/h						
Noise < 2 μ rad rms						
Momentum Wheel Assembly (MWA)						
Harmonic Peak Harmonic Amplitudes (spacecraft coordinate system)						
Resonance (Hz)	Accelerations (g)			Rotational Displacements (μ rad)		
	x	y	z	θ_x	θ_y	θ_z
100	0.04	0.036	0.036	0.40	0.20	0.20
200	0.006	0.002	0.002	0.010	0.02	0.02
300	0.016	0.030	0.018	0.032	0.03	0.03
400	0.008	0.012	0.006	0.0028	0.001	0.001

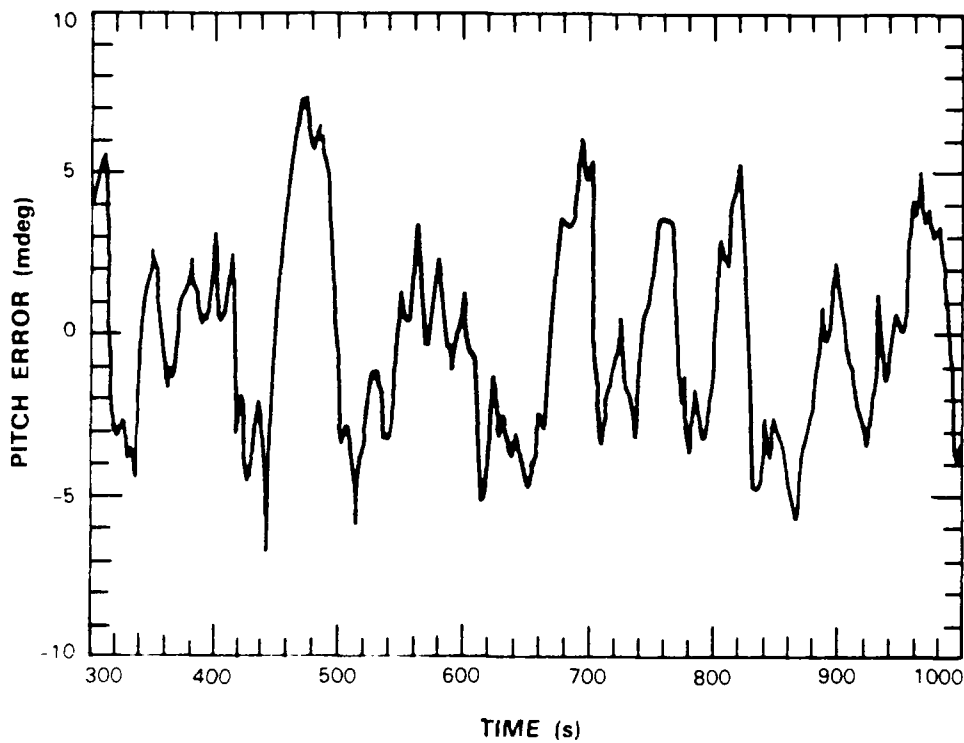


Figure 7. Simulated spacecraft pitch disturbance due to ESA.

The stepping of the solar array drive interacting with the low-frequency vibrational modes of the solar panels gives rise to a low-frequency angular disturbance in pitch. Figure 8 is a simulated time history of the disturbance [25-27] which is modeled as the first five harmonics of a triangle wave at a frequency of 0.75 Hz (this is the dominant mechanical mode that interacts with the stepping frequency of 0.25 Hz) and a peak amplitude of 70 μ rad.

To minimize LOS jitter, and thereby simplify the acquisition algorithm, during acquisition the solar array drive is turned off and the ESA is replaced with a gyro. The use of a gyro for attitude reference is a preexisting operational mode of the ACTS attitude control system of which the LITE package is able to take

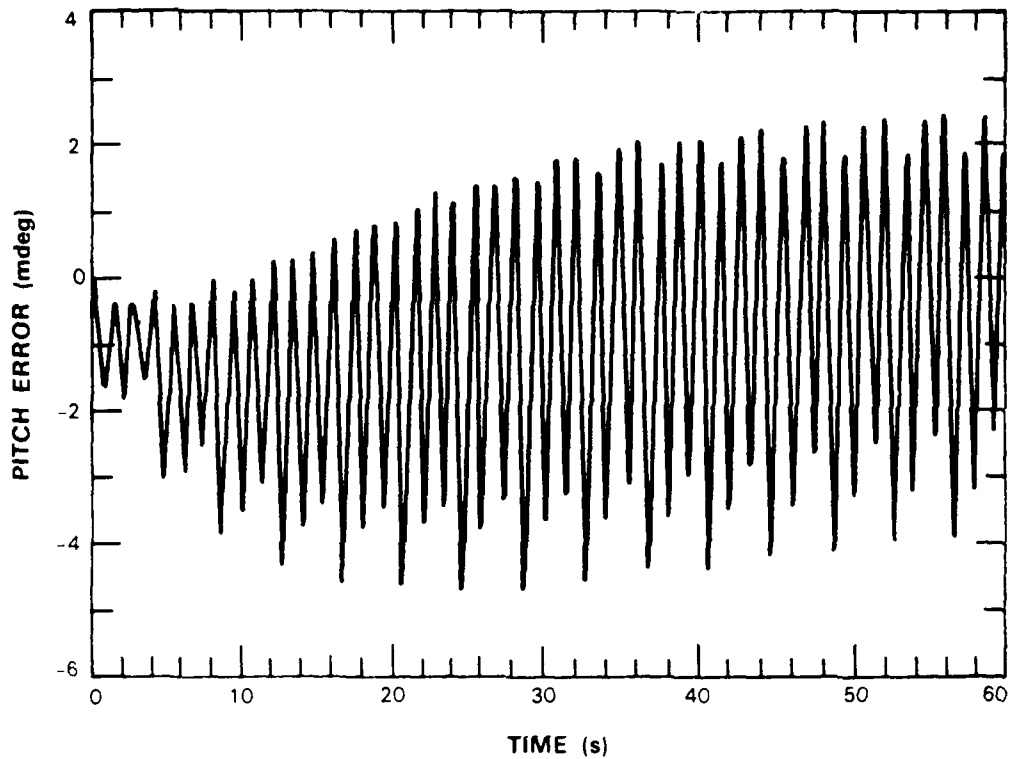


Figure 8. Simulated spacecraft pitch disturbance due to SAD.

advantage. Thus before acquisition begins, an interaction with the spacecraft is required to make the switch from ESA to gyro attitude control. Figure 9 is a simulated time history showing the transition from ESA to gyro control [27-29]. Figure 10 shows an expanded version of the gyro disturbance. There are two principal components to the gyro angular error: (1) a long-term linear drift, not expected to exceed $200 \mu\text{rad/h}$, and (2) a short-term jitter, not expected to exceed $2 \mu\text{rad rms}$. The short-term jitter model is a second-order Butterworth spectrum with a bandwidth of 1 Hz.

The stepping of the solar array drive also has the potential of interacting with the vibrational modes of the microwave antenna assemblies. This disturbance is modeled as two sine waves with amplitudes of 30 and $10 \mu\text{rad}$, at frequencies of 1 and 2 Hz, respectively.

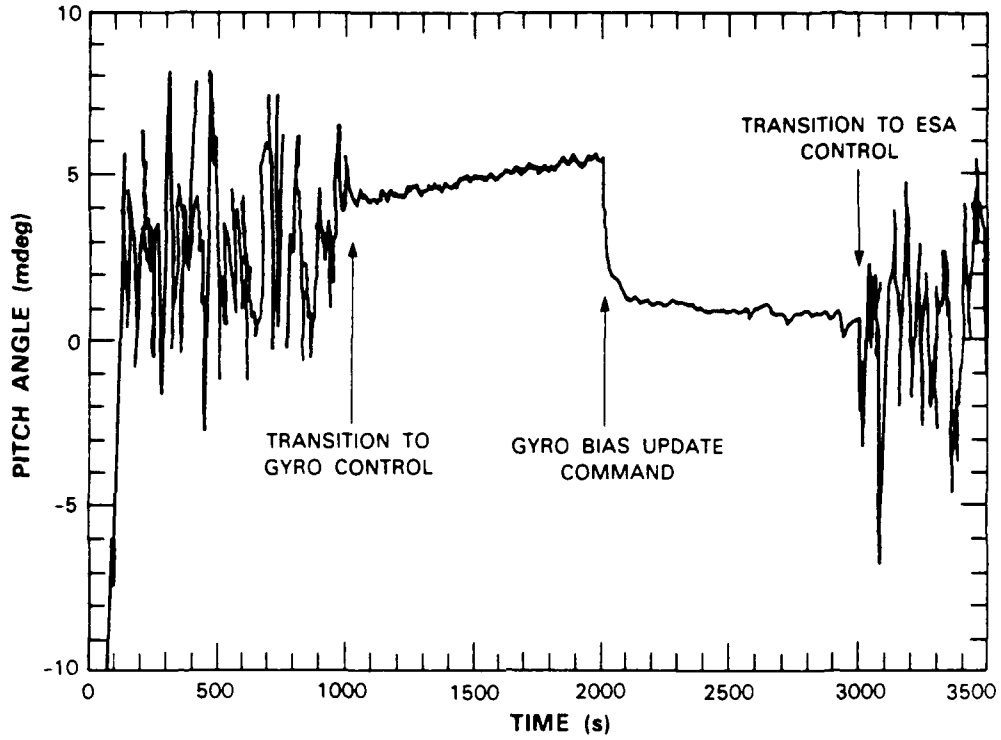


Figure 9 Simulated spacecraft pitch disturbance in transition between ESA and gyro attitude control

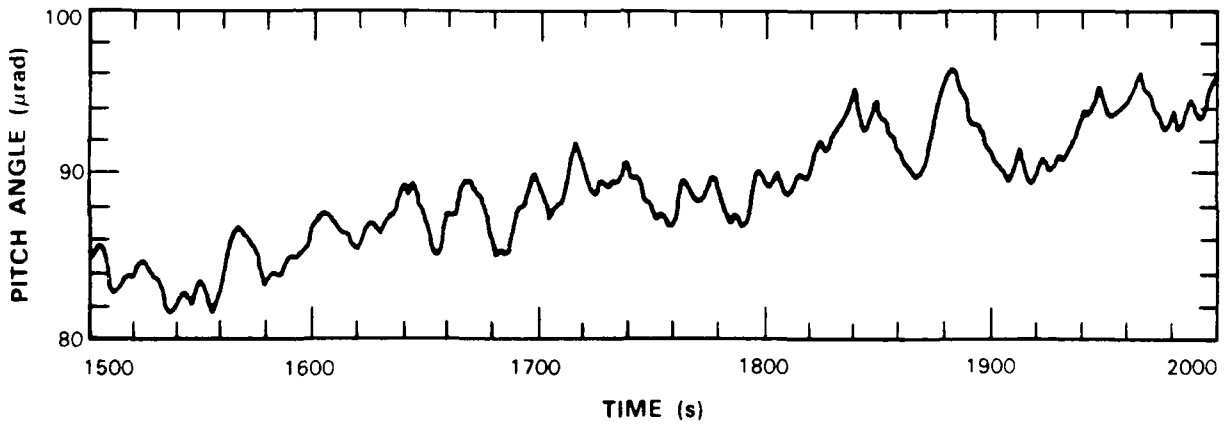


Figure 10. Simulated spacecraft pitch disturbance due to gyro.

Mass imbalances in the spacecraft momentum wheels, as well as imperfections in their bearings, can give rise to high-frequency jitter. This disturbance is later shown to be one of the dominant sources of tracking and pointing error as well as LOS jitter during acquisition (see Section 4.6). To model this disturbance, measurements of the acceleration jitter spectrum on an operational momentum wheel (over the operational spin frequency range $6000 \text{ rpm} \pm 8 \text{ percent}$) mounted on a similar (SPACENET) spacecraft were made [30-33]. Three-axis accelerometers were mounted on the MWA as well as at three mounting locations that were weighted to simulate an OMS. Figure 11 shows a typical acceleration jitter spectrum at the MWA [33,34]. Note that the imbalance of the MWA used was measured at $\sim 35 \text{ mg}$ whereas the specification allowed for 70. Therefore the measured responses were doubled when used in subsequent analysis (Table 7 includes this doubling). In addition, acceleration transfer functions (magnitude and phase) from the MWA to the mounting locations were determined using impact hammers and network analyzers [30,31]. At high frequencies the transfer functions were determined to be very dependent on the actual spacecraft bus design. Therefore a conservative approach was adopted, to assume that all the energy is transmitted from the MWA to the OMS mounting locations.

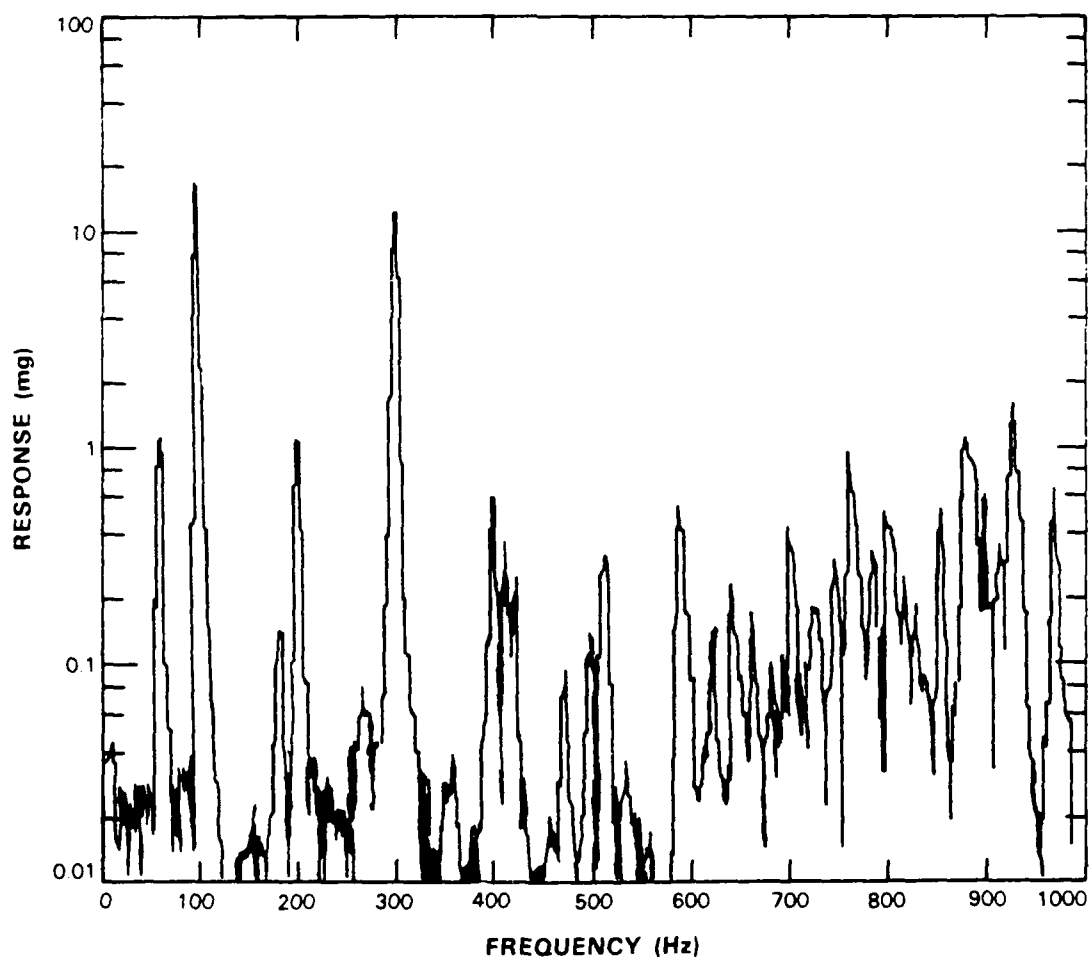


Figure 11. Measured MWA acceleration spectrum.

106808-16

The disturbances at the spacecraft mounting plane are modeled using six degrees of freedom at each MWA harmonic. The results for a wheel speed of 5000 rpm are given in Table 7. The operating range for the MWA is 5600 to 6400 rpm. Small but significant differences over this operating range are taken into account [35]. There are however, much larger differences in the response of the OMS as a function of frequency (see Figure 12). The rotational disturbance inputs are derived assuming the disturbances travel as a shear wave from the MWA to the OMS mounting locations [34,35]. At a given frequency, the LOS responses to the various inputs are absolute summed, while responses at different frequencies are root-summed-squared.

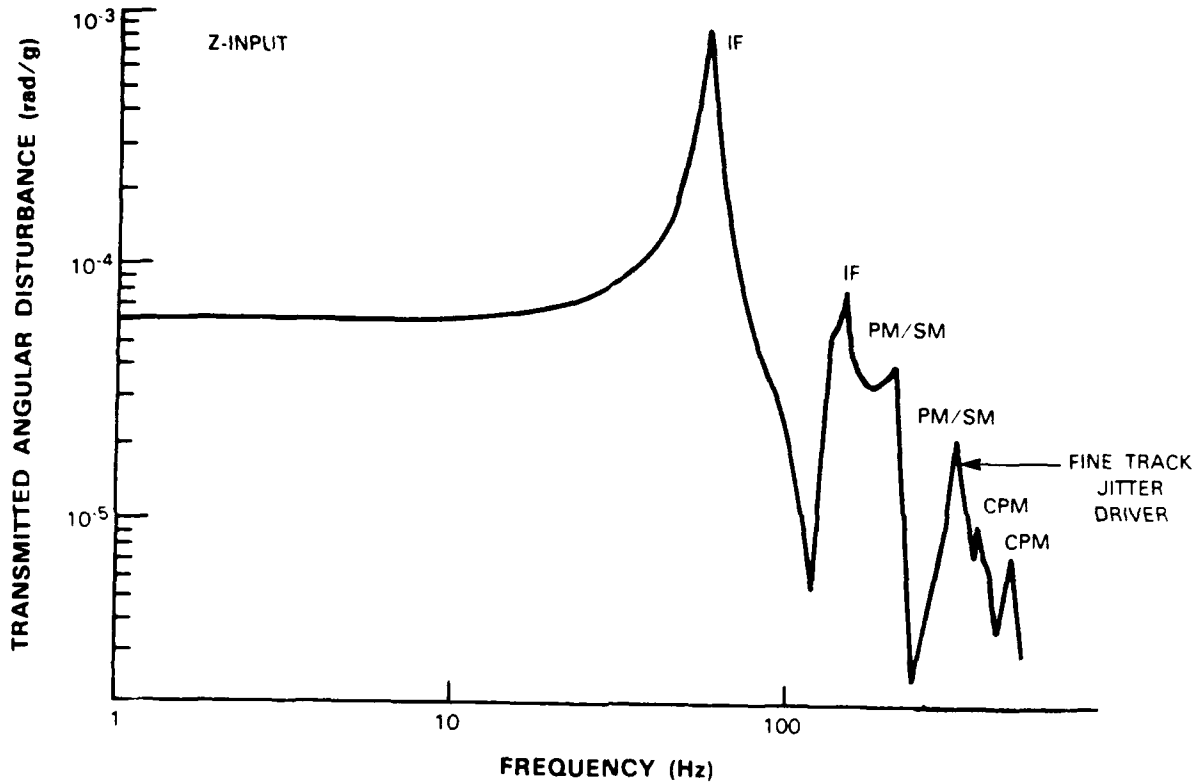


Figure 12. Calculated spacecraft-to-OMS LOS transfer function.

106808-31

To reiterate, four different levels of conservatism are built into the MWA model: (1) a worst-case MWA mass imbalance of 70 mg; (2) a transfer function of 1 from the MWA to the OMS mounting locations; (3) all disturbances at a given frequency add in phase; and (4) the worst-case operational MWA speed is assumed in the subsequent tracking analysis.

The disturbances discussed so far are the result of the host spacecraft to which the optical package is attached and represent the angular disturbances present in the OMS-to-spacecraft mounting plane. Extensive NASTRAN modeling of the optical components, mounts, and mechanical transfer functions was necessary to determine the actual LOS variations induced in the pointing system by these disturbances. By taking into account the relative motion of the various optical components, transfer functions of the form shown in Figure 12 are obtained. There are 12 different transfer functions to be considered (6 inputs, each with 2 outputs). Multiplying the transfer function with the appropriate input disturbance spectrum yields the LOS jitter. Table 8 shows the LOS jitter that result from the MWA [37]. Similar information is used in subsequent acquisition LOS jitter calculations and tracking and pointing error calculations.

TABLE 8. LOS Disturbances Due to MWA		
Frequency* (Hz)	North/South (μ rad)	East/West (μ rad)
107	0.440	3.900
214	0.640	0.120
320	0.460	0.180
427	0.006	0.003
rss Total	0.90	3.90
* MWA @ 6400 rpm		

3.4 POINT-AHEAD REQUIREMENT

Another constraint imposed by the orbit in which LITE operates is the necessity to account for the relative motion of the transmitting and receiving platforms in a point-ahead angle requirement [5.8.38]. This is the lead angle by which the outgoing beam must be offset in order to illuminate a moving target. The point-ahead angle can be approximated by the following expression (which assumes a small angle approximation and neglects relativistic terms)

$$PA \approx 2 \frac{V_{\perp}}{C} \quad (2)$$

where V_{\perp} is the component of differential platform velocity which is perpendicular to the LOS. The point-ahead angle between a platform in geosynchronous orbit and a ground station is $\sim 21 \mu\text{rad}$ and does not change with time. The magnitude of the point-ahead angle between a GEO and a LEO platform can be as large as $50 \mu\text{rad}$ ($70 \mu\text{rad}$ for a LEO in a retrograde orbit) and varies as the LEO platform passes from the edge of the earth's disk to directly below the satellite. A point-ahead angle slew rate of $0.5 \mu\text{rad/s}$ and a LOS slew rate of $300 \mu\text{rad/s}$ are sufficient to follow most LEO platforms.

In addition, the tracking system must have enough low-frequency loop gain to track a LEO over $\pm 10^\circ$ or to maintain lock on a GEO at $\pm 90^\circ$.

3.5 ATMOSPHERIC EFFECTS

The ultimate goal of the LITE system is to operate over a space-to-space link. However, as pointed out in the introduction, initial experiments over a GEO-to-ground link are planned. Therefore we will briefly comment on some atmospheric effects that must be considered for optical transmission through the atmosphere.

Atmospheric effects at optical wavelengths can be divided into three categories: absorption, scattering, and turbulence [39,40]. With the exception of clouds, absorption and scattering primarily reduce the received signal power and are very slowly varying functions of time; consequently, with sufficient signal power they can be overcome. To minimize absorption, a wavelength of 860 nm was chosen for the uplink and downlink. A window at this wavelength avoids most of the molecular water absorption lines at shorter wavelengths (i.e., 800 to 840 nm) [41]. Measurements of absorption and scattering indicate that at 860 nm the losses are expected to be less than 1 dB at a good site on a good day (no clouds).

The effect of turbulence on optical beam propagation and communication link performance has been the subject of many studies [42]. For a space-to-space link with small pointing and tracking errors, the signal power at the receiver is relatively constant. However, for transmission through the atmosphere, turbulence can cause significant distortion of the optical beam. For a beam transmitted from a ground site to a GEO satellite receiver, the phase front at the receiver is essentially an ideal plane wave but the power is subject to fades. This is due primarily to two causes. The first is that transmission through the atmosphere (first few kilometers) can corrupt the phase front. The resulting propagation of this corrupted phase front to geosynchronous orbit can be such that it destructively interferes in the far-field, and the receiver experiences a signal power fade. The ratio of transmitter aperture to atmospheric transverse coherence length (d/r_0), plays an important role in determining the statistics of this effect [43]. For a beam transmitted from a GEO satellite to a ground receiver and for relatively small ratios of receive aperture to transverse coherence lengths ($d/r_0 \sim 1$), the receiver experiences phase front fluctuations composed mainly of tilt, the total power being relatively constant [39,43].

The second cause of degradation is that the uplink and downlink beams do not traverse exactly the same paths through the atmosphere due to the point-ahead offset. Hence the tilt correction on the downlink imposed by the ground station may not be completely correct for the uplink. The isoplanatic angle θ_0 , and the antenna beamwidth λ/d , play important roles in determining the statistics of this effect [43]. The differences in atmospheric paths can be compounded by ground tracking and pointing errors.

The LITE ground station location minimizes atmospheric effects by selection of a site at high altitude (to be above the worst of the atmospheric turbulence) and by limiting link operation to "good seeing" periods of the day (typically in the vicinity of dusk or dawn). It is expected that, even at an exceptional site, the atmosphere will meet the good seeing conditions less than 5 percent of the time. Furthermore, even under good conditions, the atmospheric degradation can easily exceed 10 dB [43]. Despite the large amount of research devoted to quantifying atmospheric effects, the present analytic models are imperfect, and thus some uncertainty as to the performance of the communication, acquisition, tracking, and pointing systems in the presence of turbulence remains.

4. SYSTEM DESCRIPTION

4.1 OPTICAL SYSTEM OVERVIEW

A simplified schematic of the LITE OMS package is shown in Figure 13. A more detailed optical prescription is shown in Figure 14, and a pictorial diagram of the OMS is shown in Figure 15. The discussion that follows will briefly describe some of the elements shown in these figures. To achieve the required angular coverage of $\pm 90^\circ$ in east/west and $\pm 10^\circ$ in north/south while satisfying the constraints of package volume and wavefront quality, the system utilizes a coarse pointing mirror (CPM) and a fixed telescope. The CPM design affords an additional 90° rotation in the east/west axis to allow the CPM to rotate into the stow and spacecraft alignment positions. In the stow position, the optical module is partially sealed to minimize contamination during ground testing, launch, and thruster firing during satellite station keeping. Each axis contains a 22-bit inductosyn to provide position and velocity feedback. The east/west motor is a 2-phase 24-pole brushless dc motor. The north/south motor is a limited-angle, permanent-magnet torque motor. Proper bearing selection for the CPM is essential to meeting the performance requirements. Low starting and running torque are critical to minimize LOS jitter during slewing (see Section 4.3) [44-46].

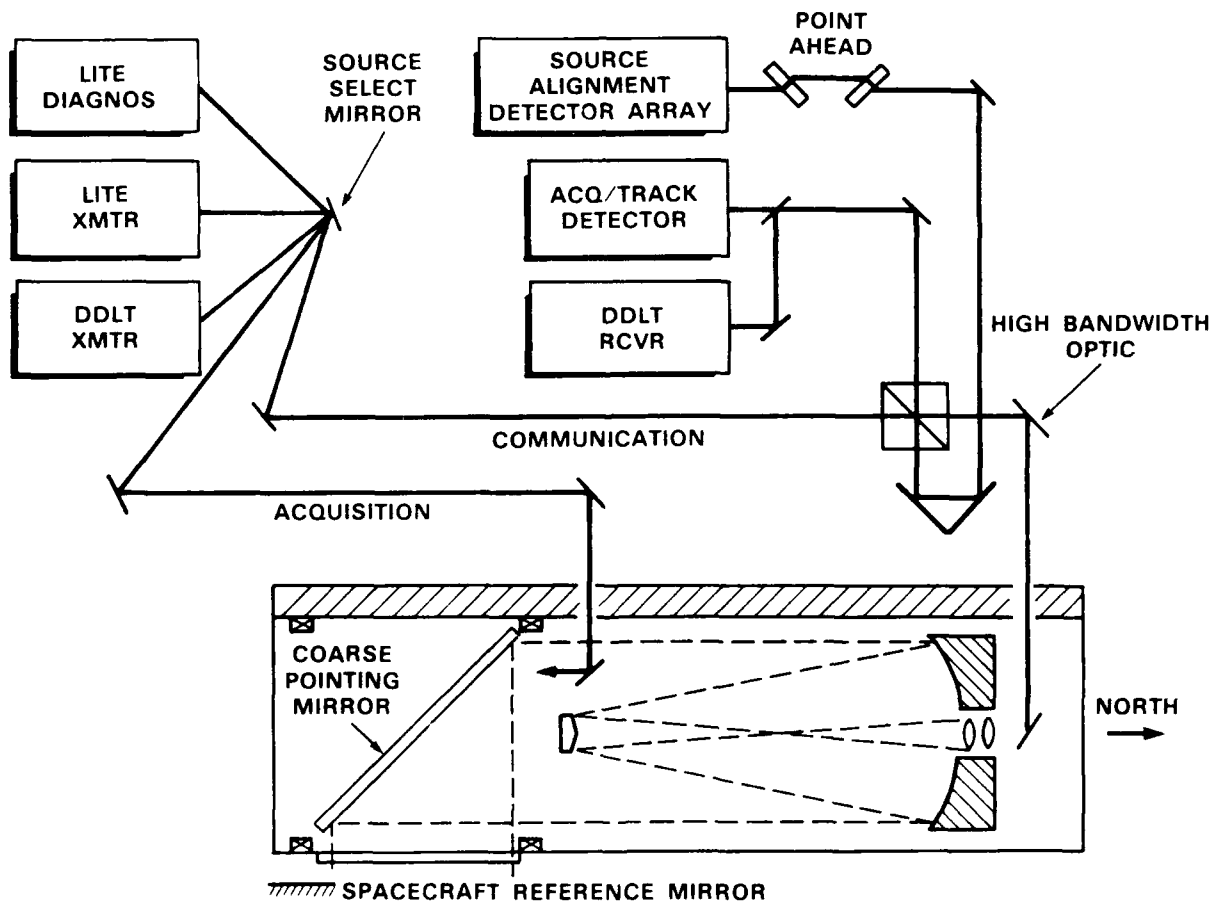


Figure 13. Simplified OMS schematic.

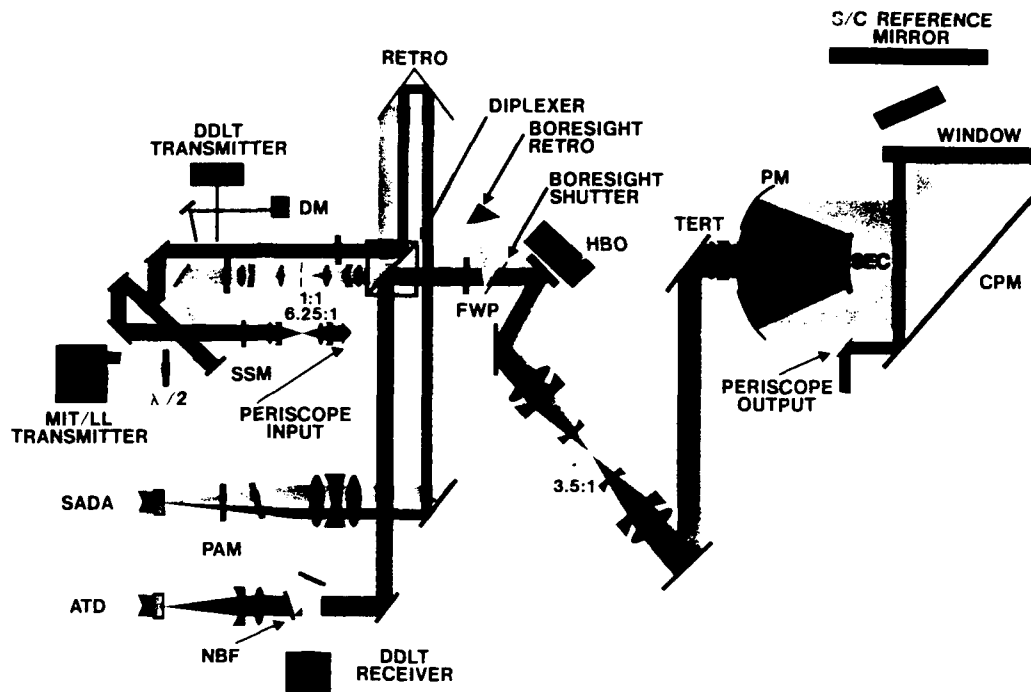


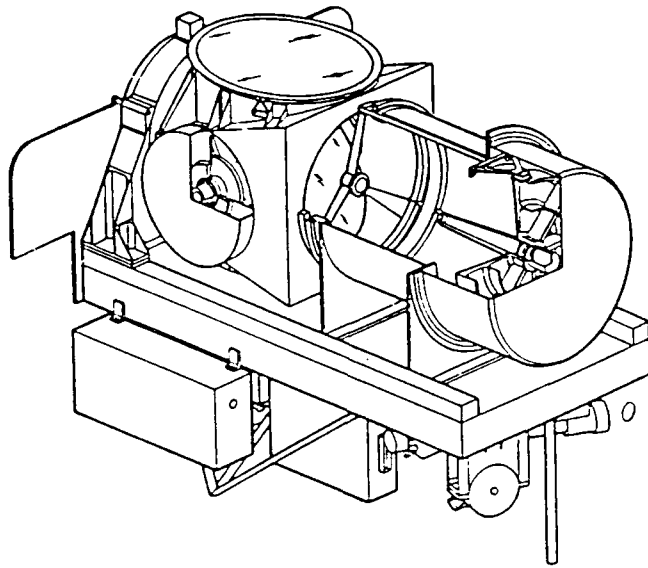
Figure 14. OMS optical prescription.

The CPM is designed with two thin ultralow expansion (ULE) glass facesheets frit-bonded to an egg-crate core in order to make it lightweight, thermally and mechanically stable, and radiation resistant.

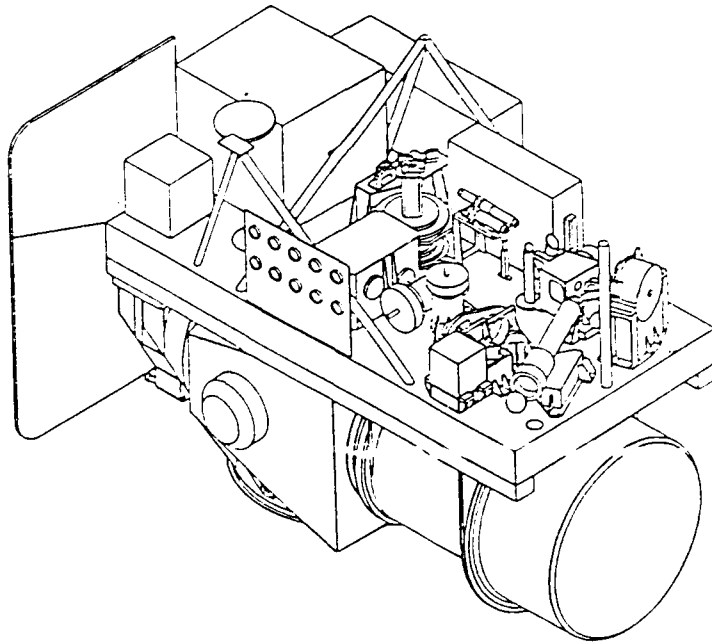
Mounted onto the CPM assembly entrance aperture is a window which is an integral part of the thermal control subsystem. It helps to maintain a constant thermal environment as the sun passes in and out of the FOV. With the sun in the FOV, 80 percent of the incident solar flux is rejected while transmitting 90 percent of the signal energy at the beacon and communication wavelengths.

The telescope is a modified Dall-Kirkham design (ellipsoidal primary and spherical secondary) in that a collimating correction tertiary lens group is included. The entrance pupil is 20-cm-diam. and is located on the $f/1.7$ primary mirror. To maintain the critical primary-to-secondary spacing, super invar metering is used. The telescope has a 15 percent linear obscuration, an afocal magnification of 11.5, and a field stop that limits the FOV to 1.5 mrad (full width). The overall system optical wavefront quality is $\lambda/15$ at $0.86 \mu\text{m}$ with an optical throughput loss of -3.9 dB in the transmit path and -2.5 dB in the tracking receiver path.

As seen in Figure 14, the 3.5:1 relay is next in the optical train. It is used to image the input pupil onto the high-bandwidth optic (HBO) so that pupil walk is minimized. This is important not only for optical



TOP VIEW



BOTTOM VIEW

Figure 15. Top and bottom views of OMS.

106808-17

throughput, but for proper tracking performance as well [3]. The HBO is used to track the received beacon and to scan the acquisition and tracking detector (ATD) FOV during acquisition. During tracking the HBO is controlled by error signals from the ATD, and during acquisition it is controlled digitally by the acq/track microprocessor. The HBO is a two-axis device driven by two pairs of linear voice coil actuators. Each pair is driven in push-pull. It has internal differential eddy current angular sensors, a 1-cm-diameter mirror, a mirror normal angular range of ± 13.5 mrad (local space) in each axis, angular acceleration capability of 15 krad/s^2 , and a -3 dB closed loop bandwidth capability in excess of 5 kHz.

The incoming and outgoing light are orthogonally polarized and are separated via polarization diplexing. The light reflected off the HBO is sent through a quarter-wave plate to convert the incoming circular polarization to linear and the outgoing linear polarization to circular. A polarization diplexer then separates the incoming and outgoing light. The received beacon is sent through a $25\text{-}\text{\AA}$ interference filter and then focused onto the ATD. Incoming light at other wavelengths, such as the DDLT communication beam, is reflected off the interference filter and into the DDLT receiver.

The ATD is a quadrant avalanche photo-detector (APD). An APD was chosen over PIN detectors, photo-multiplier tubes, and CCD detectors since it offers significantly better performance for both acquisition and tracking under the various operational scenarios. A quadrant detector-based tracking system is chosen over detector arrays with more than four elements as well as single element detector (nutaton) tracking systems since it offers essentially optimum tracking performance while providing estimates of tracking errors via simple sum and difference circuits [3]. Unfortunately, there are no commercially available monolithic quadrant APDs that meet our requirements of low noise, narrow dead zone, and gain uniformity. Therefore one is created using an image splitting cube and four discrete detectors. A four-way image splitter is placed in the focal plane along with a pin hole to define the FOV. Four lenses, each placed between the image splitter and the APD, are used to collect the reflected light beams and image a pupil onto each of the detectors. Imaging a pupil (as opposed to focusing) onto each of the four detectors minimizes the motion of the spot across the detector surface and therefore minimizes the effect of gain nonuniformities across the face of the APD.

There are five laser sources. Four are contained in the MIT/LL transmitter and one in the DDLT transmitter. The source select mirror (SSM) is a two-axis mechanism that selects one of the five sources and can route it to one of three paths. The required range of the elevation axis of the SSM is small (± 5 mrad); therefore it is driven with a linear actuator and has a differential eddy current sensor to provide position information. The required range of the azimuth axis is large (52°). The azimuth assembly consists of a precision duplex ball bearing mount, a brushless dc motor, and a 17-bit inductosyn for position information.

There are three optical paths. The first off the SSM is to the diagnostics module (DM). It is used to determine the transmission quality of the MIT/LL sources [47]. The second path is to the periscope and is used during acquisition to spoil the beam to 1 mrad. As discussed in Section 2.3, it is necessary to spoil the beam while scanning the ATD FOV over the uncertainty region. The method chosen to achieve this is to demagnify the selected source, route it around the telescope, and onto the CPM. This avoids complicated

counter scan and zoom lens techniques. The periscope is basically an extended corner cube and therefore is insensitive to alignment errors. The third path is through the telescope. As the outgoing beam passes through the diplexer, a small amount of light (~2 percent) is split off and routed to the source alignment detector assembly (SADA). The SADA is used to stabilize the transmitted beam relative to the ATD and also to implement the point-ahead function.

The SADA and its focusing lens are strategically located next to the corresponding elements in the ATD to minimize the effect of thermal drift and thus maintain the optical alignment of the receive and transmit beams.

The purpose of the point-ahead mechanism (PAM) is to implement the point-ahead function and to allow for boresighting. It consists of two orthogonally mounted 12.5 mm BK7 glass plates. Each plate is driven by a *limited-angle, permanent-magnet, torque motor to provide a range of $\pm 6^\circ$* . Position and velocity sensing is provided by a resolver. As the tilt-plates are rotated, the focal spot is translated at the SADA detector. This displacement is sensed by the SADA error electronics and compensated for by using the SSM. Therefore, as the PAM rotates, a bias or offset is added to the SSM. The PAM provides very high angular gain. For 1 μ rad of far-field displacement, ~1.5 mrad of PAM rotation is required. The actual PAM tilt to focal spot displacement is nonlinear and to minimize the error associated with using this mechanism, a third-order polynomial fit to the nonlinearity was implemented [48]. This high sensitivity and low dynamic range provides better pointing stability than other methods (such as adding offsets directly to the SADA/SSM loop or using translational lens drives). Furthermore, placing the PAM in the SADA path does not introduce additional WFE into the transmitted or received beams. PAM accuracy is listed in Section 4.6.4.

The SADA is similar to the ATD in that it involves an image splitter and imaging lenses. However, since sufficient signal power is available, PIN detectors instead of APD are used. This avoids the need for adjustable high-voltage supplies and reduces sensitivity to temperature and gain uniformity. Also, since the transmitted beam is not intensity-modulated, tracking information is derived at baseband, whereas the ATD receives an intensity-modulated beam.

The following subsections discuss in more detail the operation of this system. They are arranged in an order that mimics the actual system operation, i.e., initialization, alignment, acquisition, hand off, tracking, and pointing.

4.2 SYSTEM INITIALIZATION

This section describes the initialization sequence which follows a power up from standby mode. While in standby mode the entire LITE package is off except for those electronics necessary to keep the optical bench *temperature above the minimum allowable (-20°C)*. This temperature is necessary for the survival of the super-invar elements. After a power-on command, the bench temperature and temperature gradients are stabilized, and the link management processor is initialized. This is necessary to minimize thermally induced distortions and misalignments which contribute to both WFEs and pointing and tracking errors. Thermal stabilization takes ~30 to 50 min. General housekeeping functions are performed during this interval, including calculation of the ephemeris and scan generation look-up table, and the selection and stabilization of the transmit laser.

4.3 ALIGNMENT

Possible changes in alignment due to launch loads, as well as thermal and mechanical on-orbit disturbances, dictate the need for an on-orbit alignment capability. The four major tasks discussed in this section are (1) to internally align and stabilize the laser source; (2) to align the transmit and receiver paths (boresight); (3) to align the transmit path to the spacecraft; and (4) to align the acquisition path to the spacecraft.

The first step in aligning and stabilizing the laser source is to locate it on the SADA. To do this, the acq/track microprocessor commands the PAM to its electrical null and the SSM to point the selected laser to the SADA. The SADA pointing information is contained in memory. Each time the selected source is located and centered on the SADA, its previous position information is updated with the new location information, if necessary. The pointing information accuracy and the system thermal and mechanical stability, combined with the large SADA FOV (± 4.9 mrad) ensure that the selected source will land on the SADA. However, the system has the ability to scan the selected source with the SSM to locate the signal on the SADA. Once signal power is detected on the SADA, control of the SSM is switched to the SADA error signals.

The purpose of the SSM in this mode is to internally stabilize the source with respect to the SADA. Electrical and optical block diagrams illustrating the concept of the SSM control loop are shown in Figures 16 and 17, respectively.³ The loop bandwidths must be sufficient to overcome both the low-frequency rigid

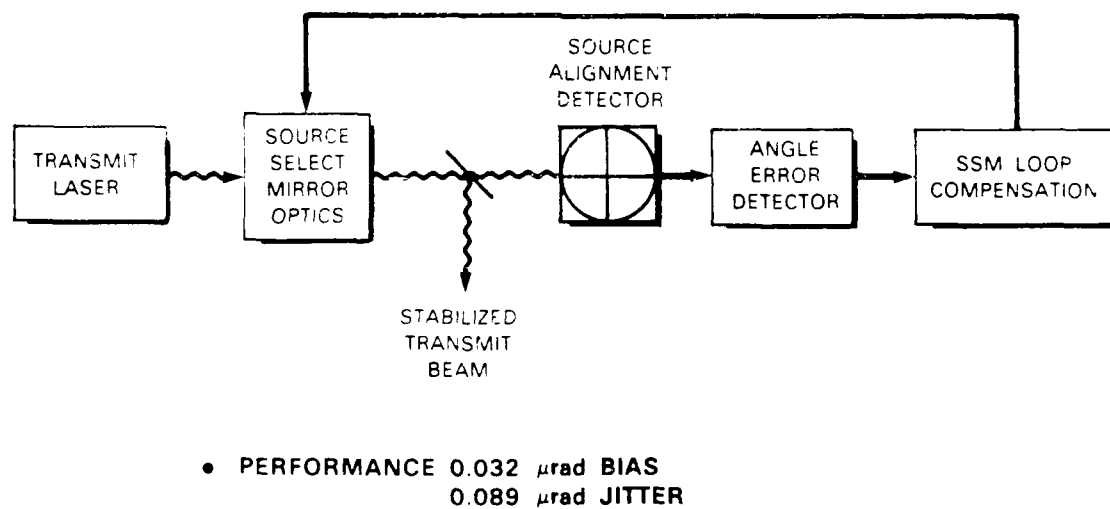


Figure 16. Source stabilization loop block diagram

³ The electrical block diagrams shown here and elsewhere are often conceptual in nature in that certain optical paths have been simplified. The optical diagrams are often closer to actual hardware.

body modes and the high-frequency vibrational modes of the SSM, transmitter housing, and various optical components. Under microprocessor control, the SSM has 50-Hz position loops in both axes and a 400-Hz velocity loop in the azimuth axis. The position loop bandwidth is limited by the update rate of the microprocessor under loading. Under SADA control the elevation axis position bandwidth is increased to 500 Hz. However, a structural resonance at ~ 1 kHz does not allow the azimuth bandwidth to be increased. The LOS pointing jitter due to linear and rotational disturbances at the base of the SSM, as well from other angular disturbances such as the transmitter housing, were analyzed using NASTRAN and played through the servo system to predict the contribution to LOS jitter (see Section 4.6.4). The limitation of a 50-Hz position loop during acquisition resulted in a large MWA-induced jitter (see Table 9).

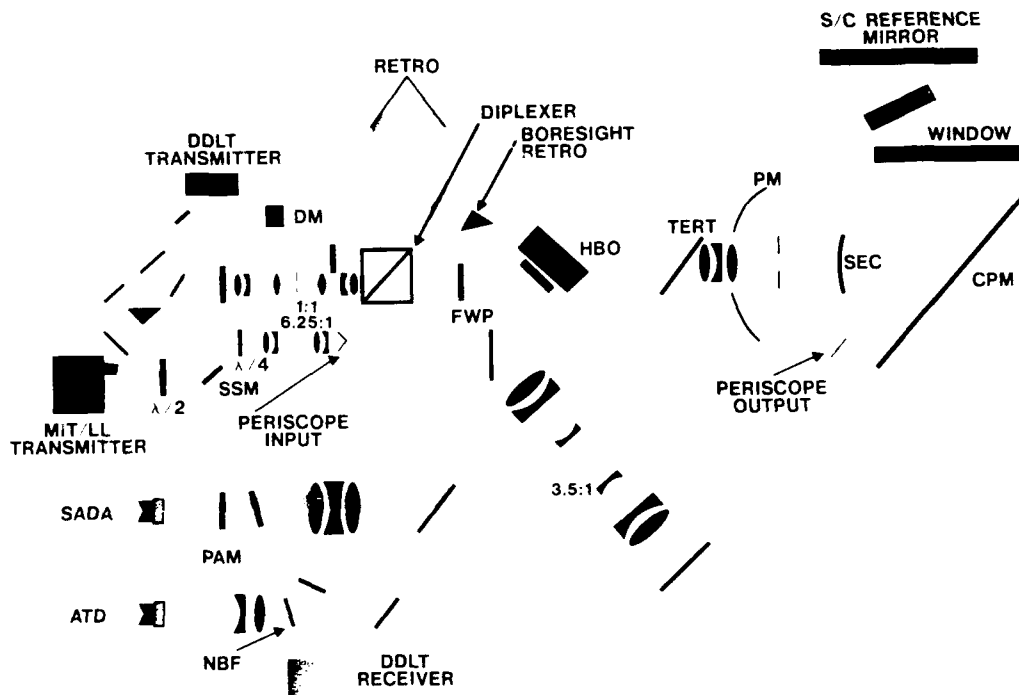


Figure 17. Source stabilization loop optical diagram.

Now that the source is internally stabilized, it must be aligned to the receiver path. This boresight procedure is begun with a command to rotate a mirror, located after the $\lambda/4$ plate, into the transmission path. This mirror directs the light onto a retroreflector. The reflected light therefore has the same polarization as the received beacon and is directed to the ATD. The mirror is designed to attenuate the reflected light to a power level comparable to the received beacon. The alignment tolerances are such that with high probability the light should focus onto the ATD. If not, the light can be scanned using the PAM to locate the signal on the ATD.

Once signal power is detected on the ATD, the gains of the four front-end channels must be balanced. Each APD can have a slightly different gain dependence on bias voltage and temperature. At high APD gains, small differences in these parameters can lead to large differences in APD gain [49,50]. Furthermore, not all the effects of aging and radiation on the parameters of the APD have been quantified [51]. This, combined with the stability and accuracy of the gains of the front-end transimpedance amplifiers (TIAs) and bias voltage supplies, lead to the need for autonomous gain balancing.

TABLE 9.	
Periscope-to-Spacecraft Alignment Accuracy	
	(μ rad)
Spacecraft Reference Mirror	50.00
CPM Accuracy	48.33
Position Accuracy	29.00
Servo Error	16.00
Structural Drift	10.00
Bearing Runout	32.00
Orthogonality	10.70
Alignment Residual	56.62
CPM Azimuth Resolution	0.75
CPM Elevation Resolution	1.50
SSM Azimuth Resolution	21.70
SSM Elevation Resolution	42.80
SADA	30.00
Jitter	57.93
Azimuth Servo	1.40
Elevation Servo	2.80
Structural Vibration	2.50
SSM Elevation	57.40
SSM Azimuth	7.13
rss Total	106.76

Before error signals can be generated by the ATD, the transmitter laser must be intensity-modulated at 54 kHz to be detected by the receiving electronics. To balance the front-end gains, the bias voltage corresponding to the desired gain for APD No. 1 is found using a look-up table. This bias voltage is applied to all four APDs. The signal power incident on APD No. 1 is maximized by monitoring the voltage (at 54 kHz) out of the corresponding TIA and using a hill-climbing algorithm and the microprocessor to steer the

PAM. Once the signal is peaked, it is stored as a reference for the other three channels. The signal out of the next channel to be balanced is peaked using the same algorithm. Once peaked, the bias voltage is servoed until the output voltage is equal to the reference voltage. The gain balancing procedure is adequate to set the average gain of the four channels to within ± 10 percent of the desired gain and the gain of an individual channel to within ± 2.5 percent of the average gain. The temperature stabilities of the ATD and bias voltage supplies are sufficient to ensure that their contribution to tracking system bias remains less than $0.086 \mu\text{rad}$ per axis (see Section 4.6.4).

Once the front-end channels are balanced, the boresight procedure can be completed. Electrical and optical block diagrams illustrating the concept of the boresight loop are shown in Figures 18 and 19, respectively. To achieve boresight, the transmit beam must be simultaneously centered on the SADA and ATD. To accomplish this, the PAM is slaved to the ATD error signal via a digital loop that involves the microprocessor. Once the beam is centered on the ATD, the position of the PAM is measured and stored as the zero reference for the point-ahead angle. The accuracy with which the ATD and SADA can be aligned is dependent on many factors. These are enumerated in Section 4.6.4, but a detailed discussion of the individual items is beyond the scope of this report.

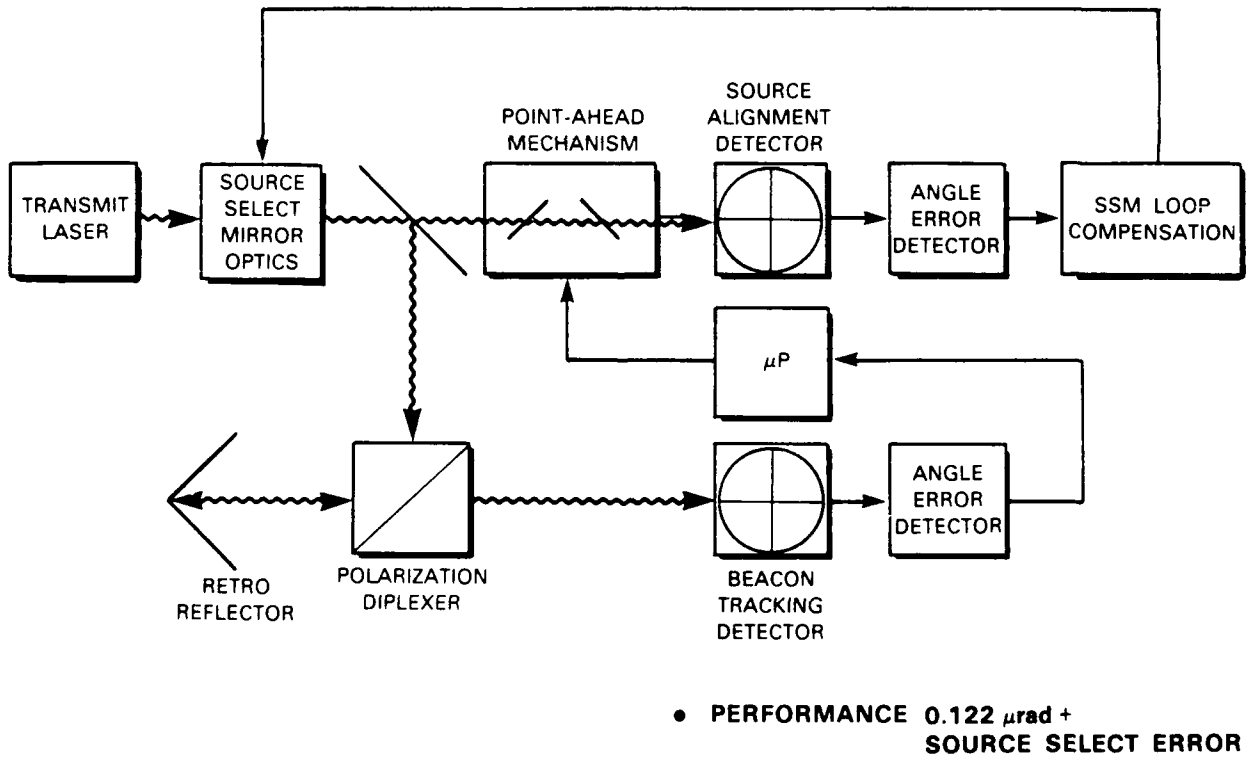


Figure 18. Boresight system block diagram.

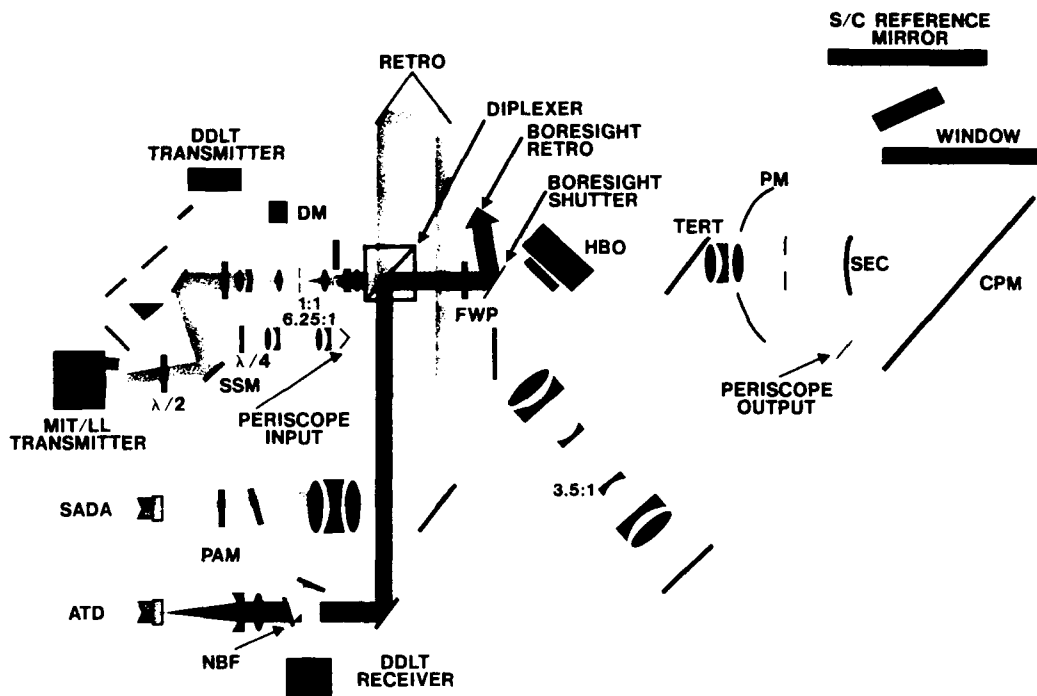
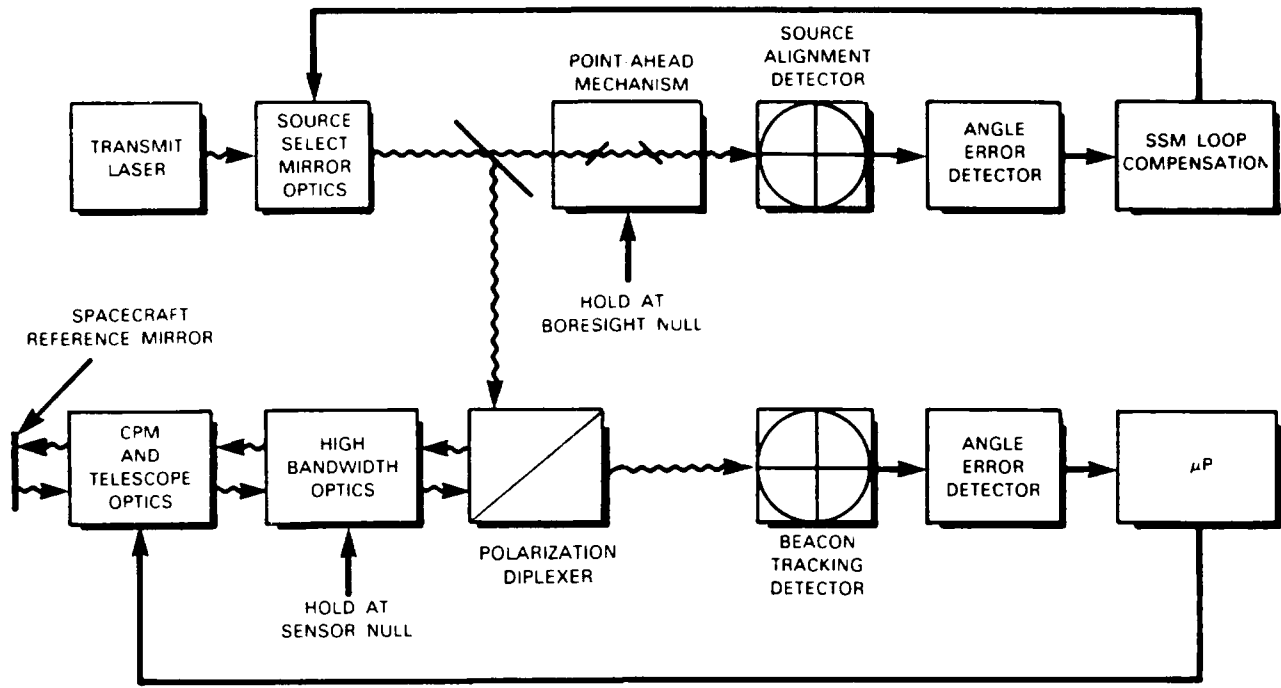


Figure 19. Boresight optical diagram.

Once boresight has been accomplished, the transmission path is aligned to the spacecraft (Figures 20 and 21). The CPM is moved from its stowed position to point the LOS to a reference mirror located at the OMS/spacecraft interface. The reference mirror is located at the base of one of the interface struts which is next to a spacecraft alignment cube. Also located close by is the earth sensor assembly (ESA) reference used by the spacecraft attitude control system. The close proximity of the reference mirror to the ESA helps ensure that proper alignment to the spacecraft axes is maintained in the presence of thermal changes. An acquisition scan is then implemented to locate the return from the reference mirror with the ATD. The acquisition scan algorithm is discussed in Section 4.4. To achieve power levels comparable to the received beacon, the reference mirror diameter is sized to be 4 cm and a neutral density filter is placed in the alignment path. Once the reference mirror is located, the CPM is slaved to the HBO position signal. When the HBO reaches its null, the CPM position is sampled and used as zero point reference for subsequent open-loop pointing. The estimated accuracy with which the transmit path can be aligned to the spacecraft is equal to 86 μ rad. Table 10 lists the some of the dominant factors that determine this accuracy.

112043-8



● PERFORMANCE 86 μrad

Figure 20. Telescope LOS-to-spacecraft system alignment block diagram.

TABLE 10.	
Telescope-to-Spacecraft Alignment Accuracy	
	(μrad)
Spacecraft Reference Mirror	50.00
CPM Accuracy	48.33
Position Accuracy	29.00
Servo Error	16.00
Structural Drift	10.00
Bearing Runout	32.00
Orthogonality	10.70
Alignment Residual	1.68
CPM Azimuth Resolution	0.75
CPM Elevation Resolution	1.50
Telescope LOS Change	50.00
rss Total	85.66

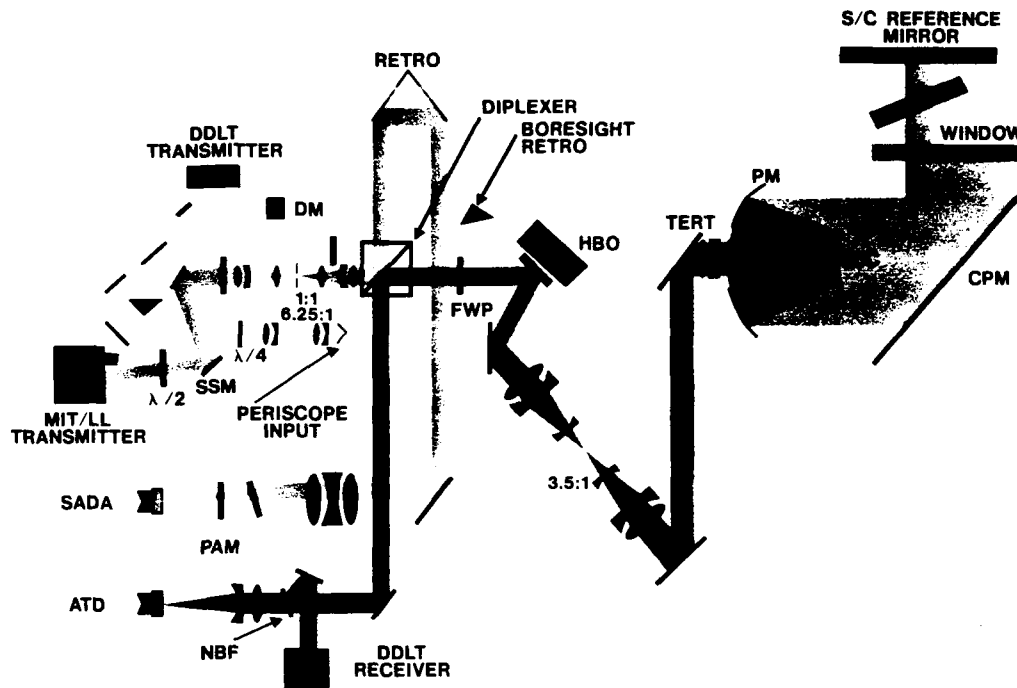
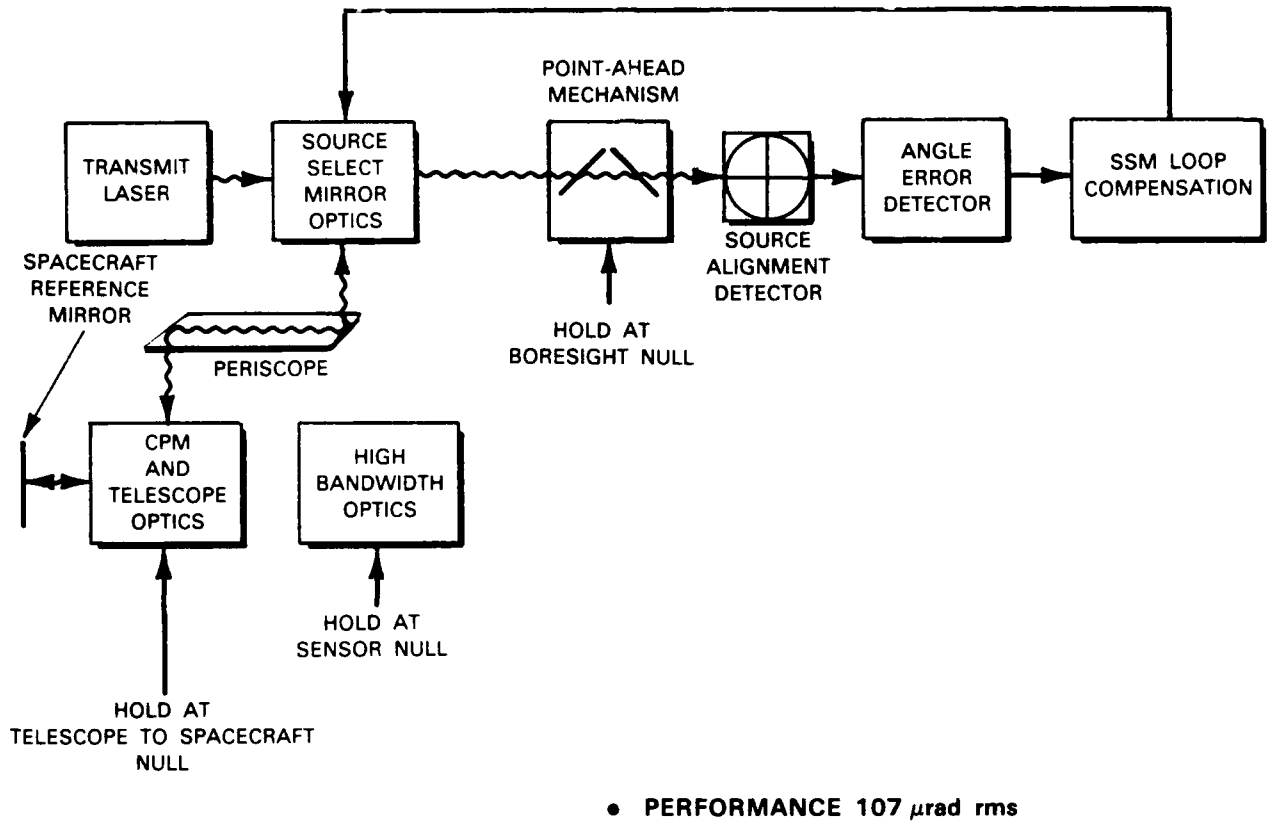


Figure 21. Telescope LOS-to-spacecraft optical diagram.

Now that the transmit path has been aligned to the spacecraft, the acquisition path must be aligned (conceptually shown in Figures 22 and 23). This is accomplished by directing the source through the periscope, off the reference mirror, and back onto the SADA, while the CPM is held in its reference position. A polarization diplexer and the $\lambda/4$ plate separate the transmitted and reflected light. The SADA focusing lens and the PIN detectors are sized to accommodate the lateral shift in the beam from its nominal nonspoiled beam mode. The SADA FOV and the open-loop pointing accuracy of the SSM should be sufficient to ensure that the return from the reference mirror will be immediately detected on the SADA. However, a scan for the return can be implemented using the SSM.

Upon detecting a signal on the SADA, control of the SSM is switched from the microprocessor to the SADA. Once the beam is centered on the SADA, the position of the SSM is monitored. The SSM then redirects the light from the acquisition path to the telescope path where the SSM/SADA control loop is reestablished. The increment in the SSM position from the telescope path to the acquisition path is stored

for use during acquisition. Storing the increment in the SSM position rather than the SSM position itself, helps minimize drift errors during the time it takes the CPM to slew to its targeted position (~30 min). Table 9 lists acquisition path alignment accuracy and some of the dominant factors determining the periscope alignment accuracy.



106808-5

Figure 22. Acquisition LOS-to-spacecraft system alignment block diagram.

4.4 SPATIAL ACQUISITION

4.4.1 Overview

The acquisition system on ACTS has two major functions: (1) to illuminate, with a beacon, the uncertainty region containing the other terminal, and (2) to detect and locate the return beacon from that terminal so that a handover to the LITE spatial tracking system can be performed. This section focuses primarily on the second task.

A spiral scan search is performed by using the HBO to scan the FOV of the APD acquisition detector. The angular dimensions of the spatial region, which is both illuminated and scanned, are determined by the a priori uncertainty in the location of the other terminal. Section 4.4.2 gives a budget for the spatial

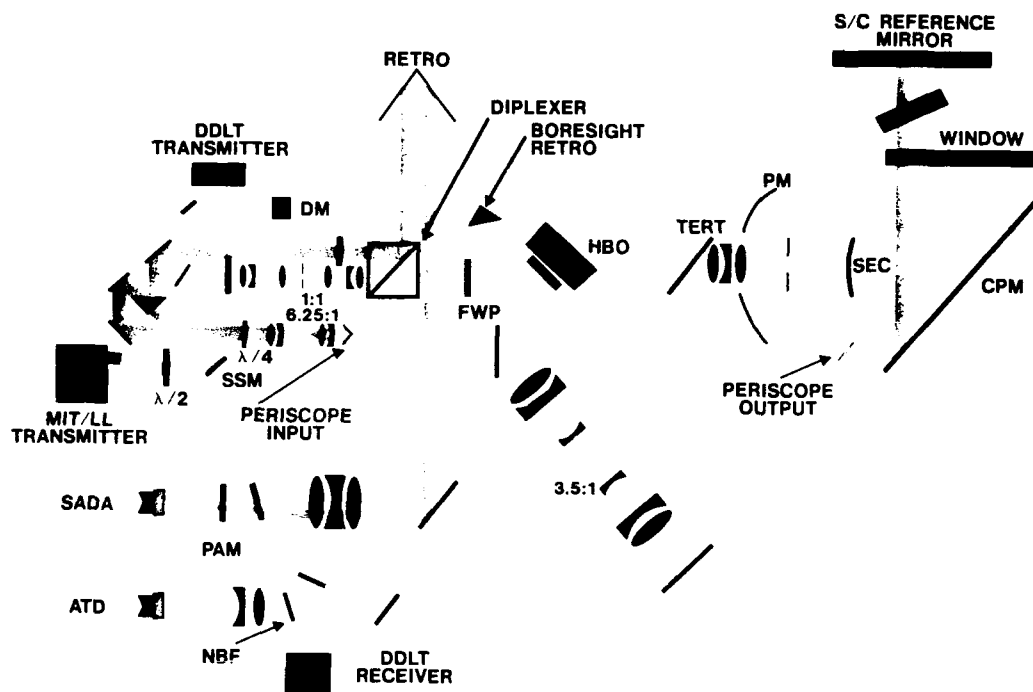


Figure 23. Acquisition LOS-to-spacecraft system optical diagram.

uncertainty. The output of the detector is passed on to signal detection electronics, and the position of the HBO when a hit is detected gives the location of the detected beacon. Acquisition strategy is discussed in Section 4.4.3, with details of the acquisition system implementation described in Section 4.4.4. Detection performance depends upon many variables, including received signal power, the various sources of noise, and LOS jitter. Section 4.4.5 gives the detection analysis.

106791-3

4.4.2 Angular Uncertainty Budget

The angular range which must be searched depends upon the a priori pointing uncertainty which arises from a variety of sources. Here we give the budget for open-loop angle uncertainty between ACTS and a receiving station, and discuss the variables which influence pointing accuracy. For purposes of analysis, angular errors have been divided into three categories: (1) biases which are stable in orbit but are not known or predictable prior to launch; (2) long-term errors which are defined as the time-averaged angle deviation of the platform attitude, where the average is taken over the duration of the longest anticipated acquisition (several minutes) after subtracting biases; and (3) short-term errors, referred to here as "angle jitter," representing angular deviations occurring within an acquisition time interval. Acquisition angle uncertainty is related mainly to long-term error and thus the uncertainty budget given here includes only that. It is assumed that biases can eventually be estimated and calibrated out on-orbit after performing many acquisitions. The residual long-term errors then represent unknown, slowly varying deviations in angle which appear essentially fixed over the course of a single acquisition but may vary from one session to the next. Short-term errors are manifested as line-of-sight jitter during the course of an acquisition scan and are dealt with separately.

In order to compute a best-estimate initial pointing angle for the target terminal, orbital elements for both ACTS and the terminal are supplied as inputs to an on-board spatial acquisition processor (SAP), which performs an orbit-fitting routine and computes pointing angles. Errors in orbit-fitting of ACTS translate to an estimated pointing error of 0.1 mrad (see Table 6). An error of 0.1 mrad is representative of the accuracy of moderate-complexity orbit-fitting programs which can be accommodated by the SAP. If the other terminal is a LEO satellite, another ephemeris-related issue of on-board clock accuracy must be considered. That is, if the computed pointing angle for a specific time is not implemented at the correct instant because of time-of-day errors at the satellite, an additional pointing error is incurred. For example, the angle slew rate of a LEO terminal as seen from ACTS can be as high as 250 $\mu\text{rad/s}$. A 0.1-s clock error then results in a 25- μrad pointing error. For a geostationary-to-geostationary link, however, the pointing angle is nominally time-invariant and clock accuracy is thus not an issue. In practice, imperfect station-keeping results in some residual drift in the satellite orbit and thus some small angle slew rates may be encountered. Open-loop pointing error accounts for the CPM open-loop pointing accuracy, that is, the difference between commanded and realized open-loop pointing angles. The error includes effects of CPM-to-spacecraft alignment and errors intrinsic to the CPM (see Tables 9 and 10).

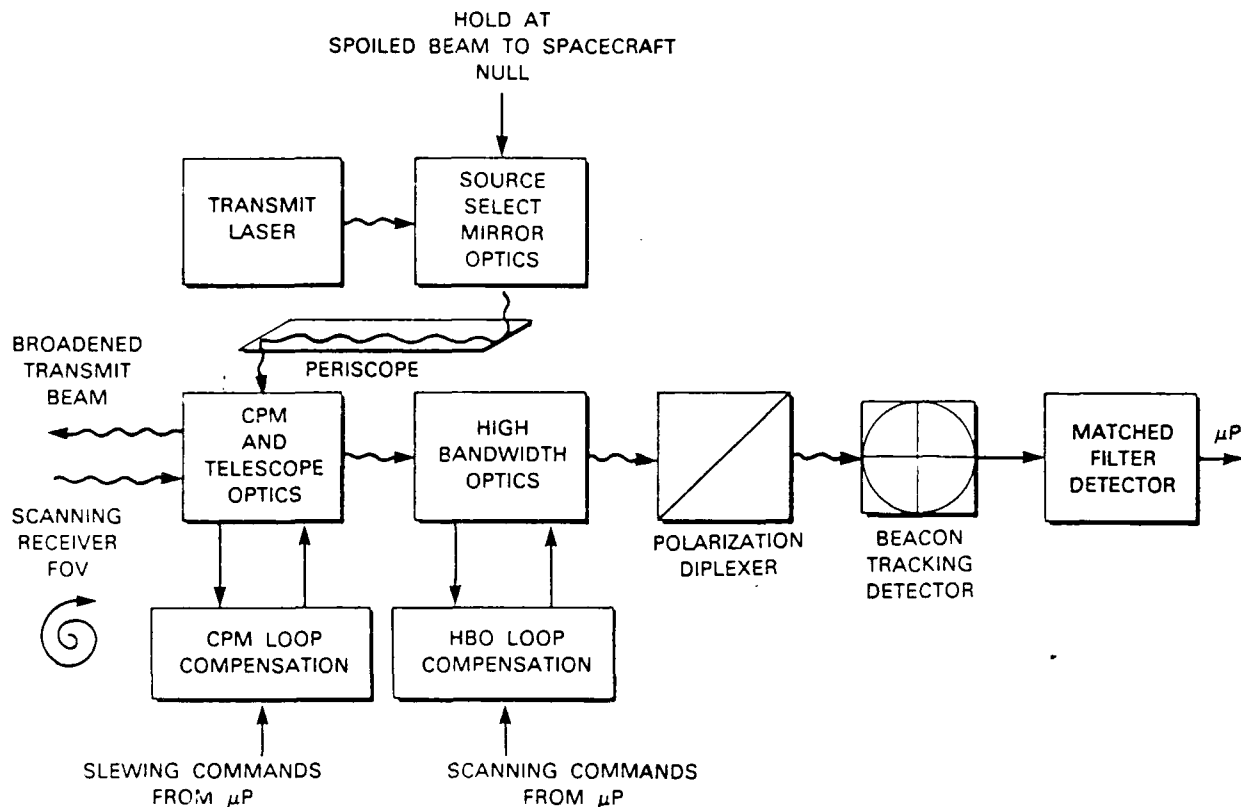
The dominant term in the budget is spacecraft attitude control accuracy. Even if satellite ephemeris is known perfectly, uncertainty in the attitude of the platform with respect to inertial space produces uncertainty in pointing. Table 6 gives the best- and worst-case numbers over which ACTS attitude control performance can vary. For an ACTS-to-LEO link, pointing is relatively insensitive to yaw error. The indicated attitude control numbers are representative of the performance of a well-designed geosynchronous satellite, assuming a star tracker is not employed. A resulting rss total of 0.60 mrad best case and 2.50 mrad worst case (omitting yaw errors) are acquisition spatial uncertainty bounds.

4.4.3 Acquisition Strategy

As shown in Figure 2, the ACTS terminal initiates the acquisition sequence by illuminating the uncertainty region with the transmit beam broadened to 1-mrad FWHM, corresponding approximately to the best case total spatial uncertainty specified in Table 6. The other terminal acquires the beam and after a detection is made, points a return beacon in the estimated direction of ACTS. This beacon is pointed open-loop since the received power density of the spoiled received beam is too small to initiate closed-loop tracking. Because of residual pointing uncertainties at the other terminal at the completion of acquisition, the return beacon at this stage is broadened to 18 μ rad to minimize signal power loss at ACTS due to pointing errors. A broader beam would have a larger loss at the receiver from the increased beam divergence, whereas a narrower beam would suffer greater pointing losses. In the case of a LEO terminal, the effects of LEO platform instabilities on uplink pointing and ephemeris uncertainties in maintaining open-loop pointing when slewing is involved must be considered in the selection of the uplink acquisition beamwidth.

After a time-out period of a few seconds, during which the receiving terminal search is completed and the return beacon is sent out, spatial acquisition is initiated on ACTS. The HBO performs a spiral scan beginning at the center of the region being illuminated. The use of the periscope approach, by which the transmit beam bypasses the HBO, allows the receive FOV to be scanned while at the same time maintaining fixed pointing of the 1 mrad transmit beam as the other terminal waits for ACTS to acquire the beacon. Electrical and optical diagrams illustrating the concept of the acquisition system are shown in Figures 24 and 25, respectively. The spiral angular diameter is 1.25 mrad, which allows for a small amount of over-scanning of the illuminated area. In the acquisition mode, the outputs of the four quadrant APDs are summed together and provide a circular FOV of 20- μ rad diameter. The value of this FOV is a compromise between acquisition and tracking requirements, given that both systems have been constrained to employ the same detector. A smaller FOV is optimum for tracking whereas a larger FOV would reduce scanning time in acquisition.

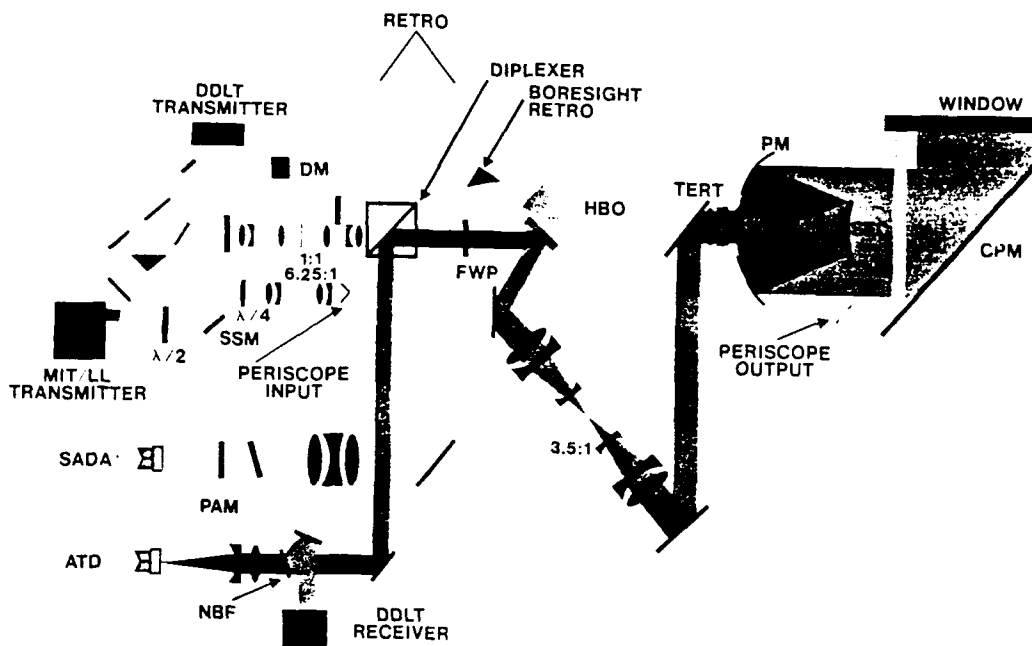
The scanning rate is set by command to one of three values: 10, 40, or 160 mrad/s tangential velocity given in terms of rate of coverage of angle in object space. (A fourth velocity of 2.5 mrad/s is reserved for the dither scan which is discussed below.) The lower velocities provide longer dwell times to increase margin when necessary. Also, to fill in gaps in coverage caused by LOS jitter, scanning redundancy is introduced by overlapping successive tracks of the spiral. Overlap can be set to 5, 10, or 15 μ rad.



106808 4

Figure 24. Acquisition system block diagram.

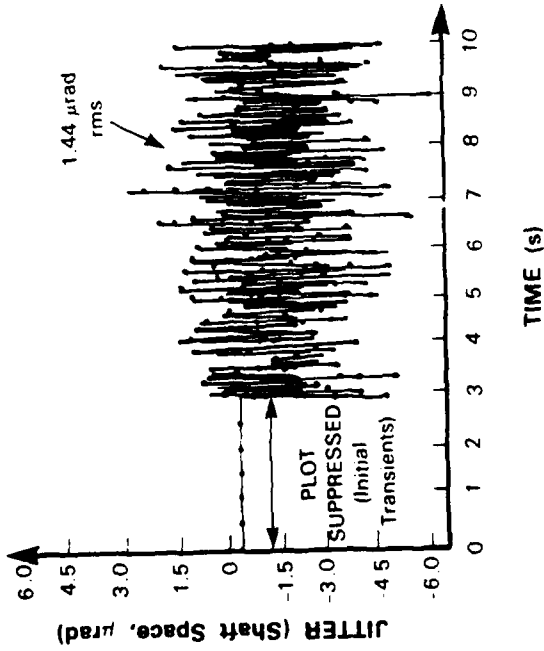
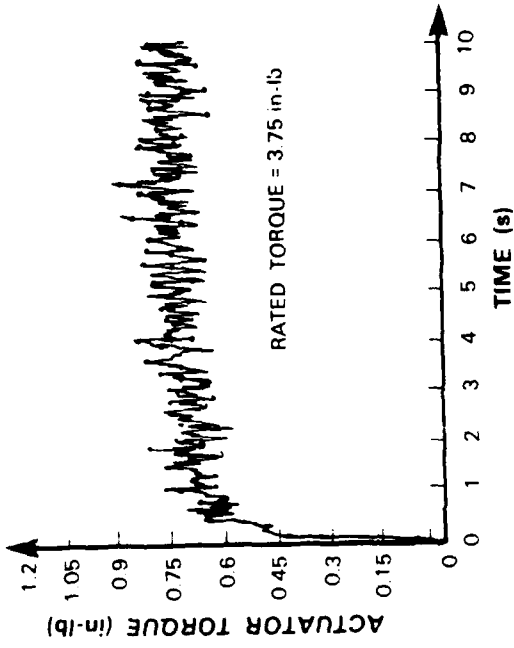
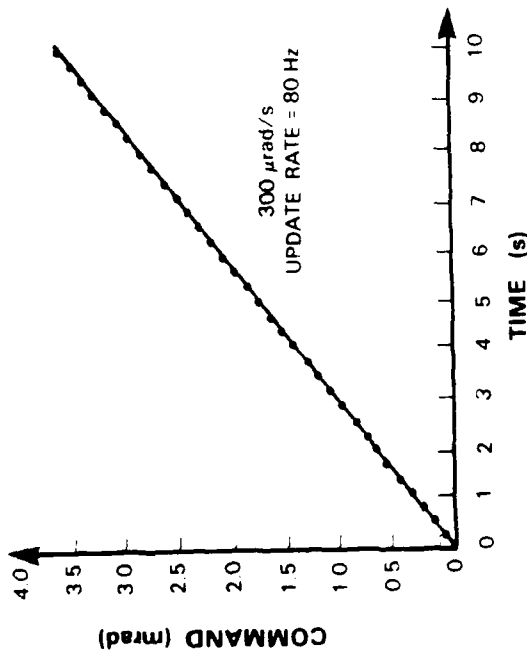
Table 11 lists the LOS jitter during acquisition. The MWA and gyro components were discussed in Section 3.3. The CPM and HBO servo components were derived from computer simulations and measured laboratory results [52]. They are the result of both mechanical and electrical imperfections in the respective servo systems. Bearing variabilities are a main source of CPM servo jitter, and quantization and sensor noise dominate the HBO servo jitter. Figure 26 shows some of the simulation results for azimuth CPM jitter while slewing at $300 \mu\text{rad/s}$. Note that the $3.1 \mu\text{rad}$ entry in the budget allots for an equal amount of jitter in the elevation axis (which is optically multiplied by a factor of two). The reaction torque components are due to uncompensated torques coupling into the various mechanical modes resulting in the LOS jitter. The actual values are difficult to calculate since it requires coupling the NASTRAN models with the servo modes. In addition, the values depend on what mode the OMS is in (i.e., acquisition or tracking). The entries for these components were allotted the remainder of the budget. However, some analysis was completed to show that indeed these are safe upper bounds to the actual values.



106791-2

Figure 25. Acquisition system optical diagram.

TABLE 11.		
Line-of-Sight Jitter During Acquisition		
Source		Budget (μ rad)
Spacecraft	MWA	4.0
	Gyro	2.0
ServoCPM	3.1	
	HBO	1.0
Reaction Torques	CPM	2.1
	HBO	0.2
Total (rss)		6.0



CPM JITTER IS WITHIN BUDGET

**BEARING NOISE AND VELOCITY SENSOR NOISE INCLUDED
COMMAND AND ERROR QUANTIZATION AND UPDATE RATE
INCLUDED
SATURATION NONLINEARITIES INCLUDED
CONTROLLER STAGE OUTPUTS WITHIN SPECIFICATION LIMITS
BEARING NOISE BANDWIDTH USED WAS 12 Hz, BASED ON
MEASUREMENTS AT 0.5 rpm AT 20 mrad/s (0.19 rpm);
BEARING NOISE BANDWIDTH LESS AND SERVO
REJECTION RESULTS IN JITTER VALUE < 1.44 μ rad**

Figure 26. CPM μ -mrad jitter performance

The return beacon is intensity-modulated with a 54-kHz square-wave to shift the signal as detected at the APD output away from dc and low frequency disturbances such as APD dc dark current, background photo-current, and various 1/f-type noises in the front end, all of which would impair signal detection. A frequency of 54 kHz was available from an existing source and was high enough to avoid these problems, but not so high as to stress receiver front-end bandwidth requirements. At the receiver, only the fundamental frequency of the modulation is used for detection, which is carried out by bandpass matched filters centered at 54 kHz. The use of square-wave instead of sine-wave modulation of the beacon laser transmitter has the advantage of better utilization of semiconductor laser peak-power limitations (the fundamental-frequency power is greater in the squarewave than a sine wave for the same peak power) and the minimization of frequency-chirping and possible mode-hopping of the laser under modulation.

Signal detection is performed by passing the summed APD outputs into a bandpass matched filter centered at 54 kHz. The filter bandwidth is matched to the duration of the expected signal pulse produced by scanning the detector FOV over the target source at the specified rate. For example, with a 20- μ rad FOV and a scan rate of 160 mrad/s, the pulse duration is about $(20 \mu\text{rad} \div 160 \text{ mrad/s}) = 125 \mu\text{s}$. The corresponding filter bandwidth is then $(125 \mu\text{s})^{-1} = 8 \text{ kHz}$, although the exact, optimal bandwidth depends upon the actual filter transfer function. For example, with a second-order bandpass (i.e., the bandpass equivalent of a two-pole lowpass) Butterworth implementation, a width of about 7.6 kHz is close to optimal. Three matched filters are provided for the three possible scan rates. The post-filter signal-detection logic can be operated in either a threshold-detection or pick-maximum mode.

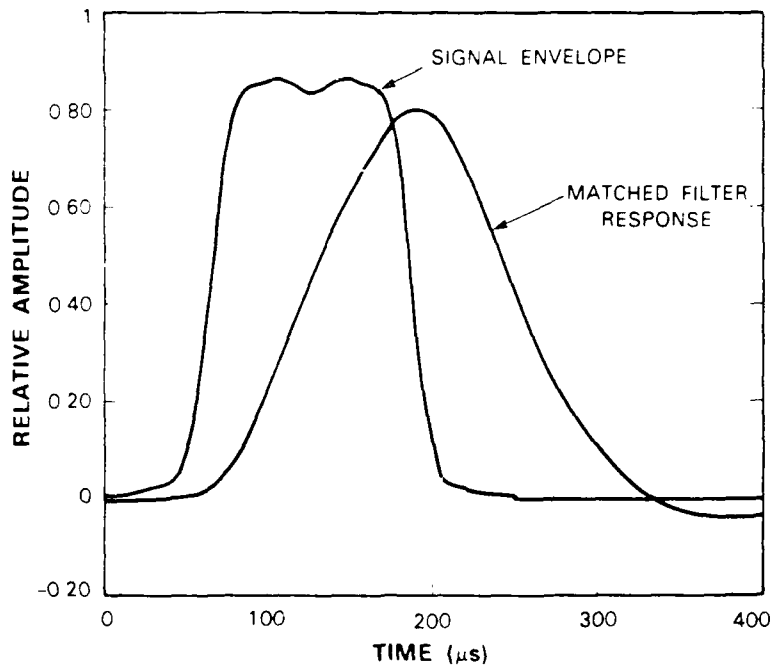


Figure 27 Acquisition signal and matched filter response.

The actual shape of the pulse envelope which is produced by scanning the received spot across the center of the detector at 160 mrad/s is illustrated in Figure 27. (For other scan rates, the pulse duration scales inversely to the scan rate.) This is a calculated result which takes into account the actual detector size and shape, the beam diffraction pattern profile, and a small dead zone in the quadrant APD. In this figure, a normalized amplitude is shown - a pulse height of unity is obtained only for an infinitely wide detector with no dead zone. The indicated maximum pulse amplitude of less than one is attributable to the finite detector size and the resultant loss of some signal power beyond the edges and within the dead zone of the APD. The baseband power spectrum of the pulse envelope is shown in Figure 28. A -3-dB bandwidth of slightly less than 4 kHz is observed. Note that if the scanned spot is offset from the center of the detector, then the received pulse is somewhat shortened temporally, and its spectral bandwidth is increased slightly. Also shown in Figure 27 is the calculated response of the two-pole Butterworth matched filter to the pulse.

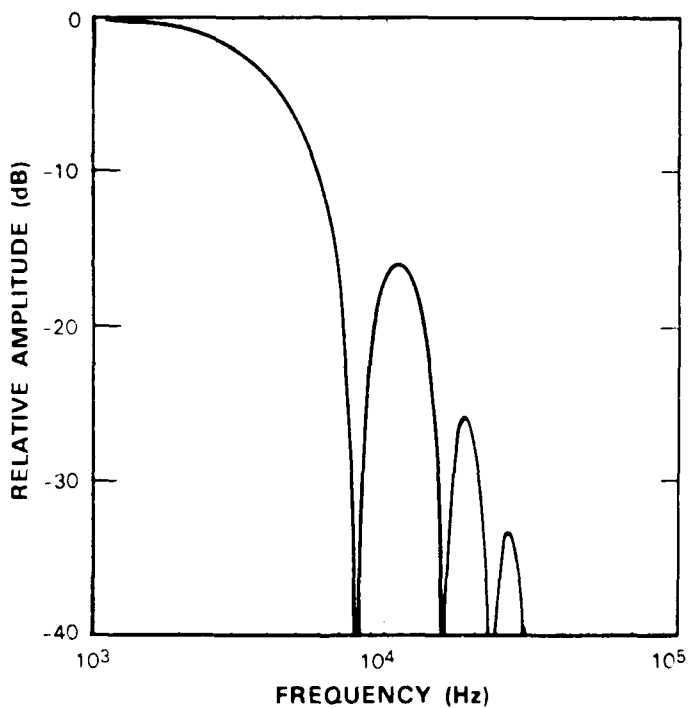


Figure 28 Acquisition signal spectrum

In threshold detection, a threshold level is computed before the start of acquisition based on a measurement of receiver front-end noise. During the search, the scan is stopped each time the matched-filter output exceeds the threshold and the hit is investigated a second time by means of a dither scan which provides a simple and robust transition to tracking and a means of recovering from any false alarms. The dither scan is a spiral of 100- μ rad diam., centered at the observed hit location. Since the main scan cannot stop instantaneously at a hit but, instead, overshoots the location and must back up, the dither provides considerable tolerance for error in returning to the actual hit location in attempting to relocate the beacon. Figure 29 shows an example of this acquisition scan where the error in the return to the hit location has been exaggerated. If a second hit is observed during dither, a hand over to the tracking loop is immediately triggered. The dither uses only the smallest scan velocity of 2.5 mrad/s to allow adequate time for the tracking loop to pull in while the target is still in view. The dither scan uses the maximum overlap of 15 μ rad and takes ~ 0.6 s to reach its maximum diameter of 100 μ rad. If a second hit is not obtained during dither, the first is assumed to have been a false alarm and the acquisition scan resumes from that hit location. The probability of two successive false alarms - in the main scan and immediately afterwards in the dither - is made negligible by choosing the detection threshold to provide a suitably small false alarm rate. Thus in the threshold-detection mode, the search terminates after the first valid detection before the entire spiral has been scanned. Since the target is generally more likely to be found near the center of the uncertainty region, the combination of spiral scanning and threshold detection usually provides for more rapid acquisition than the alternate pick-maximum mode.

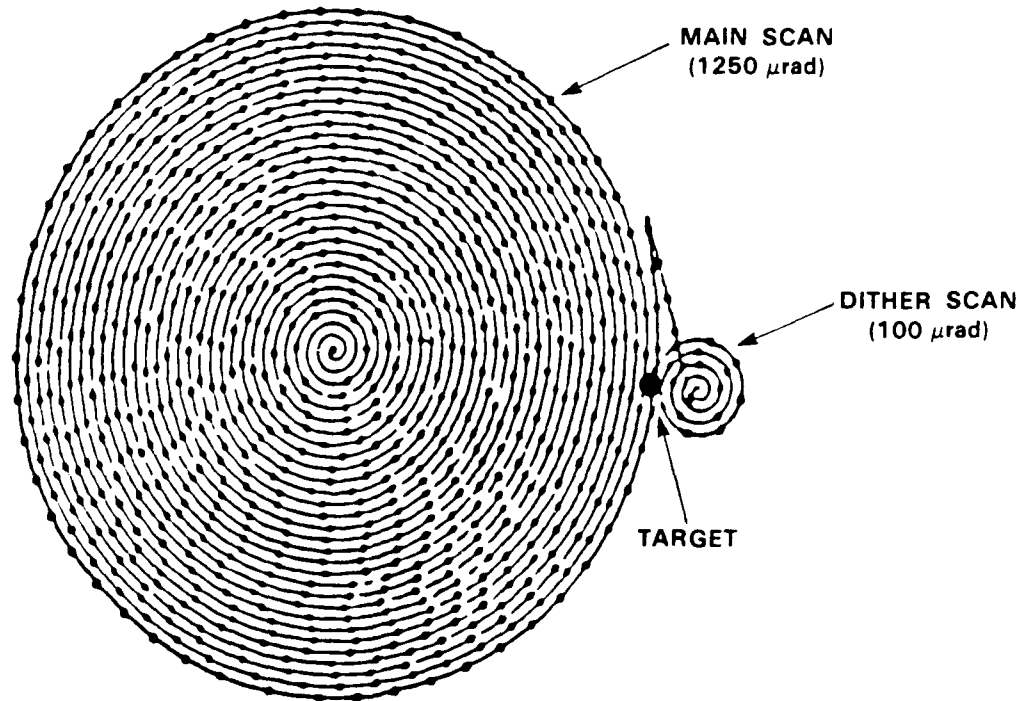


Figure 29 Main and dither scans for acquisition threshold detection.

In the pick-maximum approach, the entire uncertainty region is scanned, looking for the largest matched-filter output over the whole region. At the conclusion of the scan, the HBO is returned to the location where the largest output was observed, and the dither scan is initiated as in threshold detection. In the dither scan, a threshold value based on the magnitude of the largest recorded matched-filter output is calculated and a hand over to tracking is initiated if the threshold is exceeded. If no hit is observed, the acquisition search is resumed. This mode holds a possible advantage in certain scenarios in which, in the threshold detection mode, the system may attempt to lock onto false sources such as stars. However, because the acquisition beacon is expected to be stronger than most stars, the pick-maximum mode will correctly choose the beacon over stars. Based on a calculation using statistics of star brightness, in a region of the size being scanned (~ 1 mrad), the probability of a star intensity exceeding that of the acquisition beacon in a 25-Å filter is on the order of only 10^{-3} [53].

If the target is located within the region being illuminated and searched, the acquisition should be completed after one spiral scan. On the other hand, if the other terminal is not contained within the region, the first acquisition attempt will fail with high probability since the mispointed acquisition beam will prevent the other terminal from acquiring the beam and, in turn, prevent ACTS from acquiring the returned beacon. If no successful acquisition and hand over is accomplished after the first spiral scan, the CPM is repointed to a predetermined adjacent region and the whole process of illumination and search is repeated until a detection occurs (Figure 30). This process is carried out autonomously without intervention by ground control. It was deemed impractical to increase the transmitted beam divergence and the size of the spiral scan to cover the worst-case uncertainty in a single search because of (1) an unacceptable loss of acquisition margin due to the reduction in received signal power density, which falls off as the square of beamwidth, and (2) angular dynamic range limits of the HBO, relay lenses, and telescope.

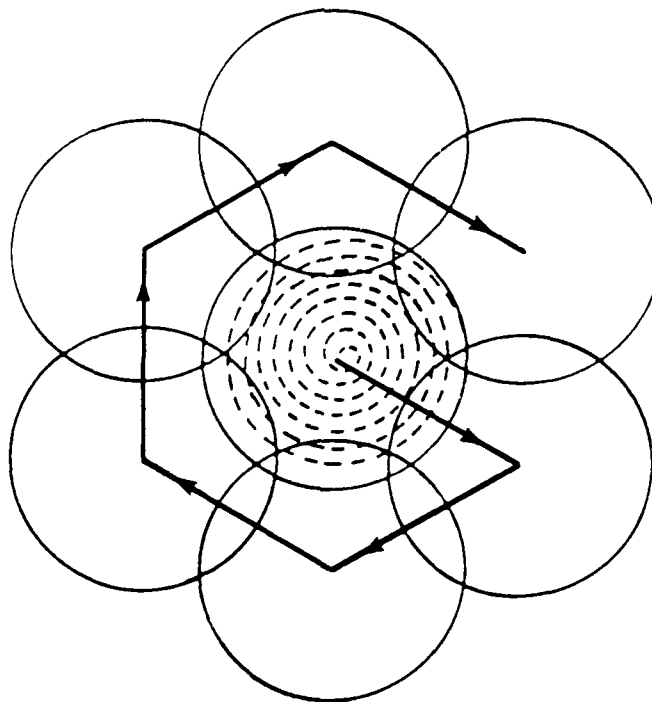


Figure 30. Multiple region acquisition scan

4.4.4 Implementation

In this section we describe the implementation of the hardware in the acquisition system. The front-end detection hardware (four-quadrant splitter, APDs, TIAs, and sum/difference amplifiers) are common with the tracking system, and are described in Section 4.5. Here we focus on the hardware unique to the acquisition process. These areas include the matched detection filters, the decision logic, the threshold setting logic, and the acquisition scan generation hardware. The acquisition electronics are shown in Figure 31.

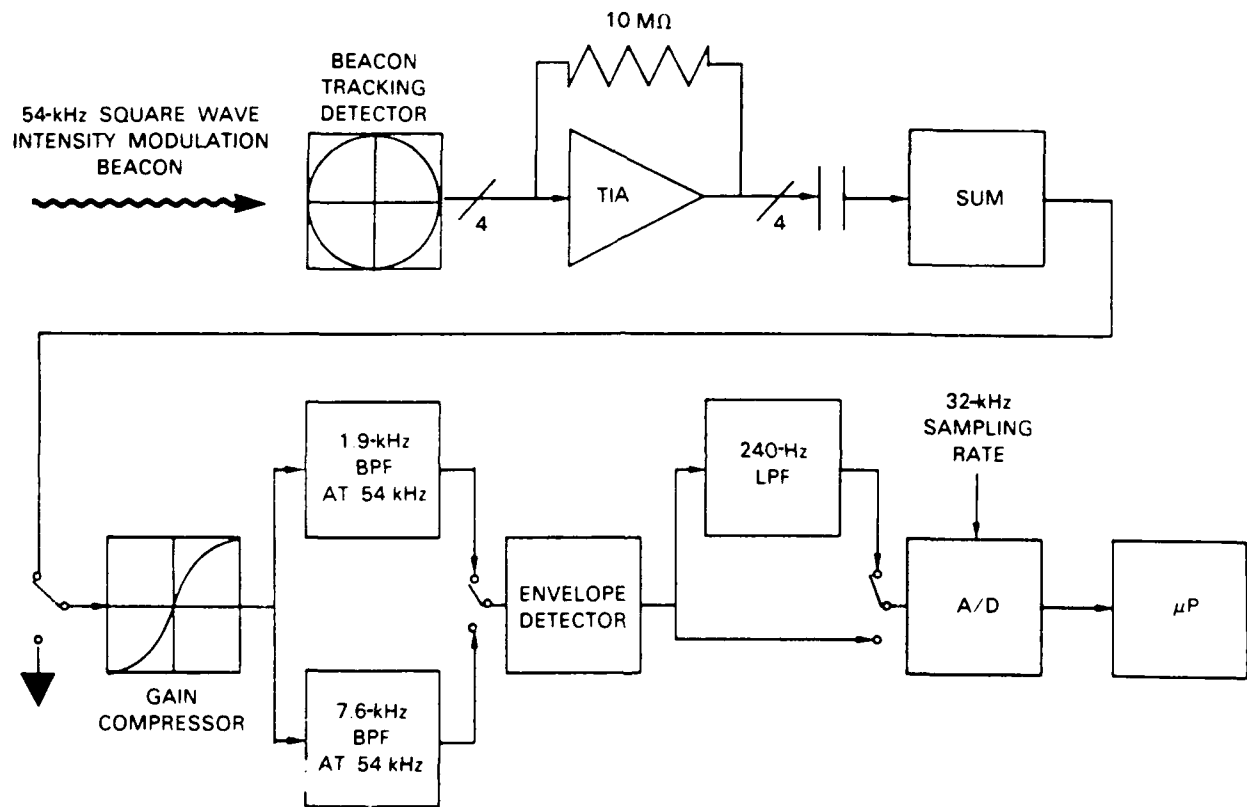


Figure 31. Acquisition system signal processing.

106808-22

The acquisition detection electronics are designed to amplify and detect a 54-kHz pulse the width of which varies from 125 μ s to 8 ms, depending upon the scan rate during the search. To attain robust acquisition performance, the electronics are designed to operate over a signal power dynamic range of 60 dB. This ensures sufficient range to accommodate a combination of pointing errors, receiver locations, and transmitter power variations.

Gain compression is used in the first amplifier of the acquisition section in order to reduce the dynamic range seen by the demodulation and detection circuits. The compression is shaped to keep noise from being nonlinearly amplified at the lowest signal levels and to keep the detection circuits from saturating on the highest signal levels. The compression curve is piecewise linear, and has three separate gain regions, 450, 50, and 0.

A combination of bandpass and post-detection low-pass filters is used. The signal path is chosen to provide filtering matched to the pulse shape produced by scanning the FOV through the received beacon at one of the four available scan rates. Bandpass filtering alone followed by envelope detection is used for the two fastest scan rates (160 and 40 mrad/s). For either of the two slowest scan rates (10 and 2.5 mrad/s), an additional post-detection low-pass filter is used to further narrow the detection bandwidth (Table 12).

TABLE 12.					
Matched Filter Characteristics					
Mode	1	2	3	4	Dither
Scan Velocity (Object Space)	160 mrad/s	40 mrad/s	10 mrad/s	2.5 mrad/s	2.5 mrad/s
54-kHz Butterworth Bandpass Filter Bandwidth (-3dB Full Width)	7.6 kHz	1.9 kHz	1.9 kHz	1.9 kHz	Same as Main Scan
Post Detection Lowpass Filter Bandwidth (-3dB Half Width)	None	None	240 Hz	240 Hz	Same as Main Scan

The matched filter output is converted to a 12-bit digital word at a 31.25-kHz rate. After each conversion the resultant digital word is compared to a reference value. For threshold detection the reference value is the value set according to preacquisition receiver noise estimates. During threshold detection the reference value is not changed during the course of acquisition. During pick-max detection the reference

value is always the largest matched filter output since the start of the acquisition scan. Whenever a larger value occurs, it replaces the previous reference value. For each type of hit detection logic, signals are generated which initiate sampling of the scan position at the instant of the hit detection.

Because the mirror acceleration is excessive near the center of the scan if a constant velocity scan is commanded, the scan is modified such that the tangential velocity ramps from zero to the preset velocity as the radial distance of the FOV increases from zero to 200 μ rad (32 percent of the total scan pattern radius). Such a soft start limits the maximum drive frequency in either the azimuth or elevation channels to \sim 150 Hz (see the Appendix).

Commands are calculated prior to the start of the scan and stored in a digital look-up table. The velocity ramp is built into the stored commands. When the scan begins, the azimuth and elevation position commands are read out at a uniform 4-kHz rate, converted to analog voltages in a pair of 12 bit D/As and sent to the azimuth and elevation HBO position servos. If a slower scan velocity than the maximum 160 mrad/s rate is desired, the same look-up table is used. Commands are read out from the table at 1 kHz, 250, or 62.5 Hz, and digital interpolation is used to fill in the gaps so that fresh azimuth and elevation position commands are still sent to the mirror position servo every 250 ms.

The response of the mirror position loop exhibits 20 to 30 percent peaking between 150 and 250 Hz. Because this peaking would cause unacceptable distortion in the spiral scan pattern, an analog prefilter is inserted after the D/A conversion, to cut the gain in the command path. The overall closed loop gain distortion is held to within \sim 1 percent from dc to 500 Hz.

For the threshold-detection mode, the value of the threshold is determined by a semi-adaptive procedure. Prior to the start of each acquisition, a large number of samples of the front-end noise are taken at the output of the acquisition processor to form estimates of the mean and rms values. The CPM is in its stowed position at this time so that any externally introduced background noise is negligible, and only APD dark current noise and front-end electronics noise are measured. The threshold is then set equal to a scaled multiple (which can be varied) of the estimated noise standard deviation to obtain the desired false alarm rate. Because background noise is not included in the noise estimate, the actual noise levels are underestimated when a strong background, such as daytime earth, is actually present during acquisition. However, in the following section, it is shown that even the worst-case earth background of daytime snow and ice causes only a slight increase in total receiver noise. A real-time running average adaptive threshold was considered for dealing with time-varying background levels, but was eventually discarded because of its additional complexity and only modest projected improvement in performance over the present fixed-threshold mode.

4.4.5 Performance

In this section, an analysis of acquisition performance is given. The emphasis is on a statistical characterization of both the threshold-detection and pick-maximum modes of operation. The effects of LOS jitter are also discussed. Since performance depends upon received signal power and total noise, these two parameters are quantified first. A budget for the LEO-to-ACTS link is presented in Table 13.

The post-APD electrical rms signal power, P, in the 54-kHz fundamental-frequency component of the square-wave intensity modulated beacon the detected signal is given by

$$P = \frac{1}{2} \left(\frac{4}{\pi} m G \frac{\eta e P_s}{h \nu} \right)^2 \quad (3)$$

where η is the quantum efficiency of the APD, e is electronic charge, $m < 1$ is the modulation index of the 54-kHz component, G is the APD gain, P_s is the average optical power of the signal incident on all four APDs, h is Planck's constant, and ν is the optical frequency.

TABLE 13.	
LEO-ACTS Acquisition Link Budget	
Transmit Laser (dBW)*	-18.2
Transmit Optical Losses	-4.6
Laser Module Phase ($\lambda/20$)	-0.4
Laser Module Amplitude (EOL)	-0.3
Optical Train Phase Loss ($\lambda/15$)	-0.8
Optical Train Amplitude Loss (EOL)	-1.7
Obscuration (15% linear + spiders)	-1.3
Polarization Error (15°)	-0.1
Beam Spoiling (18 μrad)	-15.9
20 cm Transmit Aperture Gain (Ideal)	117.3
Spatial Pointing Loss	-1.9
Space Loss (42700 km)	-295.9
20 cm Receiver Aperture Gain (Ideal)	117.3
Receiver Optical Losses	-2.5
Obscuration (15% linear + spiders)	-0.1
Optical Amplitude Loss (EOL)	-1.8
Polarization Error (15°)	-0.1
Interference Filter (25 Å)	-0.5
Detected Power (dBW)	-104.4
Number of Photons/s at Detector (dB-Hz)	82.0
Losses	-1.8
Implementation	-1.0
Finite Detector Size	-0.8
* 15 mW average power (30 mW peak power)	

Noise at the receiver arises from several sources: shot noise from signal and background radiation, APD dark current noise, and front-end electronics noise. In the frequency band of interest around 54 kHz, the noise in the sum of the four APD channels can be modeled as spectrally white with the following density (single-sided) [49]:

$$N_o = 2e \{ FG^2 [\eta e (\frac{P_s}{h\nu} + \lambda_b) + 4 I_{db}] + 4 I_{ds} \} + 4 N_c \quad (4)$$

where F is the excess noise factor of the APD, λ_b is the rate parameter of the background radiation incident on all four APDs, I_{db} is the gain-dependent component of a single APD's dark current (usually the bulk-generated current), I_{ds} is the gain-independent component of a single APD's dark current (usually the surface-generated current), and N_c is the effective (single-sided) current noise of one channel of the front-end electronics. The excess noise factor F is given approximately by

$$F = kG + (2 - \frac{1}{G}) (1 - k) \quad (5)$$

where k is the APD ionization rate ratio. The APD gain G can be chosen to optimize detection performance (Section 4.6). In practice, however, the performance turns out not to be a strong function of the gain and a single fixed value of gain is near-optimal for the scenarios of interest. $G = 100$ is used in the numerical calculations.

The background rate parameter λ_b is scenario dependent and can be time varying. Among natural sources of background radiation, the sun is the strongest source of noise. For acquisition of an earth or LEO terminal, we shall be concerned with the earth as a background. (A LEO satellite at the edge of the earth can appear with the sun in the background, but this infrequent event is ignored in the present acquisition discussion.) Radiation from a nighttime earth background consists primarily of earthshine (thermal radiation emitted by the earth and its atmosphere) and reflected moonlight. In a 20- μ rad FOV and a 25- \AA filter in the 0.8- μ m region, the received nighttime background level is so low in comparison with other sources of noise that it can be considered to be essentially zero [54]. On the other hand, the daytime earth background radiation is dominated by sunlight reflected from the earth's surface or from clouds. For diffuse scattering, a background of winter snow and ice has the highest reflectance around 0.8 μ m, producing a worst-case spectral irradiance $N(\lambda) = 25 \text{ mW cm}^{-2} \text{ sr}^{-1} \mu\text{m}^{-1}$ [see Reference 54]. A spectral irradiance of $N(\lambda) = 1800 \text{ W cm}^{-2} \text{ sr}^{-1} \mu\text{m}^{-1}$ is used for the sun [54]. The background rate parameter λ_b is given in terms of $N(\lambda)$ by [55]

$$\lambda_b = \left(\frac{\pi}{4} \right)^2 \frac{1}{h\nu} \Delta\lambda \theta_r^2 D^2 N(\lambda) L_r \quad (6)$$

where $\Delta\lambda$ is the optical filter pass-band width, θ_r is the angular FOV of the detector, D is the aperture diameter, and L_r is the receiver throughput loss.

Table 14 summarizes the numerical data used to calculate the total system noise in the acquisition analysis. The APD parameters were obtained by laboratory measurements of the RCA C30902S APD [51]. The values listed are conservative and in addition assume a worst-case operating temperature of 35°C. For the anticipated operating temperature of 21°C, the gain dependent dark current would be a factor of ~4.6 lower and the gain independent dark current a factor of ~3.3 lower [50].

TABLE 14.	
Acquisition and Tracking System Noise Parameters	
Wavelength, λ_s	0.86 μm
Telescope Diameter, D	20 cm
Quantum Efficiency, η	0.80
Gain Dependent Dark Current, I_{db}	0.052 pA
Gain Independent Dark Current, I_{ds}	6.8 nA
Ionization Rate Ratio, k	0.02
Acquisition APD Gain	100
Tracking System APD Gain Range	1-200
TIA Input Current Noise Density, N_c	$2.2 \times 10^{-27} \text{ A}^2/\text{Hz}$
Modulation Depth	1.0
Interference Filter Bandwidth, $\Delta\lambda$	30 \AA
Detector FOV, θ_r	20 μrad
Background Rate Parameters:	
Solar Background	$6.5 \times 10^{11} \text{ s}^{-1}$
Strong Daytime Earth Background	$8.0 \times 10^6 \text{ s}^{-1}$
Nighttime Earth Background	0 s^{-1}
Background Throughput	5.5 dB
* includes polarization (-3 dB) and throughput (-2.5 dB) attenuation in calculations	

The preceding APD noise parameters do not account for the effects of radiation. Preliminary experimental measurements of radiation from the natural environment indicate two dominant effects on the APD [51]. The first is increased noise due to increased gain-dependent dark current as a result of bulk damage in the active region of the APD. The second is an increase in noise due to radiation-induced photocurrent. Bulk damage is a "total dose" effect that gradually takes place over the operational lifetime. It is anticipated that at the end of a four-year lifetime a small amount of shielding will keep the APD exposure to less than 50 krad (Si), causing a decrease in acquisition and tracking signal power link margins of between 1 and 4 dB (depending on the received signal level and background). The more serious problem is the uncertainty

in the effects of radiation-induced photocurrent. Although its level is relatively low even during magnetic storms (< 4.4 pA primary current in active region), the impulsive nature of the current (which can easily be 1000 primary electrons/event in the active region depending on the radiation type energy) is of concern. This effect is more difficult to quantify since it is a probabilistic phenomenon that is very dependent on the exact nature of the external radiation environment, the type of shielding, the acquisition and tracking algorithms, and the signal power level. Further work to quantify both of these effects remains to be done.

The acquisition detection analysis is simplified by approximating the statistics of the total noise as Gaussian. In reality, the APD-generated component of the noise has a non-Gaussian distribution [49,56] while the front-end electronics noise is well modeled as Gaussian.

The threshold-detection mode of acquisition is considered first. The problem is to detect a signal of unknown arrival time. Although the arrival time gives the spatial location, it is not necessary to estimate it with great precision. For our purposes it is sufficient to determine only that the signal is present so that the main scan can be stopped and the dither scan started. Detection performance is measured in terms of probabilities of detection and false alarm. The statistics of the output of the matched-filter/envelope detector output are Rayleigh when only noise is present and Rician (or noncentral Rayleigh) when both signal and noise are present. If signal arrival time were known, it would suffice to take a single sample of the matched-filter/envelope detector output at the instant the signal component peaks. Performance of threshold detection systems using single-sample observations is well known [57]. Because arrival time is unknown, the approach taken here is to monitor the output continuously for a threshold crossing and, in effect, many samples are observed.

The probability of detection P_D at large signal-to-noise ratios can be approximated accurately by the detection probability of a system where signal arrival time is known [58]. If the signal is large enough to be detected with high probability at the instant where a sample would be taken with arrival time information, it is also large enough to cause the threshold in the present system to be exceeded since the threshold corresponds to a level much smaller than the expected peak of the signal. For an ideal matched filter, P_D can then be expressed in terms of the well-known Marcum Q-function.

$$P_D = Q(a, b) \quad (7)$$

$$Q(a, b) = \int_b^\infty r \exp\left[-\frac{(r^2 + a^2)}{2}\right] I_0(ar) dr \quad (8)$$

where $a = \sqrt{E/N_0}$, E being the peak detected electrical signal energy ($E = 2P\tau$), for rms signal power P , signal duration τ (assuming a square pulse), and $b = \rho/\sqrt{N_0 B}$, where ρ is the detection threshold and B is the matched filter noise bandwidth. In practice, the detection filter is not perfectly matched to the signal - the signal itself is not completely deterministic since the exact temporal characteristics of the received pulse depend upon what portion of the APD array the target crosses, and the implementation of the filter used in the ACTS/LITE

system is actually a second-order Butterworth approximation of an ideal matched filter. Therefore the value of the signal energy-to-noise density ratio E/N_0 as used above will be degraded somewhat (~ 1 dB) from the ideal.

The probability of a false alarm occurring during the course of the *entire* search depends upon the search duration T . To avoid dealing with a random T , we calculate the false alarm probability P_{FA} using a worst-case T , namely the time required to complete an entire scan of the 1.25-mrad-diam. region. (The possibility of needing to scan multiple regions is ignored for now.) At a single instant in time, the probability P_{FA} of a false alarm is

$$P_{FA} = \int_b^{\infty} r \exp\left(-\frac{r^2}{2}\right) dr \quad (9)$$

$$= \exp\left(-\frac{b^2}{2}\right) \quad (10)$$

Exact calculation of P_{FA} for continuous-time observations is complicated. One approximation for the probability of false alarm in T seconds is [58]

$$P_{FA} = \frac{\beta T \sqrt{\rho}}{\sqrt{2\pi N_0 B}} \exp\left[-\frac{\rho^2}{2N_0 B}\right] \quad (11)$$

where β is the rms bandwidth of the low-pass-equivalent receiver noise process. The factor $\sqrt{\rho/(2\pi N_0 B)}$ is typically on the order of unity. The time-bandwidth product βT represents approximately the number of independent time samples produced by observing the matched-filter/envelope-detector output for T seconds. Thus P_{FA} can be related to P_{FA} as

$$P_{FA} \approx \beta T P_{FA} \quad (12)$$

The detection threshold ρ can then be selected to produce a specified P_{FA} as

$$\rho \approx \sqrt{-2N_0 B \ln\left(\frac{P_{FA}}{\beta T}\right)} \quad (13)$$

$N_0 B$ is obtained from the estimation procedure described in Section 4.4.4.

With matched-filter detection, the product βT is determined only by the number of spatial cells which are covered by a complete scan. For the maximum scan overlap ($15 \mu\text{rad}$), βT is $\sim 4 \times 10^4$ for a 1.25-mrad-diameter region, and thus the threshold ρ must be set so as to produce a single-sample false alarm probability P_{FA} which is much smaller than the desired overall probability P_{FA} .

In the LITE system, extremely low false alarm rates are not required. The main issue is whether the acquisition system can recover "gracefully" from false alarms, and the dither scan provides such a means of recovery. Failure to detect a target in the dither scan after an initial false hit merely results in additional time spent in performing the dither scan before eventual resumption of the main scan.

The analysis of the pick-maximum mode uses many of the same parameters as in threshold detection, and this discussion summarizes the main results. Although the receiver observes the matched-filter/envelope detector output in continuous time, an analogy is made to a discrete-time receiver to simplify the analysis. Assume that in T seconds, the receiver output process can be represented by approximately βT equally spaced, independent samples as in the threshold-detection analysis. The corresponding discrete-time receiver picks the largest magnitude time sample as the one with the beacon. The probability of a correct detection in the continuous-time case is then equated with the corresponding probability in the discrete-time receiver. The latter is a classical M -ary detection problem, where $M = \beta T$. Using the union bound, the probability P_E of choosing the wrong sample can be shown to be

$$P_E \approx \frac{\beta T - 1}{1 + \frac{N_{02}}{N_{01}}} \exp \left[- \frac{E}{N_{01} + N_{02}} \right] \quad (14)$$

where N_{01} and N_{02} are the receiver noise densities when signal plus noise and only noise are present respectively. This result assumes implicitly that only one time sample contains the signal whereas the assumed discretized version of the receiver may actually produce more than one such sample, depending upon details of the sampling. Nonetheless, the number of samples containing signal is on the order of unity, and the above expression may be used as a good approximation. As indicated previously, with matched-filter detection βT depends only on the number of spatial cells being searched.

At the conclusion of the scan, the HBO returns to the location where the largest detector output was obtained, and a dither scan with a threshold detector is begun, similar to the dither scan in the threshold-detection mode. There are differences in detail, however, between the pick-maximum and threshold-detection dither searches. In the latter, the detector threshold is computed on the basis of a preacquisition receiver noise measurement. In the former, the threshold-setting procedure is modified to the following: the threshold is simply set equal to one-half the value of the detector output obtained at the maximum-signal location during the acquisition scan. No knowledge of any other signal, noise, or system parameters is required. This choice of threshold can be justified on the basis that in a wide range of scenarios, the dither false alarm and missed-detection probabilities turn out to be comparable, i.e., $P_{FA} \approx 1 - P_D$. Both probabilities are then made to decrease simultaneously with increasing received-signal power. This approach differs from

that used in the threshold-detection mode in which the receiver operates as a constant false alarm receiver where P_{FA} remains fixed but P_D varies with signal power. Analysis of the dither performance can be found in the Appendix.

The preceding analysis for both threshold and pick-maximum detection assumes that the effects of LOS jitter on the actual detection probability are negligible. This is true only if the magnitude of the jitter is much smaller than one FOV of the detector. The main issue is whether gaps in the scanning pattern created by the jitter result in the target being missed entirely. There is also a secondary issue of determining a precise target location in the presence of jitter even if the target is detected. Location determination errors can occur because the apparent target position may be displaced from the true position or because the target image may even be smeared by the jitter. However, these secondary issues can be ignored here because the present system needs only to estimate the location with accuracy sufficient that the target can be relocated during the dither scan. Cross-axis jitter, i.e., jitter in the direction orthogonal to the direction of scanning, is of greater concern than jitter in the scanning direction. A complete statistical analysis of missed detections caused by LOS jitter is complicated. However, with overlap, a simple, conservative rule of thumb which follows from purely geometric considerations is that the target will always be within the detector FOV if the peak-to-peak magnitude of the cross-axis jitter does not exceed the amount of overlap. The interpretation of peak value depends upon the nature of the jitter. For a random process, the peak value might be identified with a 3σ value. For sinusoidal components, the peak corresponds to the peak of the sinusoid.

A more exact analysis of jitter effects must take into account the statistics and temporal behavior of the jitter. Only the main issues are highlighted here. If the scan is fast enough and the jitter amplitude small enough, any jitter-induced target motion may appear to be frozen over one or more scans in the neighborhood of the target. In the case of ACTS, the jitter spectrum is spread over a band between 0 and 300 Hz. The largest single disturbance is produced by the 100-Hz fundamental of the momentum wheel (see Tables 8 and 11). The spiral scan frequency, that is, the frequency associated with the period of one ring, varies with the scanning velocity and radial position in the spiral. The peak spiral frequency is 160 Hz occurring in the 160 mrad/s scan, and the minimum is less than 0.6 Hz during the 2.5 mrad/s spiral. Thus during portions of the 160 mrad/s scan, the low-frequency jitter (in the region of a few Hertz) can be considered to have negligible effect, whereas the momentum wheel disturbances cannot.

Jitter margin must be traded against either signal-power margin or acquisition time. Figures 32 and 33 illustrate the principles of this trade-off. In Figure 32 the amount of overlap has been set equal to the peak-to-peak jitter amplitude, or twice the peak value of jitter, following the rule of thumb just discussed, and the scan rate has been held fixed to maintain a constant signal power margin. A sharp increase in total search time is observed as the peak jitter approaches one-half the detector FOV (and the overlap approaches one FOV). In Figure 33, overlap is set by the same rule, but the scan rate is increased so as to maintain a constant total search time at the expense of signal margin. The margin drops rapidly as the peak jitter approaches one-half the detector FOV. In this example, the receiver is assumed to be background noise-limited, in which case signal margin drops 3 dB for each fourfold increase in scan rate.

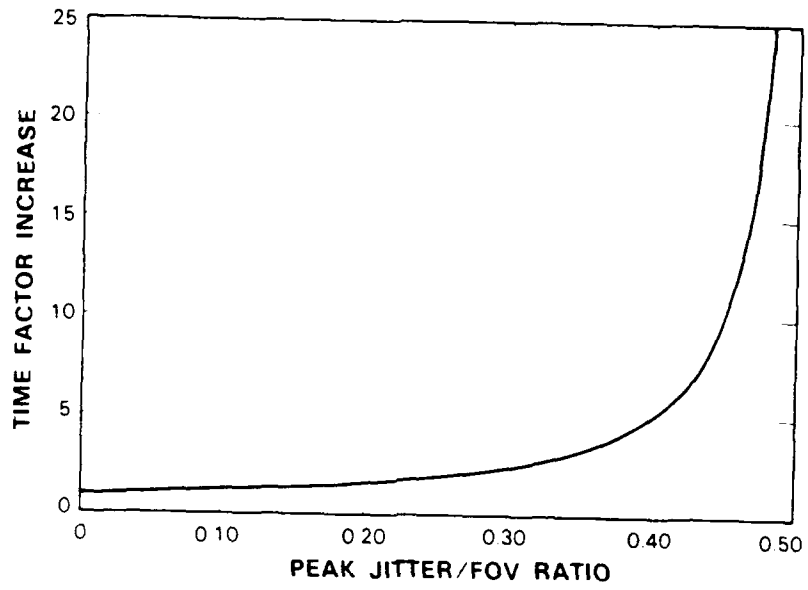


Figure 32 Acquisition time jitter trade-off

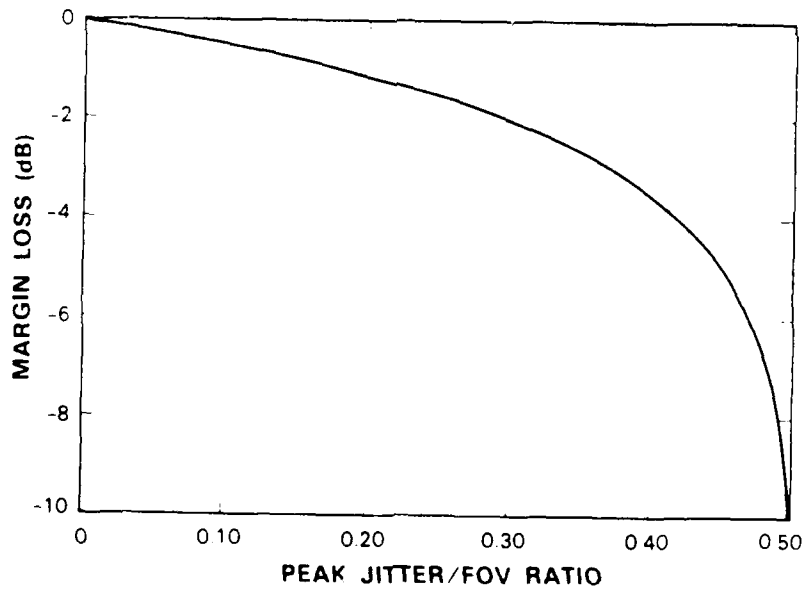


Figure 33 Acquisition margin jitter trade-off

121485.7

121485.8

Table 15 summarizes the performance of the LITE acquisition system in the threshold and pick-maximum detection modes. In the former case, margins have been calculated by fixing the false alarm probability $P_{FA} = 10^{-4}$ and determining the minimum received signal power required to maintain a detection probability $P_D = 0.999$ where the effects of jitter have been assumed to be made negligible by the use of overlap. The margin then represents the difference between this minimum signal power and the actual available power as given by the link budget in Table 14. Different choices for P_{FA} and P_D will yield somewhat different margins. Similarly, with pick-maximum detection, the error probability has been set to $P_E = 10^{-3}$ to obtain the indicated margins. The pick-maximum mode shows somewhat higher margins than threshold detection because with the latter, detection performance must be compromised to obtain a low false alarm rate. (The single-sample, false alarm probability must be set to $P_{FA} \approx 10^{-9}$ in order to obtain an overall performance of $P_{FA} = 10^{-4}$). The scan times are the times required to complete an entire scan of a single 1.25-mrad-diameter region. If the target is present in the interior of the scanned region, the actual times will be less in the threshold-detection mode, depending upon the actual location. In the event that the target is not present in the particular region, the times will be greater by an amount depending upon how many regions must be searched before the target is encountered. The performance against the nighttime and daytime earth backgrounds is based on the background numbers given earlier. An APD gain of 100 has been assumed throughout.

TABLE 15.			
Acquisition System Performance Summary			
Scan Rate ($\mu\text{rad/s}$)	10	40	160
Search Time (s)			
Overlap (μrad)			
5	8.8	2.2	0.55
10	13.1	3.3	0.82
15	26.2	6.5	1.6
Threshold Detection Margin (dB)			
Nighttime Earth	16.6	13.8	10.7
Daytime Earth	15.3	12.9	9.7
Pick-Maximum Margin (dB)			
Nighttime Earth	18.5	16.1	12.7
Daytime Earth	17.9	14.8	11.5

The difference of no more than about 1 dB between daytime and nighttime margins arises from the fact that the APD dark current and front-end electronics noises set a lower limit on the effective background levels. The worst-case daytime earth backgrounds only exceed this level by a relatively small amount. To increase the nighttime margins, improvements in APD technology in terms of lower dark current (or use of APD

cooling) or in low-noise front-end active devices are required. Also, it is noteworthy that each fourfold increase in acquisition time increases signal margin by about 3 dB, reflecting the fact that the total receiver noise process is essentially background noise-limited. In the signal shot-noise-limited regime, the corresponding increase in margin would be 6 dB.

4.5 HAND-OFF FROM ACQUISITION TO TRACKING

Following acquisition of the received beacon it is necessary to transfer control of the mirror position servos from the scan generator to the tracking system. The essential difference between the scan and tracking servos is in the source of the error signal (See Section 4.6.2). During the acquisition scan the error signal is formed from the difference between the commanded scan position and the actual mirror position, measured with respect to the mirror housing. During tracking, the error signal comes from the angle error detector, and the tracking error is a measure of how far from null the received beacon is on the ATD.

Successful acquisition merely ensures that the received beacon is visible somewhere within the FOV of the ATD. There is usually a residual tracking error which the tracking loop must null immediately following hand off. Furthermore, in order to keep the residual error within the pull-in limits of the tracking loop, the hand off must be completed within a time that is short compared to open-loop jitter and drift time constants.

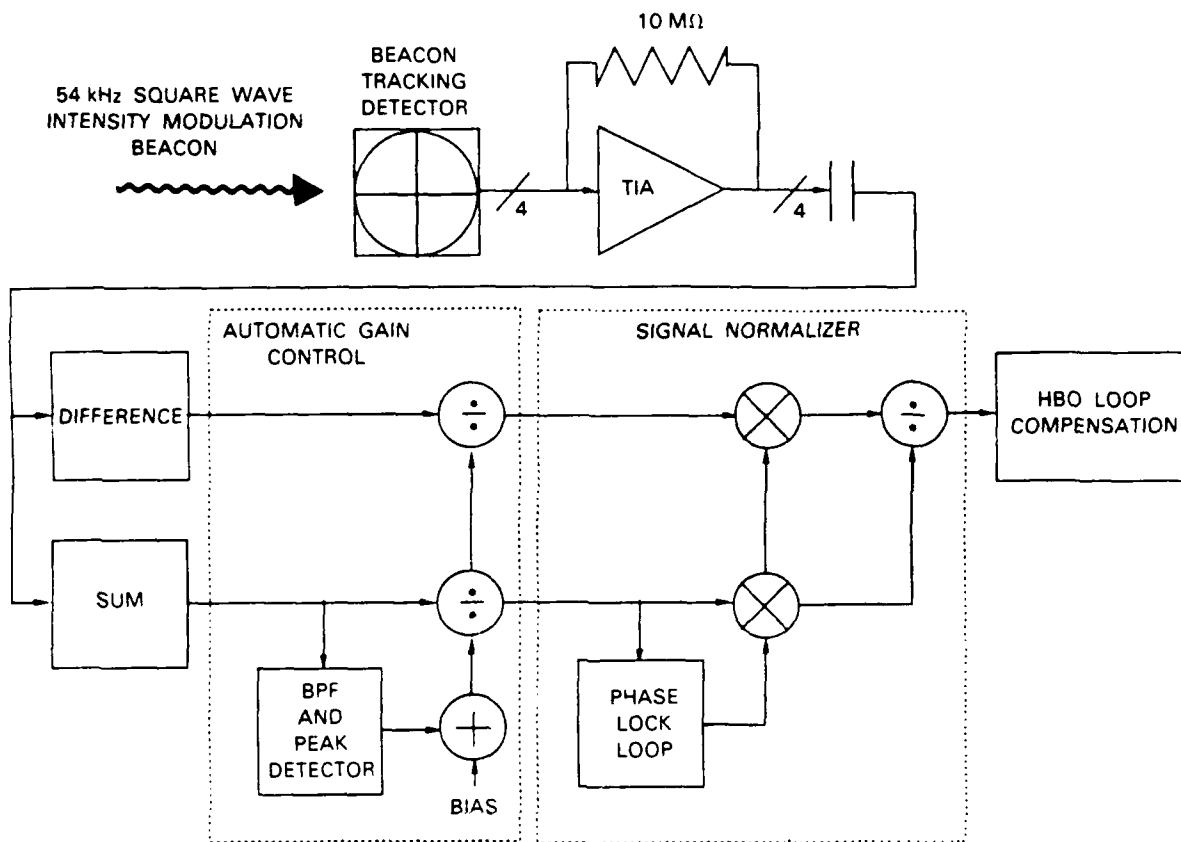
The hand-off sequence begins with the successful acquisition of the received beacon, defined by a hit detected during the dither scan. Next, the processor looks for an indication of a valid tracking error signal prior to transferring control of the mirror position servos from the acquisition scan generator to the tracking system. The valid tracking error signal is defined as a stable output from a quadrature detector of the sum channel phase-lock loop which is used to convert the IF error signals to baseband (Figure 34). As soon as these conditions are met the position servos are switched and the tracking system nulls the beacon position error present prior to hand-off.

Shortly after the switch to hand over has been initiated, the PLL quadrature signal is checked again, and an rms level detector on the normalized tracking errors is checked to determine if tracking has indeed been established. These detectors also serve as loss-of-lock indicators.

4.6 TRACKING AND POINTING

4.6.1 Overview

The goal of the tracking system is to keep the rms tracking jitter to less than 0.05 BW and the bias to less than 0.020 BW. This section describes how these budgets are met in the presence of the spacecraft and OMS disturbances as well as variations in the received signal power. We begin with a discussion of the servo loops and then discuss the front-end angle error processing electronics.



106808-26

Figure 34. Tracking system normalizing angle error detector.

The ability of the tracking loop to track the spacecraft and OMS disturbances is measured by the uncompensated tracking error. Figure 35 shows spectrally the relative amplitude of some of the platform and OMS disturbances in relation to the required tracking budget. (There are a number of additional disturbances not shown in this figure, i.e., LEO and cross-orbit requirements as well as thermal and mechanical drifts.) It is clear that even without the 17 dB of low-frequency disturbance margin, some of the disturbances are almost 80 dB (with margin included) larger than the tracking budget. Furthermore, they are spread out over a wide range of frequencies. Figure 36 shows the basic concept that is used to track these out as well as point the transmitted beam. The first line of defense against the spacecraft disturbances is the mechanical interface. It is preferable to prevent such disturbances from entering the environment of the OMS than to track them out. However, as shown in Sections 3.2 and 3.3, this is only effective at frequencies above 50 Hz. The

remaining disturbances must be tracked out using the optical error sensor (ATD) as a reference. In the limit of very good tracking, the received beam will be held fixed relative to the LOS of the ATD. If the transmit laser is now combined (in this stabilized space) with the appropriate point-ahead angle, via reciprocity it will illuminate the distant receiver.

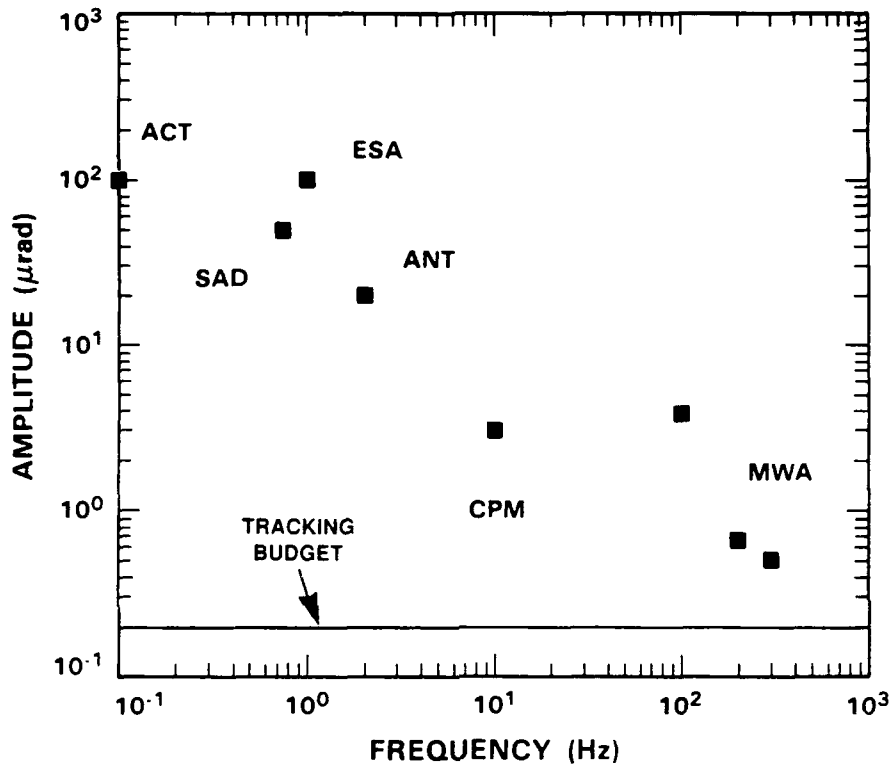
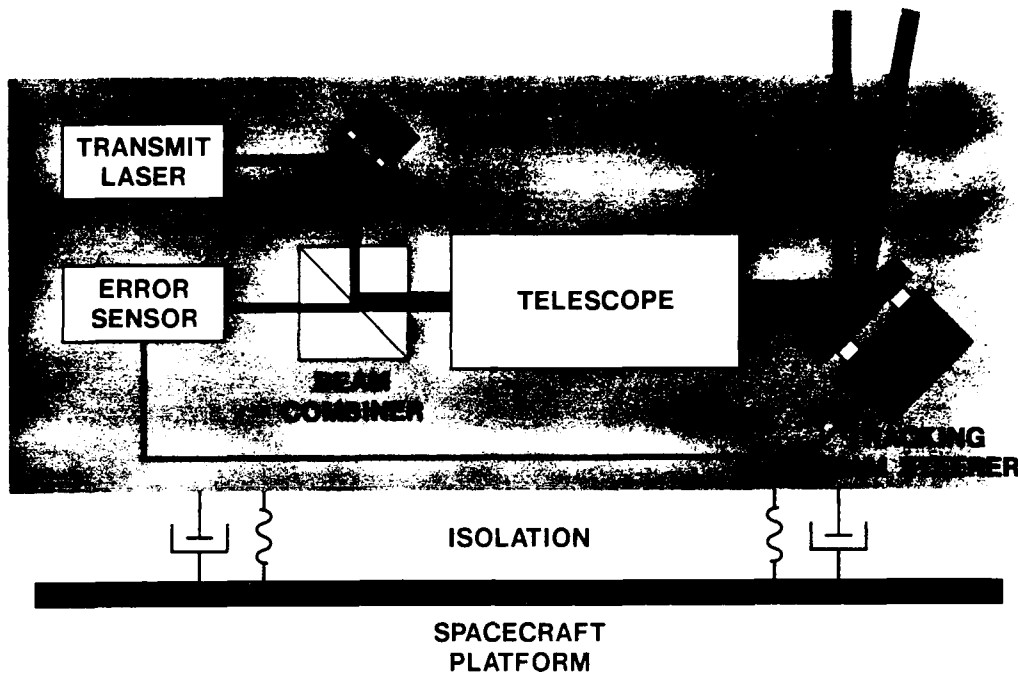


Figure 35. Tracking disturbance spectrum.

97055-7

In addition to the uncompensated tracking error is the noise-induced tracking error, which is defined in terms of the noise equivalent angle (NEA). Straightforward methods exist to derive the optimal loop transfer function based on the disturbances, signal power, and noise level. However, designing such optimal loops has limited application due to disturbance modeling uncertainties and a finite bandwidth capability in the HBO and CPM. Therefore the designs are confined to be type-2 tracking loops. Under this restriction we find that a 1-kHz crossover frequency in the HBO loop yields a good compromise between disturbance amplitude and signal power margins and does not stress the HBO's mechanical and electrical designs.



112049-1

Figure 36. Simplified tracking and pointing system.

4.6.2 Servo Description

Figures 37, 38, and 39 are block diagrams of the tracking system. This control loop is modeled in both the time and frequency domains to predict tracking performance. The models include saturation nonlinearities such as controller voltage and motor torque saturation. The Dahl model for bearing friction [59] and bearing torque noise used in analyzing the CPM loop are based on data measured from a breadboard. Ripple and cogging torque are included but are small compared to the bearing torque noise.

Figures 38 and 39 contain more detailed block diagrams of the HBO and CPM loops. Tables 16 and 17 contain the HBO and CPM parameters. A adjustable compensator allows the HBO loop to be configured with a crossover frequency of 500 Hz during acquisition and either a 500-Hz and 1-kHz crossover frequency during handover/tracking. However, the 1-kHz mode is the primary one and is assumed in all reported budgets.

During acquisition, the CPM is controlled by a 10-Hz position loop and a 60-Hz velocity loop. Velocity feed-forward is used to minimize the time required while slewing to a target. During closed loop tracking, the HBO loop is nested inside the CPM loop to keep the HBO within its operating range. The HBO position sensors are sampled at 250 Hz and used to provide a direct error signal to the 10-Hz CPM loop. The outer loop maintains the velocity feedback to keep its dynamics well behaved in the presence of bearing variabilities. These bandwidths are sufficient to keep the HBO to within 70- μ rad rms (in object space) of

its null. In addition to the servo models shown in Figures 37 to 39, structural modes derived from NASTRAN analysis are integrated, as well as sensor nonlinearities, to ensure adequate performance and stability. In all configurations loop gain-increase margins are more than 6 dB, gain-decrease margins are more than 10 dB, gain-increase margins at a structural peak are less than 10 dB, phase margins are more than 35°, and the torque margins are greater than 3.

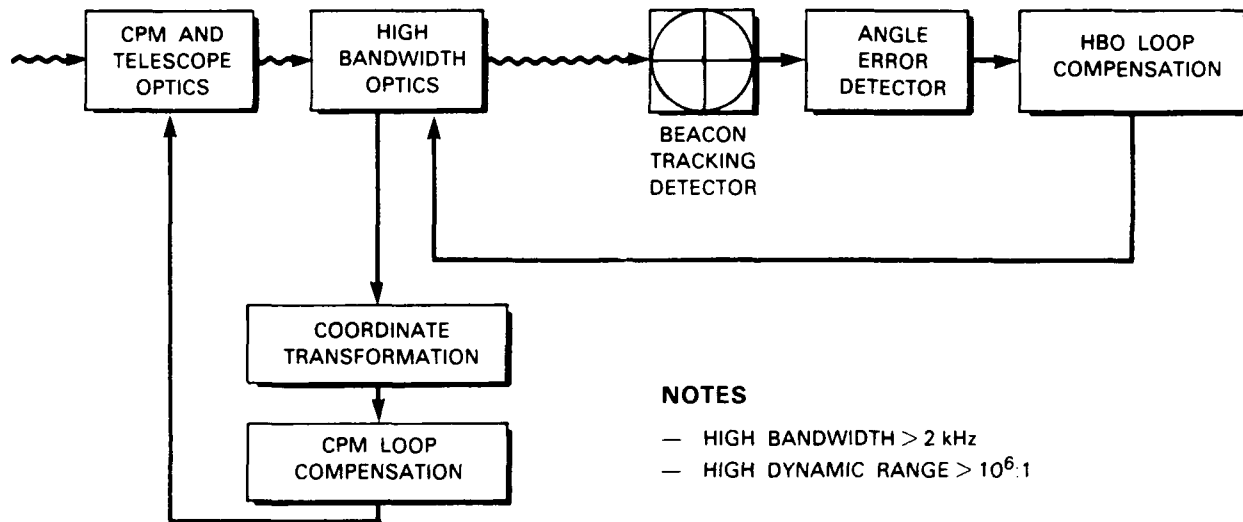


Figure 37. Tracking system block diagram.

106808-2

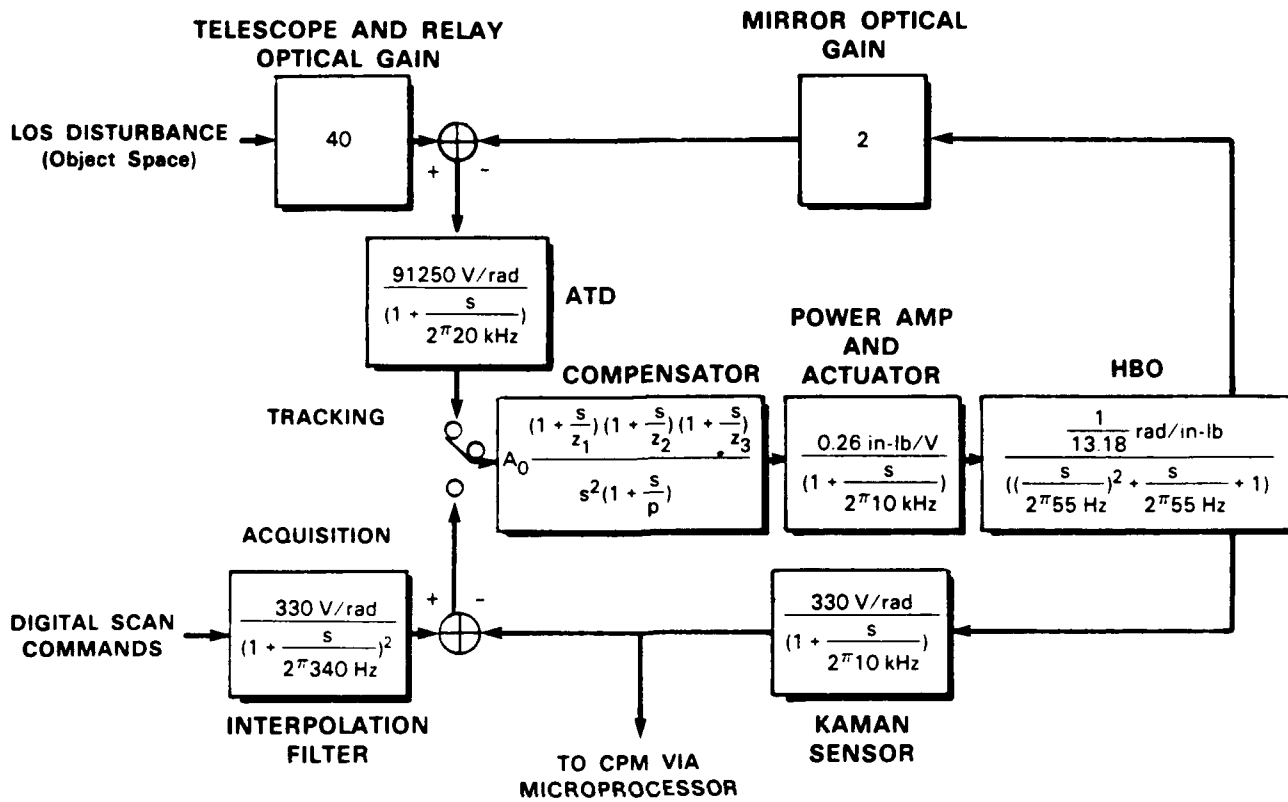


Figure 38. HBO loop block diagram.

121485-9

TABLE 16.
HBO Loop Parameters

	A_o	Z_1	Z_2	Z_3	P
Acquisition	7.3 k	2.6 Hz	132 Hz	132 Hz	10 kHz
Tracking					
500 Hz	74	2.6 Hz	132 Hz	132 Hz	10 kHz
1000 Hz	689	2.6 Hz	300 Hz	303 Hz	20 kHz

TABLE 17.
Azimuth CPM Loop Parameters

J	Moment of Inertia	0.649 in-lb-s ²
M	Mass	16.5 lb
L	CG Offset	< 0.05 in
K_M	Motor Constant	0.85 in-lb/A
T_{max}	Maximum Motor Torque	3.0 in-lb
γ	Dahl Friction Parameter	2.64×10^4 (in-lb) ⁻¹
T_{FO}	Friction Torque	0.78 in-lb
T_N	Noise Torque	0.04 in-lb (rms)
K_{CV}	Velocity Controller Gain	20.0 A/V
d	Velocity Controller Zero	15 Hz
K_{CP}	Position Controller Gain	365 V/V
a	Position Controller Zero	3 Hz
b	Position Controller Pole	30 Hz
K_V	Velocity Gain	1000 V/(rad/s)
g	Noise Torque Bandwidth	< 12 Hz (Worst Case)
K_1	Inductosyn Parameter	3.23
K_2	Inductosyn Parameter	68200
T_1	Inductosyn Zero Time Constant	4.46 ms
T_2	Inductosyn Pole Time Constant	0.2 ms
K_5	Equivalent Gain of DAC	3260 V/rad
h	Velocity Noise Bandwidth	200 Hz
T_O	HBO Signal Update Interval	4 ms

The overall tracking loop rejection is shown in Figure 40. The figure assumes worst-case end-of-life parameters (i.e., maximum radiation damage, worst-case MWA speed, worst-case CPM look angle). The symbols represent the rejection that each source of angular disturbances would require (without the required system margins) if it were allotted the whole tracking budget. The heavier line represents the overall rejection that would be required if all disturbance were to be tracked out simultaneously with no margin. This curve represents an approximate bound on the minimum required rejection. The finer line represents the rejection provided by the system design. Note that there is significant amplitude margin, particularly at low frequencies. Table 18 lists the individual and total uncompensated tracking errors (system margins included). The uncompensated tracking error for each axis is less than 0.15 μ rad and is met with more than the 17 dB of disturbance amplitude margin assumed for all disturbances except the MWA. The disturbance amplitude margin for the MWA is \sim 3 dB and is dominated by the mechanical resonance that couples with the third harmonic of the MWA (Figure 12). Note that this 3 dB of MWA amplitude margin is conservative for the reasons indicated at the end of Section 3.3. As noted earlier, the OMS-to-spacecraft mechanical interface was tuned to a resonance of 50 Hz. Below this resonance (where most of the disturbances are) there was no isolation of the disturbances from the LOS. Fortunately, the tracking system has a large amount of rejection margin in this region. However, at the MWA disturbance frequencies, where there is not a large rejection margin, there was a significant amount of mechanical isolation. In fact, without this high-frequency isolation the performance of the tracking, pointing, and acquisition system would be severely impacted.

TABLE 18.
Tracking System Uncompensated Closed-Loop Jitter (Per Axis)
(Including 7X Low-Frequency Amplitude Margins)

	North/South (μ rad)	East/West (μ rad)
Solar Array Drive (SAD)	0.0119	0.0119
Earth Sensor Assembly (ESA)	0.0034	0.0034
Antenna Assembly (ANT)	0.0044	0.0044
1 Hz	0.0029	0.0029
2 Hz	0.0033	0.0033
Momentum Wheel Assembly (MWA)	0.1435	0.0706
100 Hz	0.0053	0.0468
200 Hz	0.0631	0.0118
300 Hz	0.1287	0.0515
400 Hz	0.0033	0.0021
CPM Jitter	0.0280	0.0140
Bench Reaction To CPM and HBO Torques	0.0186	0.0186
rss Total	0.1479	0.0755

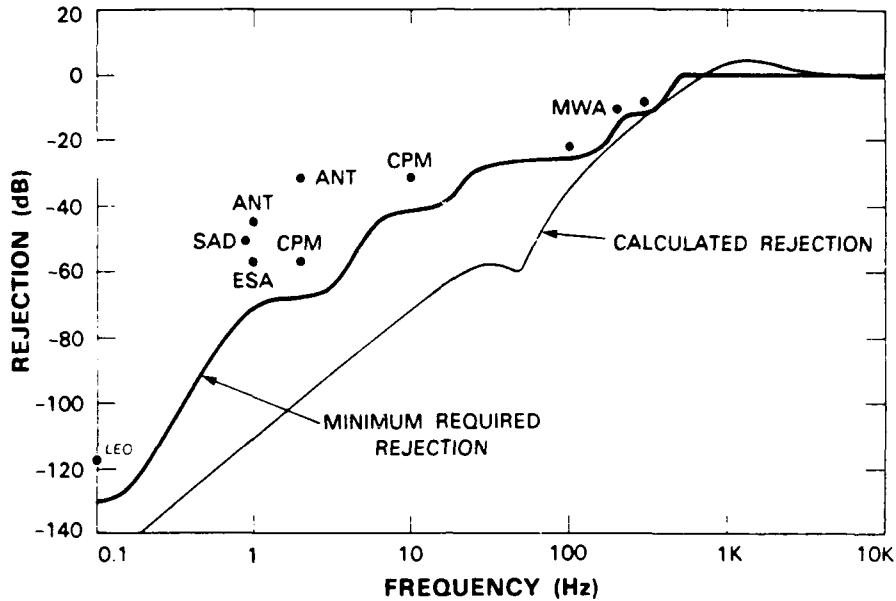


Figure 40. Tracking system closed-loop rejection performance.

4.6.3 Tracking Error Sensor

A block diagram of the tracking system normalizing angle error detector (NAED) is shown in Figure 35. As stated previously, an APD quadrant detector is used since it provides a performance improvement over alternative detectors when the system is not background- or signal shot-noise-limited [3]. The APDs are functionally equivalent to commercial units made by RCA (RCA C30902S), but are subject to extensive lot and unit testing to guarantee responsivity, radiation tolerance, and noise limits. Two modifications are required in packaging. First, a p^+ channel stop is diffused around the surface to enhance device radiation hardness [49,51]. Second, a much larger hermetically sealed can is used to house the APD than is used in commercial units. The flight units are filled with dry nitrogen, and leak-tested to insure that the density of nitrogen will not fall below that needed to inhibit arcing and corona at high bias voltages for the full four-year mission life. The dry nitrogen hermetic seal is necessary to prevent contaminants and water vapor from damaging the APD during ground testing and storage. The parameters for the APD are listed in Table 14.

The TIAs are designed to provide gain and phase uniformity at the beacon modulation frequency (54 kHz). A predominantly thermally noise-limited transimpedance of $10\text{ M}\Omega$ is achieved from dc to 70 kHz by using a T-network feedback and FET front ends for the TIAs. It is not necessary to cool either the detectors or the preamps to achieve this performance. The front-end noise is listed in Table 14.

The sum signal as well as the azimuth and elevation error signals are derived from the the preamp outputs by simple sum and difference networks. The sum channel signal is used for error normalization during tracking and for signal detection during acquisition.

In order to maintain a constant loop bandwidth in the presence of signal power variation, the estimated sum channel power is used to normalize the difference channels. Because of the large dynamic range expected in the received signal power (8×10^6 to 2.5×10^{11} photon/s incident on the APDs) the normalization is preceded by an AGC stage. The AGC is performed at IF, and uses the peak detected sum signal to control the IF amplitude of the sum and difference signals. The gain decreases quickly in response to a rise in sum channel power (attack time constant $< 35 \mu\text{s}$), but increases with a much longer time constant (decay time constant $> 1 \text{ ms}$) when the sum signal power decreases. The attack time is set by the bandwidth of the bandpass filter. The decay time is set by time constants in the detector. A dc bias is added to the detector output to limit the maximum AGC gain and ensure low noise performance. This AGC stage provides 40 dB of gain control. The fast AGC attack time allows the transients and imperfections in the AGC stages to settle before the 1-kHz tracking loop can respond to them. The slower decay time allows the normalizer to respond to most of the fades which would be encountered in an ACTS-ground link and therefore minimizes the effects of AGC gain pumping.

The second stage of gain control is performed at baseband, after the synchronous demodulator. The sum channel is low-pass filtered and used to normalize the azimuth and elevation difference signals. The time constant of the low-pass filter is chosen as $\sim 1 \text{ ms}$ to be commensurate with atmospheric fade coherence times. An additional 36 dB of gain control is provided by this stage. The resulting output error signals have ~ 80 dB of signal power dynamic range and a bandwidth in excess of 20 kHz.

The effect of signal and background shot-noise, as well as device noise, will be defined in terms of the NEA. The detector FOV is chosen as $20\text{-}\mu\text{rad}$ ($\sim 5\text{-BW}$) diam. as a compromise between providing a wide FOV for acquisition and minimizing background noise for tracking. For this detector size it has been shown that the NEA is approximately given by [3]

$$N_o = 2e \left\{ FG^2 \left[\eta e \left(0.84 \frac{P_s}{h\nu} + \lambda_b \right) + 4 I_{db} \right] + 4 I_{dk} \right\} + 4 N_c \quad (15)$$

$$NEA = \left[\frac{N_o NEB}{K_D^2 P} \right]^{1/2} \quad (16)$$

NEB = Single-sided noise equivalent bandwidth of tracking loop

K_D = Angle discriminator gain

The above parameters are described in Section 4.4.5. For a diffraction-limited optical system with a 5-BW ($20\text{-}\mu\text{rad}$) detector diameter, $K_D = 1.64 \text{ BW}^{-1}$ ($0.381 \mu\text{rad}^{-1}$). The factor of 0.84 accounts for the finite detector size and dead zone (see Figure 28).

The APD gain can be optimized to minimize the NEA. Assuming small k and large G , the optimum APD gain is given by

$$G_o = \left[\frac{8 \left(I_{ds} + \frac{N_c}{2e} \right)}{k \left(\eta e \left\{ 0.84 \frac{P_s}{h\nu} + \lambda_b \right\} + 4 I_{db} \right)} \right]^{1/3} \quad (17)$$

Figure 41 shows the gain-optimized NEA as a function of signal power incident onto the APD for a 1-Hz NEB. The actual NEB for the 1-kHz tracking loop is 3.2 kHz. Table 16 shows the parameters assumed in the analysis. The dotted line represents the NEA noise floor that may result from post-TIA circuit noise that is not included in the above expressions. Clearly, noise sources after the TIA do not contribute significantly to the overall tracking error (< 0.01 BW).

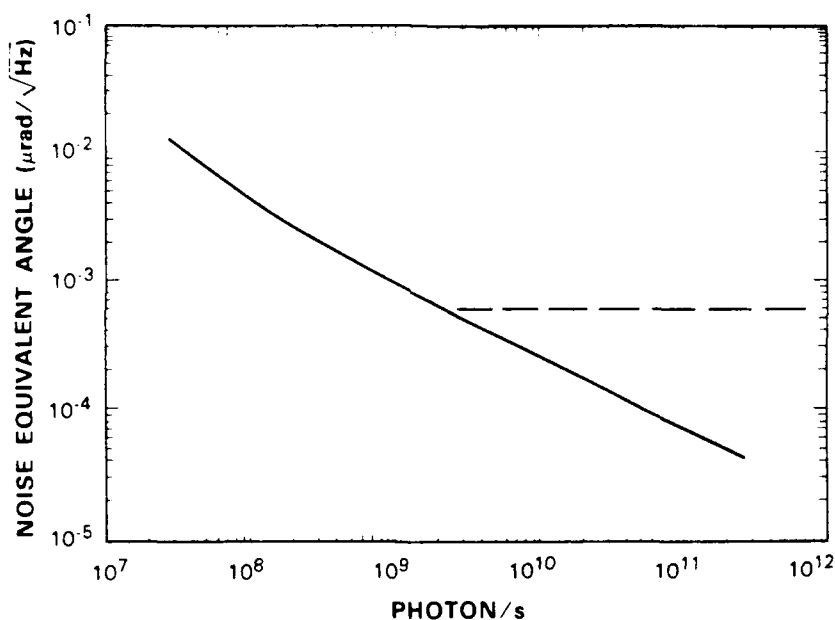


Figure 41. Tracking system NEA performance.

The combination of low noise performance and wide dynamic range allows the system to operate in the presence of large fades in received signal power. Figure 42 shows the static range over which the system can operate as a function of APD gain and received signal power. The fine tracking range is the approximate range over which the tracking system can maintain less than a $0.15\text{-}\mu\text{rad}$ NEA. The coarse tracking range is that over which the NEA is less than $0.680\text{ }\mu\text{rad}$. The AGC and NAED bandwidths allow the system to operate with instantaneous fades or power surges as large as 17 dB, provided the resulting signal power is not outside the indicated range envelope.

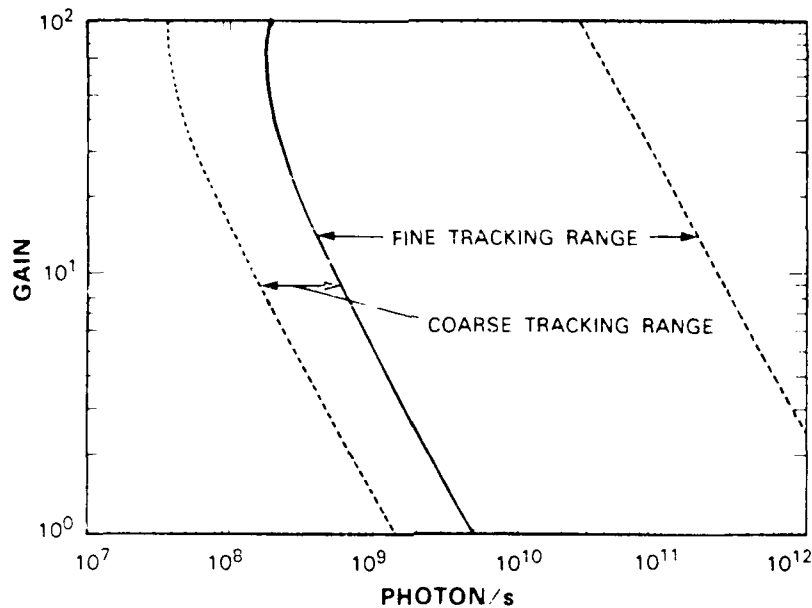


Figure 42. Tracking system operating ranges

Table 19 is a tracking system link budget. The NEA for each axis is less than $0.15 \mu\text{rad}$ and is met with more than 18 dB of signal power margin during communication, assuming a strong earth background.

It is important that the absolute angular offset in the tracking system be kept to a minimum to preserve discriminator linearity and dynamic range. Once the boresight procedure has calibrated this offset, it is important that the offset drift be kept to a minimum to maximize delivered transmit power. Both the offset and drift are dependent on relative and absolute linearity, gain stability, and phase stability of the various components that make up the tracking system. The three dominant components that contribute to drift are (1) APD gain instability, (2) APD nonlinearity and gain nonuniformity, and (3) NAED drift and nonlinearity. The APD gain stability is limited by stability of the bias voltage supplies ($\pm 0.2 \text{ V}$) and stability of the absolute and relative temperature of the four APDs ($\pm 0.2 \text{ C}$). The offset due to APD nonlinearity and gain nonuniformity is mainly a result of the differences in the linearity of the four APDs and causes the tracking system null to differ between the power used during boresight and the power received during tracking. In addition, any beam shear between the pupil imaged on the APD during boresight and tracking will contribute to tracking system bias. In the NAED, once the error signals are mixed down to baseband, dc offsets and drift become important error sources. After carefully analyzing all the contributions to offset and drift, the resulting offset was determined to be less than $0.2 \mu\text{rad}$ and the drift was less than $0.086 \mu\text{rad}$ over the fine tracking range indicated in Figure 42.

The total rms tracking jitter is less than $0.215 \mu\text{rad}$ in each axis. The system design is conservative and provides large disturbance amplitude, signal power, torque, gain, and phase margins, and large dynamic range.

TABLE 19.
Tracking System Link Budget

	Hand-Off	Communications
Transmit Laser (dBW)	-18.2	-18.2
Transmit Optical Losses	-4.6	-4.6
Laser Module Phase ($\lambda/20$)	-0.4	-0.4
Laser Module Amplitude (EOL)	-0.3	-0.3
Optical Train Phase Loss ($\lambda/15$)	-0.8	-0.8
Optical Train Amplitude Loss (EOL)	-1.7	-1.7
Obscuration (15% linear + spiders)	-1.3	-1.3
Polarization Error (15°)	-0.1	-0.1
Beam Spoiling (18 μrad)	-15.9	0.0
20 cm Transmit Aperture Gain (Ideal)	117.3	117.3
Spatial Pointing Loss	-1.9	-1.0
Space Loss (42700 km)	-295.9	-295.9
20 cm Receiver Aperture Gain (Ideal)	117.3	117.3
Receiver Optical Losses	-2.5	-2.5
Obscuration (15% linear + spiders)	-0.1	-0.1
Optical Amplitude Loss (EOL)	-1.8	-1.8
Polarization Error (15°)	-0.1	-0.1
Interference Filter (25 Å)	-0.5	-0.5
Detected Power (dBW)	-104.4	-88.6
Number of Photons/s at Detector (dB-Hz)	82.0	98.8
Power Required to Meet NEA Budget of 0.15 μrad per axis during comm and 0.580 μrad during hand over using 1 kHz crossover (dB-Hz)		
No Background	70.9	80.0
Earth Background	72.2	80.3
Solar Background	92.4	98.3
Margin (dB)		
No Background	13.1	18.8
Earth Background	9.8	18.5
Solar Background	-10.4	0.5
* 15 mW average power (30 mW peak power)		

4.6.4 Pointing Budget

Figures 43 and 44 show simplified diagrams of the overall pointing and tracking system. Most of the functions shown have been discussed. Table 20 contains a summary of the performance of the overall pointing system. Most of these entries were discussed earlier. In many cases the entries are the result of a complex thermal, mechanical, and electrical analysis (often involving extensive computer simulations). As a result, often the worst-case error is reported in the budget. Since it is unlikely that all these values will simultaneously be at their worst-case values, the actual performance of the pointing system should exceed that reported in the budget.

We will briefly discuss a few items in the pointing budget that have not been previously mentioned. The first entry contains errors that arise from limitations in the system optics. In particular, the entry for WFE is due to optical aberrations that cause asymmetrical far-field patterns (i.e., coma), and the entry for magnification uncertainty is due to the residual error in calibrating the magnification of the telescope and relay lenses as well as environmentally induced changes in magnification. The entry for spacecraft attitude error assumes that the worst-case spacecraft yaw axis uncertainty of 4.4 mrad is the axis in roll around the LOS and the maximum point-ahead angle is 32 μ rad. The entry for HBO cross-coupling is due to a rotation imposed on the point-ahead angle as a result of the HBO being off-axis. A nominal angle of incidence of 19°, a point-ahead angle of 32 μ rad, and an HBO offset of 130 μ rad are used in the calculation. And finally, the budgeted jitter and bias errors are included, although as pointed out in Section 4.6, we have considerable margin in achieving these numbers.

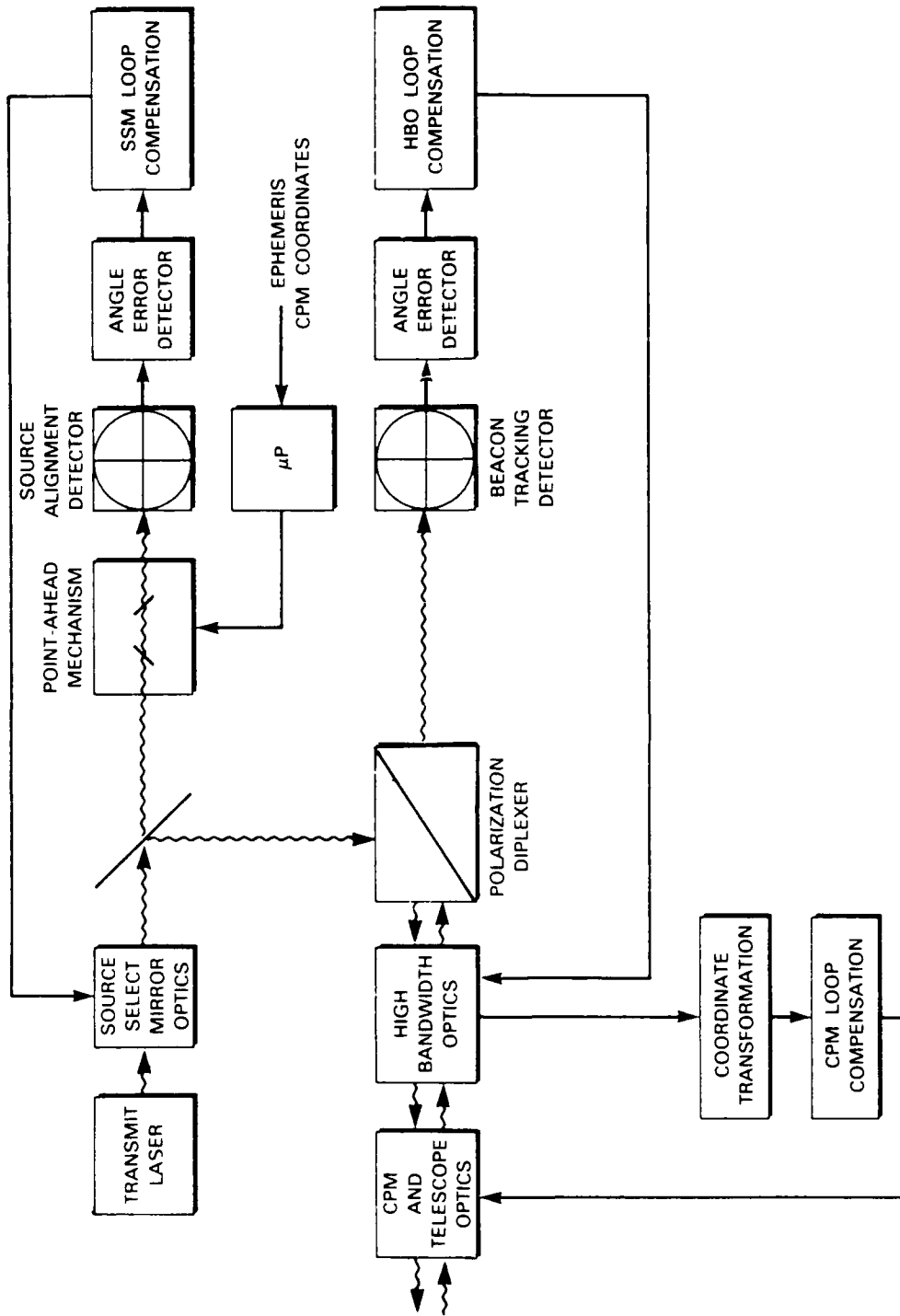


Figure 43. Pointing and tracking system block diagram.

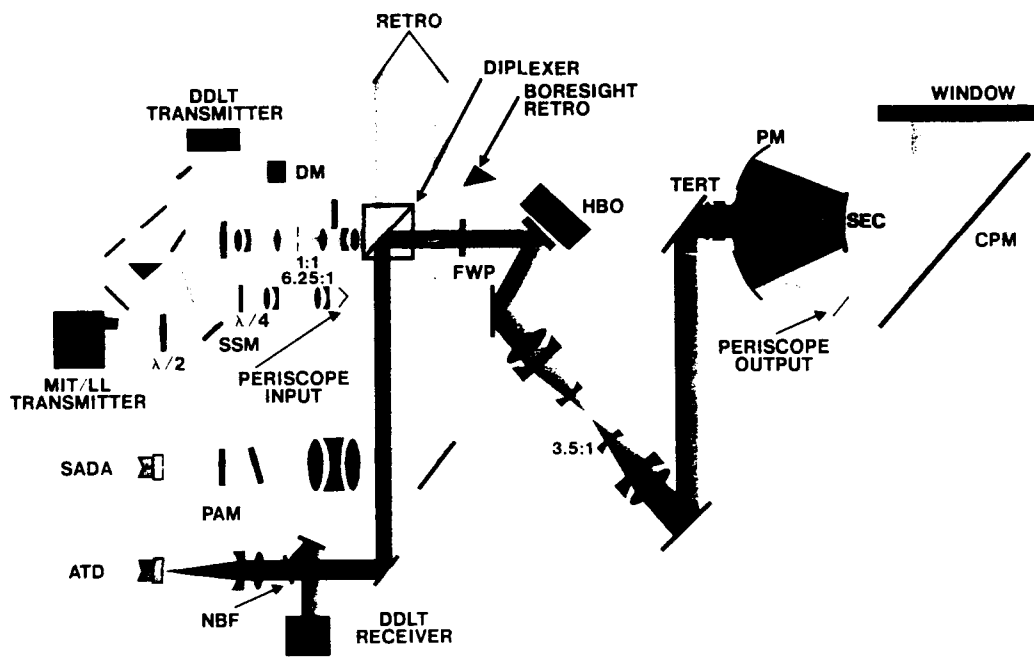


Figure 44. Pointing and tracking optical diagram.

106791-1

TABLE 20.
Pointing System Budget (Both Axes)

	Bias (μ rad)	Jitter (μ rad)
Optical Error	0.110	
Retro-Reflector	0.083	
Telescope Distortion	0.008	
Wavefront Error	0.064	
Magnification Uncertainty	0.032	
Point-Ahead Computation	0.157	
Tangential Velocity Prediction	0.067	
Spacecraft Attitude Error	0.141	
OMS to Spacecraft Attitude Error	0.005	
CPM Coordinate Transformation	0.010	
Point-Ahead Mechanism	0.052	
RDC Precision	0.016	
RDC Linearity and Drift	0.033	
RDC and Spacecraft Jitter	0.030	
Servo Drift	0.004	
Thermal/Structural Drift	0.013	
Orthogonality Between Plates	0.017	
Uncompensated PAM Nonlinearities	0.000	
Source Select Mechanism	0.025	0.057
Servo Drift	0.025	
SADA NEA		0.025
SSM Azimuth Stability		0.041
SSM Elevation Stability		0.031
High Bandwidth Optic	0.055	
Cross-Coupling	0.054	
Servo Offset and Drift	0.011	
U/L Tracking	0.122	0.304
Transmitter Housing		0.068
Uncompensated Azimuth Jitter		
Uncompensated Elevation Jitter		
Environment	0.020	0.040
SADA/ATD Path Thermal Drift	0.020	
Structural Jitter		0.040
Total (RSS)	0.241	0.319

5. CONCLUSION AND DISCUSSION

This report documents the requirements, design, and performance of the ACTS/LITE acquisition, tracking, and pointing system. For a summary review of system performance specifications, the reader is referred to Tables 3, 4, and 5.

Although parallels can be drawn to RF acquisition and tracking systems, the magnitude of the optical problem turns out to be much greater. Space platform angular vibrations measured in microradians or milliradian-level attitude control errors have virtually no impact on satellite RF systems where beamwidths are measured in degrees. In the optical domain, however, numbers of those magnitudes represent many beamwidths of angle uncertainty or jitter. As a result, the laser communications system designer is confronted with a spatial acquisition problem which can require a search over as many as hundreds of thousands of spatial cells. The spatial tracking system must be capable of rejecting disturbances many beamwidths in magnitude. These problems have both system and hardware implications which this work has attempted to address.

Satellite attitude control and on-board vibration stand out as key design drivers. A sound acquisition/tracking system design requires a careful, quantitative assessment of the spacecraft dynamic environment. In the case of ACTS, there were no on-orbit data available. Therefore, considerable effort was made by way of mechanical modeling, analysis, and measurement, with considerable interaction with the spacecraft contractor (RCA), to arrive at estimates of what the attitude control performance and the jitter environment were likely to be. In general, large amplitude disturbances, e.g., 100 μ rad from solar array motion, are found at low frequencies, while at higher frequencies the amplitudes are smaller, e.g., a few microradians from the momentum wheel at 100 to 400 Hz. Thus, disturbance rejection provided from the tracking loop across the frequency spectrum must be sized to reduce these disturbances to required levels. Obtaining adequate momentum wheel jitter rejection resulted in a loop bandwidth requirement of about 1 kHz, considerably in excess of the momentum wheel disturbance frequencies themselves. Realizable loop bandwidths in turn are dependent on HBO technology.

Because of inevitable uncertainties in estimating spacecraft angular disturbances, considerable conservatism must be incorporated into the analysis and the final system design. For example, in assessing spacecraft momentum wheel jitter, conservative assumptions were made about momentum wheel imbalance, transmissibility between the momentum wheel location and LITE optical module, the phasing of disturbances at given frequency, and momentum wheel speed. The tracker has been designed with large disturbance-rejection margins and avoids operation in regions where performance is sensitive to modeling errors. Thus the ACTS/LITE tracking system is designed to keep pointing and tracking errors (*bias and jitter*) to less than 0.1 BW. Similarly, the acquisition system incorporates a number of different operational modes - varying scan rates, overlaps, and the capability of accommodating worst-case as well as nominal uncertainty region sizes. By design, both the acquisition and tracking systems have large signal power margins — in excess of the data communications margins — for overall system robustness.

The LITE system was designed as a one-way link, and consequently a number of features that would be present in a duplex link are not present. For instance, the tracking system utilizes a low-bandwidth APD quadrant detector with an intensity-modulated beacon. Although it satisfies the LITE requirements, it is not

directly applicable to two-way direct-detection or heterodyne systems unless both a beacon and a communications beam are transmitted. For direct-detection links, quadrant APD receivers are still an attractive choice although the spectral broadening of the data-modulated signal creates a requirement of larger front-end bandwidth. Consequently the angle-error detector must be redesigned to operate at lower SNRs. In a heterodyne link, operation with a quadrant APD tracker separate from the communications front-end requires a splitting of power between the tracking and communications detectors. In addition, heterodyne systems will not generally employ intensity-modulated signals and thus the tracking system will be more sensitive to device and background noise with baseband detection of the received signal.

System improvements can be projected for the future. Acquisition times can be reduced with a parallel search scheme using a CCD or charge-injection device (CID). Work on CCD acquisition systems is currently ongoing, and it should be possible to implement such systems in the near future. A scanning search was expedient in the LITE system, but search times can become long when the uncertainty region becomes large or received signal powers are low. Although a direct-detection tracker is the logical choice for a direct-detection communications system, a heterodyne tracking system may be considered for heterodyne links. The heterodyne tracker potentially offers some of the same advantages as heterodyne communications, namely better sensitivity to signal and more immunity to background noise compared to direct-detection. However, a number of engineering issues remain to be worked out.

The LITE acquisition/tracking system applies to a geostationary satellite. Although the design of a corresponding package for a LEO platform would appear to be similar, some caveats are noted, particularly for spatial acquisition. In the case of LEO acquisition of a GEO satellite, the LEO telescope or CPM must perform highly accurate open-loop slewing, based on the satellite ephemerides, to freeze the motion of the GEO in its FOV. Peak slew rates can be 1.3 mrad/s, i.e., many diffraction-limited beamwidths per second, and as much as five times greater than the corresponding rates required on the GEO platform. Inaccurate slewing can create two problems: (1) the acquisition detector becomes faced with the problem of acquiring a streak instead of a spot, and (2) the return beacon, which in the present scheme is open-loop pointed at the intended target, will drift away from the GEO while the GEO is acquiring. In addition, attitude control errors on the LEO platform create angle coordinate uncertainty and hence additional slewing errors. For example, a yaw error of θ causes a rotational error of θ in roll-pitch coordinate orientation. Thus the actual slewing trajectory in roll and pitch will deviate from the intended one by the angle θ and the pointing will drift away from the target at an angular rate of (slew rate) \times θ . If the slew rate is 1 mrad/s and the attitude error is $\theta = 1$ mrad, then the drift error rate is 1 μ rad/s. These potential difficulties can be mitigated by rapid acquisition and handover to tracking on both ends of the link so that any drift errors are not allowed to grow large enough to become a problem. Furthermore, the need for accurate attitude control is indicated.

In future laser communications system design, choice of aperture size, at least in part, will be influenced by the ability to point and track accurately. Large apertures will have more stringent requirements than small ones. (Although direct-detection receivers can employ wide-FOV detectors which make performance insensitive to pointing and tracking errors, the transmit beam, if diffraction-limited, must still be pointed with fractional-beamwidth accuracy. Heterodyne receivers typically operate with a diffraction-limited FOV and consequently will have requirements comparable to those for the transmit beam.) The experience with ACTS

indicates that attempting to point an aperture very much larger than the 20-cm LITE aperture may be stressing to the pointing/tracking system design. The ability to utilize larger apertures may require (1) a more quiet satellite host platform, (2) more effective mechanical isolation between the optical module and the satellite body, or (3) improved tracking/pointing system design and component technology. However, since a laser communications system is likely to be only a secondary payload on a satellite, it is more reasonable to expect the optical payload to adapt to its host environment via alternatives (2) and (3) rather than vice versa by (1).

The issue of the effects of radiation from the natural environment, especially on optical detectors (e.g., APDs and CCDs), is not completely resolved and requires further investigation. The two effects of concern are bulk damage and radiation-induced photocurrent, both of which can be detrimental to detection and tracking performance.

The issue of propagation through the atmosphere was briefly described and requires much more in-depth analysis if a space-to-ground link is to be implemented. However, our main interest is in space-to-space links and therefore the work reported here has focused primarily on that application. In operational systems a space-to-ground link is probably best realized by conventional RF techniques which are not subject to the same degree of atmospherically induced degradation as optical systems.

What has been described in this report is a point design specific to the ACTS/LITE system. The details may not necessarily be duplicated exactly in future satellite laser packages and no claim of optimality is made for the present design. However, acquisition and tracking design has been carried beyond the laboratory-demo stage to a live spacecraft environment. This work has identified areas that will require careful attention or design effort in future systems.

ACKNOWLEDGMENTS

The work described here is the result of a cooperation between many individuals. The ACTS/LITE acquisition and tracking system design was a joint effort between MIT Lincoln Laboratory and Perkin-Elmer Corporation, Government Systems Sector, Danbury, Connecticut. The OMS design was performed by Perkin-Elmer under Contract No. BX-1806.

Within Lincoln Laboratory, the authors wish to acknowledge the valuable contributions of Stephen Alexander, Elaine Arnau, Jonathan Bernays, Roy Bondurant, Don Boroson, Ed Bucher, Vincent Chan, John Drover, Frank Folino, Eui In Lee, Gregory Loney, Appa Madiwale, Paul Martin, Alan Pillsbury, Fred Walther, and Kim Winick in support of this effort.

REFERENCES

- [1] V.W.S. Chan. "Space Coherent Optical Communication Systems-An Introduction." *IEEE J. Lightwave Technol.*, Vol. LT-5, No. 4, 633-637 (1987).
- [2] J.E. Kaufmann and L.L. Jeromin. "Optical Heterodyne Intersatellite Links Using Semiconductor Lasers." *IEEE Global Telecommunications Conference Record*, Atlanta, GA, 26-29 November. 961-968 (1984).
- [3] E.A. Swanson and J. K. Roberge. "Design Considerations and Experimental Results for Direct Detection Spatial Tracking Systems." *Opt. Eng.*, Vol. 18, No. 6, 659-666, June (1989).
- [4] E.A. Swanson and V. W. S. Chan. "Heterodyne Spatial Tracking System for Optical Space Communication." *IEEE Trans. Commun.*, COM-34, 118-126 (1986).
- [5] M. Katzman, ed., *Laser Satellite Communications*, Prentice-Hall, Englewood Cliffs, NJ, (1987).
- [6] R.M. Gagliardi, *Satellite Communication*, Wadsworth, Inc., Belmont, CA, Chapter 9 (1984).
- [7] R.M. Gagliardi and S. Karp, *Optical Communication*, John Wiley & Sons, NY, Chapter 11 (1976).
- [8] J.H McElroy, et al., "CO₂ Laser Communication Systems for Near-Earth Space Applications." *Proc. IEEE*, Vol. 65, No. 2, 221-251 (1977).
- [9] K. J. Held and J.D. Barry. "Precision Pointing and Tracking Between Satellite-Borne Optical Systems." *Opt. Eng.*, Vol. 27, No. 4, 325-333 (1988).
- [10] K. J. Held and J. D. Barry. "Precision Optical Pointing and Tracking from Spacecraft with Vibrational Noise." in *Optical Technologies for Communication Satellites*, K. Bhasia ed., Proc. SPIE 616, 160-173 (1986).
- [11] L. M. Germann, R. Nelson, and P. W. Young, "Pointing, Acquisition, and Tracking Subsystem for Space-Based Laser Communications." in *Optical Technologies for Communication Satellites*, K. Bhasia, ed., Proc. SPIE 616, 118-128 (1986).
- [12] R. Kern, U. Kurel, and E. Hettlage, "Control of a Pointing, Acquisition, and Tracking Subsystem for Intersatellite Laser Links ISL." in *Optical Systems for Space Applications*, H. Lutz and G. Otrio, eds., Proc. SPIE 810, 202-210 (1987).
- [13] R. A. Laskin and S.W. Sirlin. "Future Payload Isolation and Pointing System Technology." *J. Guid., Contr. and Dynamics*, Vol. 9, No. 4, 469-477 (1986).
- [14] "Comparison of Direct and Heterodyne Detection Optical Intersatellite Communication Links." EOSL, No. 87-002, C. C. Chen and C. S. Gardner, Electro-Optic Systems Laboratory, Department of Electrical and Computer Engineering, University of Illinois at Urbana-Champaign, March 1987.
- [15] P. Van Hove and V.W.S. Chan. "Spatial Acquisition Algorithms and Systems for Intersatellite Optical Communication Links." MIT Lincoln Laboratory Technical Report 667, 27 November 1984 DTIC AD-A150794.

- [16] J. D. Barry and G. S. Mecherle. "Beam Pointing Error as a Significant Design Parameter for Satellite-Borne Free-Space Optical Communication Systems," *Opt. Eng.*, Vol. 24, No. 6, 1049-1056 (1985).
- [17] G. A. Koepf, R. Peters, and R. G. Marshalek. "Analysis of Burst Error Occurrence on Optical Intersatellite Links (ISL) Design," *Proc. SPIE*, 616, 129-136 (1986).
- [18] C. C. Chen and C. S. Gardner. "Impact of Random Pointing and Tracking Errors on the Design of Coherent and Incoherent Intersatellite Communication Links," *IEEE Trans. Commun.*, Vol. 37, No. 3, 252-260 (1989).
- [19] K. Araki, et al. "Interaction Characteristics of Two Coupled Tracking/Pointing Subsystems in Optical Intersatellite Communications," CLEO '88, Anaheim CA, April 1988.
- [20] Private communication, E. A. Swanson and J. M. Elder, June 3, 1985.
- [21] L.L. Jeromin and V. W. S. Chan. "M-ary FSK Performance for Coherent Optical Communication Systems Using Semiconductor Lasers," *IEEE Trans. Commun.*, Vol. COM-34, No. 4, 375-381 (1986).
- [22] Katzman, *Laser Satellite Communications*, see Reference 5 in Chapter 6.
- [23] K. Winick. "Cramer-Rao Lower Bound on the Performance of Charge-Coupled Device Optical Position Estimator," *J. Opt. Soc. Am.*, Vol. 3, No.11, 1809-1895 (1986).
- [24] Private communication, November 1987.
- [25] T.J. McKnight, "The Lasercom Communication Package (LASERCOM) for Advanced Communications Technology Satellite (ACTS): A Design and Integration Study," NASA/ACTS-EXP-022, RCA Aerospace and Defense, Astro-Electronics Division, Princeton, NJ, 10 April 1985.
- [26] G.E. Schmidt, Jr., "Attitude Control Subsystem Pointing Analysis Update for ESA Sensing Reference," NASA/ACTS-AC-046, RCA Aerospace and Defense, Astro-Electronics Division, Princeton, NJ, 9 October 1986.
- [27] "ACTS Attitude Control Subsystem Technical Review", RCA Astro-Electronics Presentation at NASA/LeRC, 24 October 1986.
- [28] G.E. Schmidt, Jr., "MCP Receive Antenna Pitch and Roll Pointing Accuracy with Autotrack Attitude Sensing Reference," NASA/ACTS-AC-059, RCA Aerospace and Defense, Astro-Electronics Division, Princeton, NJ, 18 December 1986.
- [29] N.E. Goodzeit, "ACTS Gyro Pitch Control System," NASA/ACTS-AC-056, RCA Aerospace and Defense, Astro-Electronics Division, Princeton, NJ, 13 November 1986.
- [30] L.J. Pfeiffer, "LASERCOM to ACTS Simulator Space Craft Modal Tests / LASERCOM - RCA Special Model Test data," NASA/ACTS-FSC-025, RCA Aerospace and Defense, Astro-Electronics Division, Princeton, NJ, 27 November 1985.
- [31] L.J. Pfeiffer, "MWA and SAD Vibration Data", RCA 85-0074, RCA Aerospace and Defense, Astro-Electronics Division, Princeton, NJ, 10 December 1985.

- [32] C. Voorhees. "Test Report Measurements of MWA Induced Vibration for ACTS LASERCOM," NASA/ACTS-SE-042 Rev A. RCA Aerospace and Defense, Astro-Electronics Division, Princeton, NJ, 14 March 1986.
- [33] A. Sheffler. "MWA Induced Vibration of LASERCOM Optics," NASA/ACTS-LCS-005. RCA Aerospace and Defense, Astro-Electronics Division, Princeton, NJ, 9 April 1986.
- [34] Private communication, P.F. Martin, 8 January 1987.
- [35] Private communication, P.F. Martin, 27 November 1987.
- [36] Private communication, P.F. Martin, 26 May 1988.
- [37] Private communication, P.F. Martin, 6 October 1987.
- [38] K. Young, A. Liu, C. Chao. "Autonomous Navigation for Satellites Using LASERCOM Systems." AIAA 21st Aerospace Sciences Meeting, Reno, Nevada, 10-13 January 1983.
- [39] K. A. Winick. "Atmospheric Turbulence-Induced Signal Fades on Optical Heterodyne Communication Links." *Appl. Opt.* Vol. 25, No. 11, 1817-1825 (1986).
- [40] J. W. Strohbehn, ed., *Laser Beam Propagation in the Atmosphere*, Springer-Verlag, Berlin, Introduction (1978).
- [41] F. X. Kneizys, et al., "Atmospheric Transmittance/Radiance: Computer Code LOWTRAN 5," AFGL Report AFGL-TR-80-0067 (Air Force Geophysics Laboratory, Lexington, MA, 1980). AD No. A088215.
- [42] See References in Winick, *Appl. Opt.*
- [43] Private communication, K.A. Winick, 4 May 1988.
- [44] H. J. Boving and H. E. Hintermann. "Properties and Performance of Chemical-Vapor-Deposited TiC-Coated Ball-Bearing Components." 14th International Conference on Metallurgical Coatings, 23-27 March, San Diego, CA, 253-266 (1987).
- [45] F. R. Morrison, et al., "Load-Life Relationship for M50 Steel Bearings with Silicon Nitride Ceramic Balls," *Lubr Eng.*, Vol. 40, No. 3, 153-159 (1984).
- [46] K. T. Stevens. "The Torque Behavior of Grease-Lubricated Angular Contact Bearings Operating at Low Speeds," ESA (ESTL) 46, (1981).
- [47] V. Jayaraman, et al., "Design and Performance of an On-Satellite Laser Diagnostic System for a Free Space Optical Heterodyne Frequency-Shift-Keyed Communication System," in *High Data Rate and Atmospheric and Space Communications*, R. Hauptman, ed., Proc. SPIE 996, 84-91 (1988).
- [48] W. J. Smith, *Modern Optical Engineering*, McGraw-Hill, NY, Chapter 4 (1966).
- [49] P.P. Webb, R.J. McIntyre, and J. Conradi. "Properties of Avalanche Photodiodes," *RCA Rev.*, Vol. 35, 234-278 (1974).

- [50] Private communication. E.A. Swanson, 24 March 1986.
- [51] E. A. Swanson, E. R. Arnaud, and F. G. Walther, "Measurements of Natural Radiation Effects in a Low Noise Avalanche Photodiode," *IEEE Trans. Nucl. Sci.*, NS-34, No. 6, 1658-1663 (1987).
- [52] Private communication. P.F. Martin, 6 October 1987.
- [53] H. N. Russel, R. S. Dugan, and J. Q. Stewart. *Astronomy*, Vol II. Ginn, NY (1945).
- [54] W. L. Wolfe and G. J. Zissis, *The Infrared Handbook*, Environmental Research Institute of Michigan, Office of Naval Research, Department of the Navy (1978).
- [55] W.K. Pratt, *Laser Communication Systems*. Wiley, NY (1969).
- [56] J. Conradi, "The Distribution of Gains in Uniformly Multiplying Avalanche Photodiodes: Experimental," *IEEE Trans. Electron. Devices*, Vol. 19, No. 6, June, 1972.
- [57] D.K. Barton, ed., *Radar System Analysis*, Artech, Englewood Cliffs, NJ (1979).
- [58] C.W. Helstrom, *Statistical Theory of Signal Detection*, Pergamon Press, Oxford, England (1968).
- [59] B. G. King and L. B. Martin, "Simulation of DC Torque Motor Hysteresis and Cogging Effects," *Proc Annual Symposium Incremental Motion Control Systems and Devices 6th*, University of Illinois, 24-27 May 1977, 61-71.

APPENDIX

A.1 DITHER SCAN PERFORMANCE IN PICK-MAXIMUM ACQUISITION MODE

After completion of a pick-maximum acquisition scan, the HBO is returned to the maximum-signal location for a dither search. Let X_s be the maximum-signal value obtained at this location during the acquisition scan. For a dither scan, suppose the threshold value is set equal to aX_s where $a \leq 1$. Here we calculate the false alarm and missed-detection performance for the dither search as a function of a .

Let $\sigma_n^2 = N_{02}B$ be the variance of the input noise where N_{02} is the receiver front-end noise density when only noise is present and B is the detection filter bandwidth. If $P_{FA|X_s}$ denotes the single-sample false alarm probability conditioned on X_s , then the unconditional false alarm probability P_{FA} (single sample) with a linear envelope detector is given by

$$P_{FA} = \int_0^{\infty} P_{FA|X_s} p_{X_s}(X) dX \quad (A-1)$$

where

$$P_{FA|X_s} = \exp \left[-\frac{(aX_s)^2}{2\sigma_n^2} \right] \quad (A-2)$$

and

$$p_{X_s}(X) = \left(\frac{X}{\sigma_s^2} \right) \exp \left[-\frac{(X^2 + P)}{2\sigma_s^2} \right] I_0 \left(\sqrt{P} \frac{X}{\sigma_s^2} \right) \quad (A-3)$$

$\sigma_s^2 = N_{01}B$ is the receiver input noise variance in the detection filter bandwidth B with a front-end noise density N_{01} when signal plus noise are present. The above integral (A-1) can be evaluated exactly with the result

$$P_{FA} = \frac{1}{1 + a^2 \frac{N_{01}}{N_{02}}} \exp \left[-\frac{a^2 E}{2(N_{02} + a^2 N_{01})} \right] \quad (A-4)$$

where $E = 2P/B$ is the peak detected signal energy with a square-envelope pulse and matched-filter detection.

The probability of missed detection is more difficult to calculate exactly. Therefore, some simplifying approximations must be invoked. Let X_d be the envelope detector output during the dither scan when the signal is present. The Rician probability densities for both X_s and X_d can be well approximated as Gaussian under large signal-to-noise conditions, both with mean \sqrt{P} and variance σ_s^2 . The miss probability $P_M = 1 - P_D$ is then given by

$$P_M = \Pr (X_d - a X_s < 0 \mid \text{signal present}) \quad (\text{A-5})$$

The random variable $X_d - aX_s$ is also Gaussian with mean $(1-a)\sqrt{P}$ and variance $(1+a^2)\sigma_s^2$. Thus P_M can then be reduced to

$$P_M = \text{erfc} \left[(1-a) \sqrt{\frac{E}{(1+a^2)N_{01}}} \right] \quad (\text{A-6})$$

where $\text{erfc}[\cdot]$ denotes the complementary Gaussian error function, which itself can be further approximated, if desired, by any of several well known expressions.

These results for P_{FA} and P_M are plotted as a function of the factor a in Figures A-1 and A-2 for nighttime and daytime earth background scenarios, respectively, and assuming previously described values for the system noise parameters. Four sets of curves corresponding to 2×10^6 , 4×10^6 , 8×10^6 , and 1.6×10^7 detected photons/s are shown, representing the lower end of the range of signal powers of interest. Against the daytime earth background, it is observed that for $a \approx 0.5$, P_M and P_{FA} are roughly equivalent over this range of signal power. With a nighttime background, a similar conclusion holds for $a \approx 0.4$.

The value of $a = 0.5$ is chosen for all operational scenarios to simplify the system implementation. In the nighttime scenario, the difference in performance between $a = 0.4$ and 0.5 is small enough to justify using $a = 0.5$ here as well as for daytime backgrounds.

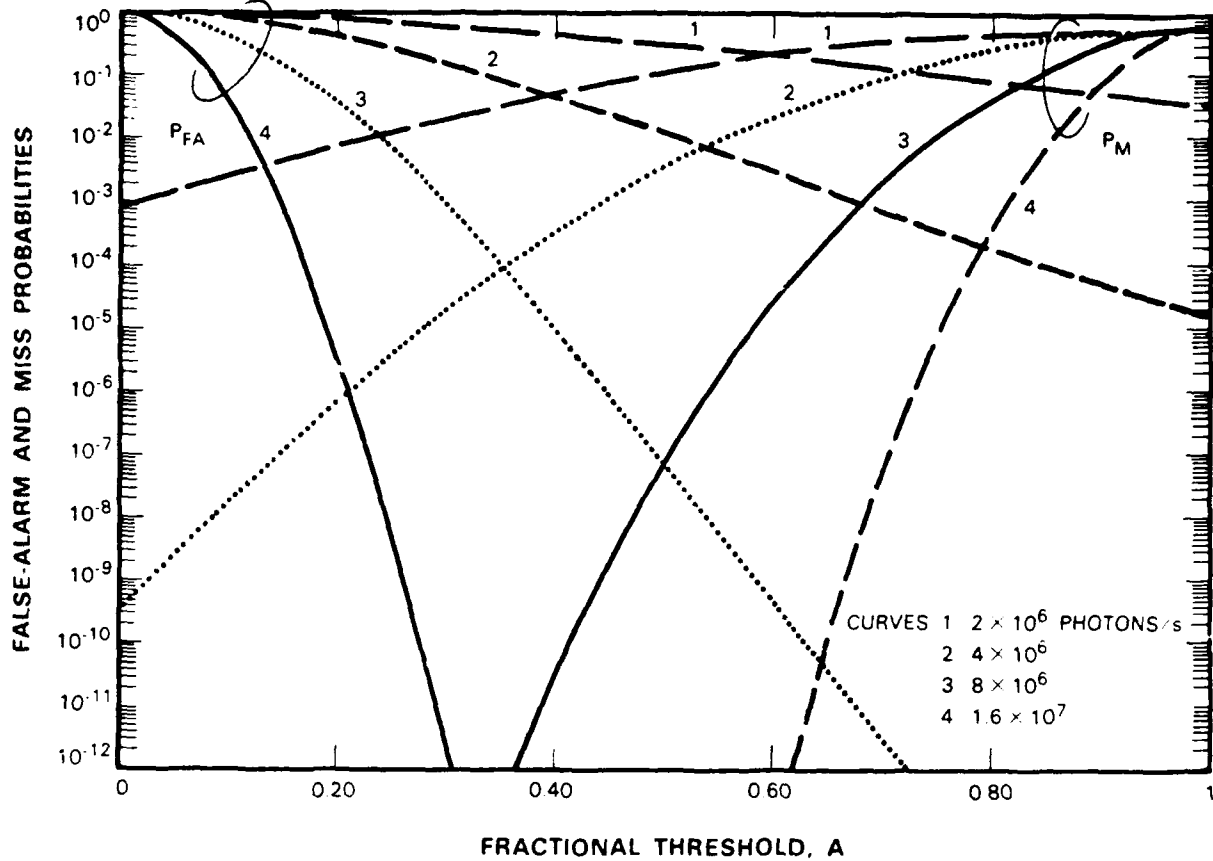


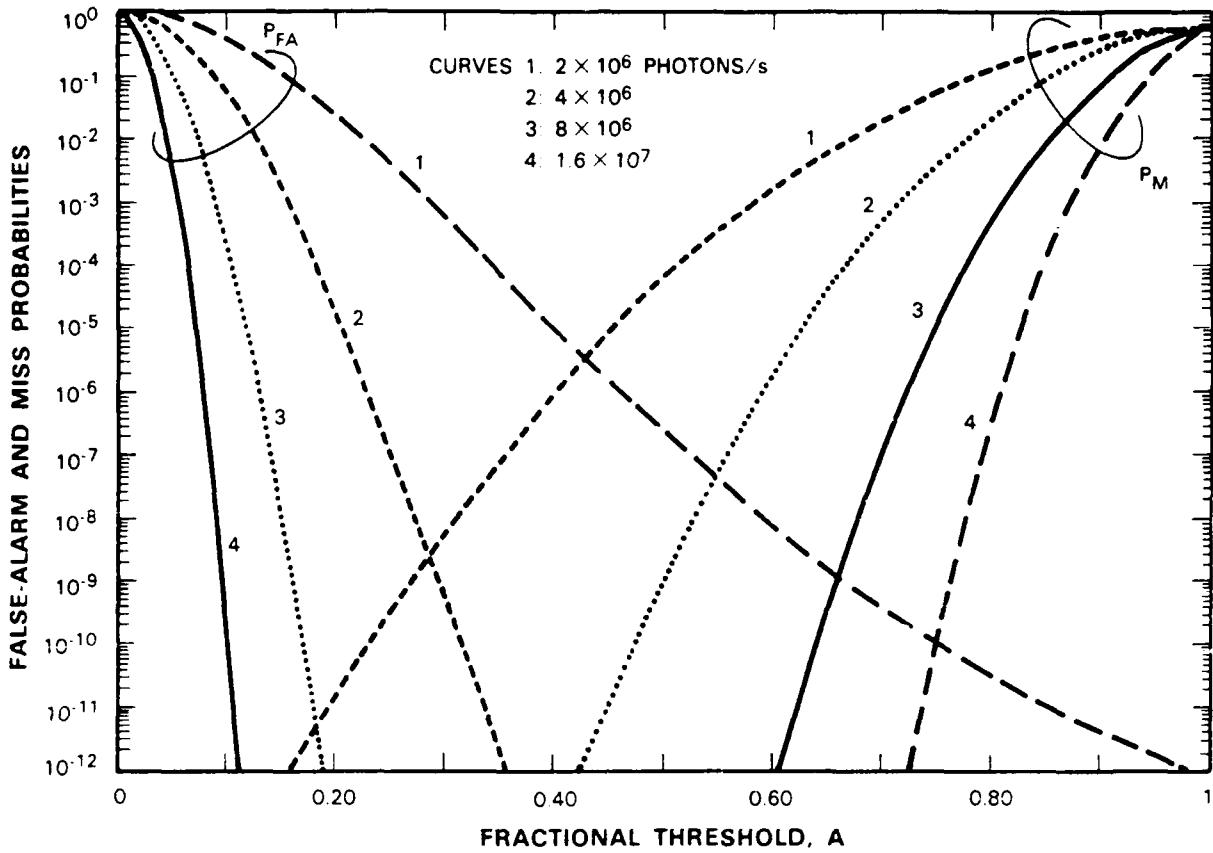
Figure A-1. Pick maximum dither scan performance (nighttime earth background).

A.2 SPIRAL SCANNING EQUATIONS

In this section we will briefly present the equations used in generating the spiral scan used during acquisition. Let

$$P(t) = R(t) e^{j\theta(t)} \quad (\text{A-7})$$

where $P(t)$ is the LOS position in polar coordinates with radius $R(t)$ and angle $\theta(t)$. The two differential



112043-6

Figure A2. Pick maximum dither scan performance (daytime earth background).

equations governing the radial growth and tangential velocity are given by

$$\left| \frac{dP(t)}{dt} \right| = V(t) \tag{A-8}$$

$$\frac{dR}{d\theta} = \frac{\Delta}{2\pi} \tag{A-9}$$

where $V(t)$ is the tangential velocity and Δ is the scan to scan separation. Therefore,

$$\left(\frac{dR(t)}{dt} \right)^2 + \left(R(t) \frac{d\theta(t)}{dt} \right)^2 = V(t)^2 \tag{A-10}$$

$$R(t) = \frac{\Delta}{2\pi} \theta(t) \quad (A-11)$$

The exact solution to these equations is difficult to solve and even more difficult to implement. However, ignoring the tangential velocity component due to the radial growth in $R(t)$ allows a simple solution that is easy to implement. That solution is given by

$$R(t) = \sqrt{\frac{\Delta}{\pi} \int_0^t V(\tau) d\tau} \quad (A-12)$$

$$\theta(t) = 2 \sqrt{\frac{\pi}{\Delta} \int_0^t V(\tau) d\tau} \quad (A-13)$$

The only approximation used in obtaining these solutions is the assumption that the radial growth did not contribute to the tangential velocity. For a constant velocity scan, it can be shown that after one spiral, the actual tangential velocity is within 1 percent of $V(t)$.

To limit the acceleration and frequency requirements of the HBO loop during the start of the scan, a ramp in tangential velocity is used ($V(t) = at$). Once the acceleration and frequency requirements are within the loop capability a constant tangential velocity is used ($V(t) = V_0$). The slower scans as well as the dither scan do not require any velocity ramp. For such scans it is easy to show that the time required to cover an uncertainty zone of Ω_u (full-width) is given by

$$T = \frac{\pi}{4} \frac{\Omega_u^2}{\Delta V_0} \quad (A-14)$$

REPORT DOCUMENTATION PAGE

1a. REPORT SECURITY CLASSIFICATION Unclassified		1b. RESTRICTIVE MARKINGS	
2a. SECURITY CLASSIFICATION AUTHORITY		3. DISTRIBUTION/AVAILABILITY OF REPORT Approved for public release; distribution is unlimited.	
2b. DECLASSIFICATION/DOWNGRADING SCHEDULE			
4. PERFORMING ORGANIZATION REPORT NUMBER(S) SC-80		5. MONITORING ORGANIZATION REPORT NUMBER(S) ESD-TR-89-158	
6a. NAME OF PERFORMING ORGANIZATION Lincoln Laboratory, MIT	6b. OFFICE SYMBOL (If applicable)	7a. NAME OF MONITORING ORGANIZATION Electronic Systems Division	
6c. ADDRESS (City, State, and Zip Code) P.O. Box 73 Lexington, MA 02173-9108		7b. ADDRESS (City, State, and Zip Code) Hanscom AFB, MA 01731	
8a. NAME OF FUNDING/SPONSORING ORGANIZATION HQ AF Systems Command	8b. OFFICE SYMBOL (If applicable) STC	9. PROCUREMENT INSTRUMENT IDENTIFICATION NUMBER F19628-85-C-0002	
8c. ADDRESS (City, State, and Zip Code) Andrews AFB Washington, DC 20334		10. SOURCE OF FUNDING NUMBERS	
		PROGRAM ELEMENT NO 63789F	PROJECT NO 270
		TASK NO	WORK UNIT ACCESSION NO
11. TITLE (Include Security Classification) Laser Intersatellite Transmission Experiment Spatial Acquisition, Tracking, and Pointing System			
12. PERSONAL AUTHOR(S) John E. Kaufmann and Eric A. Swanson			
13a. TYPE OF REPORT Project Report	13b. TIME COVERED FROM _____ TO _____	14. DATE OF REPORT (Year, Month, Day) 1989, September 12	15. PAGE COUNT 110
16. SUPPLEMENTARY NOTATION None			
17. COSATI CODES		18. SUBJECT TERMS (Continue on reverse if necessary and identify by block number)	
FIELD	GROUP	SUB-GROUP	
		optical acquisition, tracking, and pointing	
		optical intersatellite links	
		optical communication	
19. ABSTRACT (Continue on reverse if necessary and identify by block number)			
<p>This report describes the spatial acquisition, tracking, and pointing system of the MIT Lincoln Laboratory Laser Intersatellite Transmission Experiment (LITE) flight package which was to be integrated on the NASA Advanced Communication Technology Satellite (ACTS). The overall design approach and underlying rationale are also discussed. Considerable attention is given to the characterization of the spacecraft's dynamic environment and its impact on acquisition and tracking subsystem design and performance.</p>			
20. DISTRIBUTION/AVAILABILITY OF ABSTRACT <input type="checkbox"/> UNCLASSIFIED/UNLIMITED <input checked="" type="checkbox"/> SAME AS RPT. <input type="checkbox"/> DTIC USERS		21. ABSTRACT SECURITY CLASSIFICATION Unclassified	
22a. NAME OF RESPONSIBLE INDIVIDUAL Lt. Col. Hugh L. Southall, USAF		22b. TELEPHONE (Include Area Code) (617) 981-2330	22c. OFFICE SYMBOL ESD/TML